VARIATIONS IN CLIMATIC REGIMES OF TEXAS: AN ASSESSMENT OF WET SEASONS, CLIMATIC CYCLES, AND EXTREME PRECIPITATION EVENTS

A Thesis

by

NIKHIL BHATIA

Submitted to the Office of Graduate and Professional Studies of
Texas A&M University
in partial fulfillment of the requirements for the degree of

MASTER OF SCIENCE

Chair of Committee,	Vijay P. Singh
Co–Chair of Committee,	Clyde L. Munster
Committee Member,	Inci Güneralp
Head of Department,	Ronald A. Kaiser

August 2017

Major Subject: Water Management and Hydrological Science

ABSTRACT

Quantification of changing climatic regimes is essential for managing regional water resources systems. Climatic variations have resulted in intensified wet periods and frequent extreme precipitation events in the state of Texas. Our first research objective is to evaluate the total number of different degrees of wet periods and extreme precipitation events during four seasons in the last four decades: (i) *Winter Season*: December to February, (ii) *Spring Season*: March to May, (iii) *Summer Season*: June to August, and (iv) *Autumn Season*: September to November. A 3–month time–scale Standardized Precipitation Index (SPI) is employed to obtain the hydrometeorological trends for regional wet periods. One–day extreme precipitation events of the order of respective SPI threshold recurrence intervals are extracted using an appropriately fitted probability distribution. Further, much of the literature evaluates the impact of the varying state of global–scale climatic cycles on the intensified regional hydrometeorologic cycle of Texas. Therefore, in our second research objective we aim to quantify the impact of five major Atlantic and Pacific Ocean based Climatic Cycles: (i) Atlantic Multidecadal Oscillation (AMO), (ii) North Atlantic Oscillation (NAO), (iii) Pacific Decadal Oscillation (PDO), (iv) Pacific North American Pattern (PNA), and (v) Southern Oscillation Index (SOI), on annual precipitation extremes in Texas, using a unique weighted correlation approach incorporating Leave–One–Out–Test (LOOT). The Cold and Warm Desert/Semi–Arid climate regions are found to be influenced by the NAO, whereas extreme precipitation regimes in the Humid Sub–Tropical climate region are affected by the variations in the

AMO. Our third research objective is to determine the sensitivity of annual precipitation extremes with changing states of both warm and cold phases of the most correlated climatic cycles. Sensitivity analyses showcase that extreme precipitation events in both Cold and Warm Desert/Semi–Arid climate regions are not sensitive to the NAO, however, in the case of Humid Sub–Tropical climate region, the AMO drives the temporal variability of annual precipitation extremes. Results of this study coupled with reliable long–term forecasts of climatic cycles will help prepare regional water boards for scenarios of excess precipitation and extreme hydrometeorologic events in a changing climate.

DEDICATION

This thesis is dedicated to my family and friends whose constant support and words of encouragement guided me throughout the process. I would like to share a special feeling of gratitude for my loving parents, Mr. Pradeep Bhatia and Mrs. Suman Bhatia, who taught me the essence of hard work and the art of setting challenging yet achievable goals. Their unconditional love, care, and innumerous sacrifices gave me the strength to dream and aspire to pursue the higher level of study in the field of hydrometeorology.

ACKNOWLEDGEMENTS

Foremost, I would like to express genuine gratitude and thank my research advisor: Dr. Vijay P. Singh (Distinguished Professor, Regents Professor and Caroline & William N. Lehrer Distinguished Chair in Water Engineering, Department of Biological and Agricultural Engineering, Texas A&M University, College Station, Texas), for providing me with an opportunity to conduct this research under his guidance. All his needful comments significantly helped throughout the development of our work. His vision and foresight inspired me to elevate this research to its full extent.

I would like to express my sincere appreciation and thank my committee co–chair Dr. Clyde L. Munster (Professor, Department of Biological and Agricultural Engineering, Texas A&M University, College Station, Texas), and committee member Dr. Inci Güneralp (Assistant Professor, Department of Geography, Texas A&M University, College Station, Texas), for their genuine support and guidance throughout the completion of my research and courses at the Texas A&M University.

I owe a debt of gratitude to Dr. Roshan K. Srivastav (Associate Professor, Centre for Disaster Mitigation and Management, VIT University, Vellore, India) for his unconditional support throughout the completion of the work. His comments helped me to significantly refine the ideas of various aspects of this research.

I extend my deepest appreciations to Dr. Ronald A. Kaiser (Chair, Water Management and Hydrological Science, Texas A&M University, College Station, Texas), and Dr. Rosario Sanchez Flores (Research Scientist, Texas Water Resources Institute, College Station, Texas), and Dr. C. Prakash Khedun (Program Coordinator, Water Management and Hydrological Science, Texas A&M University, College Station, Texas) for their constant support and inspiration.

I would like to thank Texas A&M University, College Station, Texas, for providing me with all the necessary facilities to carry out this research. Last but not the least, I would like to express my deepest thanks to my parents, all teachers, many friends, and great people of Bryan/College Station for all their selfless efforts to help, support, and guide me at innumerable steps during my stay at prestigious Texas A&M University.

CONTRIBUTORS AND FUNDING SOURCES

This work was supervised by a thesis committee consisting of Dr. Vijay P. Singh of the Department of Biological and Agricultural Engineering (Advisor and Committee Chair), Dr. Clyde L. Munster of the Department of Biological and Agricultural Engineering (Committee Co–Chair), and Dr. Inci Güneralp of the Department of Geography (Committee Member).

The work for all the research objectives was completed independently under the guidance of Dr. Vijay P. Singh.

Major academic expenses for my graduate study at the Texas A&M University was supported by the awarded Lechner Fellowship (Academic Year 2015–16) and WMHS Scholarship (Academic Year 2016–17) from Department of Water Management and Hydrological Science, and Texas Public Education Grant (International) (Academic Year 2016–17) from Texas A&M University.

This work was further made possible in part by U.S. Army Engineer Development Research Center, U.S. Army Corps of Engineers, Vicksburg, Mississippi, under Grant Number W912HZ–16–C–0027. The contents of this research are solely the responsibility of the author and do not necessarily represent the official views of the federal agency: U.S. Army Corps of Engineers (USACE).

NOMENCLATURE

AMO	Atlantic Multidecadal Oscillation
CDF	Cumulative Distribution Function
CDO	Climate Data Online
DJF	December to February
DX90	Total number of days with projected maximum temperature exceeding 90ºF in a month
DX90–S	Total number of days with projected maximum temperature exceeding 90ºF in the season
EMXP	Extreme daily precipitation in a month
EMXT	Extreme maximum temperature for a month
EMXT–S	Mean of maximum daily temperature in the season
ENSO	El Niño–Southern Oscillation
IDW	Inverse Distance Weighted (Interpolation method)
JJA	June to August
LOOT	Leave–One–Out–Test
MAM	March to May
MOC	Atlantic Meridional Overturning Circulation
NAO	North Atlantic Oscillation
NASH	North Atlantic subtropical high pressure system
NCDC	National Climatic Data Centre

NOAA	National Oceanic and Atmospheric Administration
NSDI	National Spatial Data Infrastructure
PDF	Probability Density Function
PDO	Pacific Decadal Oscillation
$P_{extreme}$	Maximum daily precipitation event within a year
PNA	Pacific North American Pattern
PRCP	Monthly total precipitation
SOI	Southern Oscillation Index
SON	September to November
SPI	Standardized Precipitation Index
SST	Sea–surface temperature
T_{avg}	Average monthly temperature
T_{avg}–S	Average seasonal temperature
USGS	United States Geological Survey

TABLE OF CONTENTS

LIST OF FIGURES

LIST OF TABLES

CHAPTER I

INTRODUCTION

The changing climatic patterns have intensified the global, regional, and local meteorological regimes across the globe. The intensity and frequency of precipitation events in the mid–latitude land areas of the Northern Hemisphere have increased moderately after 1901 but steadily after 1951 (Stocker et al. 2013, WGII 2014). Since 1901, an increment of 0.17 in./decade has been observed in the total annual precipitation for the contiguous United States in comparison to the worldwide increment rate of 0.08 in./decade (Blunden and Arndt 2016). In recent years, a large percentage of these downpours occurred in the form of extreme one–day precipitation events. The periodicity of such heavy precipitation events remained fairly constant from 1910 to 1980, but have since risen rapidly (Bell et al. 2016). Due to this climate change, Texas observed an increment in the overall surface temperature by 0.5ºC–1ºC, a rising trend in precipitation in two thirds of the state with a 10% overall increase in annual averages, and a 16% hike in extreme precipitation events in the last century (Karl 2009, Anderson et al. 2016). The hydrometeorological literature almost unanimously predicts higher magnitudes of downpours, wetter summer and winter seasons, and frequent extreme precipitation events for the state of Texas in the coming decades (Melillo et al. 2014, Pryor et al. 2014).

The vast areal extent of the state encompasses a wide–range of geography, resulting in considerable spatial climatic differences across the state. However, previous studies did not incorporate these differences while addressing the variability of wet climatic regimes for the state of Texas. Therefore, an assessment of the long–term variations in the occurrences of wet seasons and extreme precipitation events in different climate regions of Texas is certainly of prime importance. As part of our first research objective, we aim to assess the decadal variation of wet seasons/periods and extreme precipitation events at the conventional seasonal scale (*Winter Season*: December to February; *Spring Season*: March to May; *Summer Season*: June to August; *Autumn Season*: September to November) for different climate regions of Texas during the period 1971–2010.

Extreme precipitation events lead to devastating floods which cause immense amount of losses in infrastructural, communication, livestock and agricultural systems, and eventually disrupt the society (Mishra and Singh 2010). Climatic cycles define major atmospheric/oceanic anomalies on the monthly, seasonal, annual, decadal, and multi–decadal time–scales which affect the regional climate of widely separated areas over the globe (Quadrelli and Wallace 2004, Trenberth et al. 2006, Hurrell et al. 2003a). As a measure of climate variability, these cycles are regarded as the major driver of precipitation extremes and their space–time variability that exercise a considerable influence on people's lives and regional economies (Kripalani and Kulkarni 2001). The integral property of long–term predictability of climatic cycles (Mantua and Hare 2002, Wang et al. 2002, Johansson 2007) can certianly be used for analyzing precipitation extremes, either as indicators or as potential inputs for mathematical modeling. In recent years, several studies have investigated the relationship between climatic cycles and precipitation (Cai et al. 2001, Chan and Zhou 2005, Goodess and Jones 2002) which helps understand the changing regional hydroclimatic regimes (Renard and Lall 2014). However, none of these aforementioned research studies examined the difference in the respective relationship with changing range of precipitation extremes. Therefore, as part of second research objective, we aim to quantify the potential links between Atlantic and Pacific Ocean based climatic cycles and different ranges of annual precipitation extremes (recurrence interval exceeding 2, 5, and 10 years) for different climate regions of Texas.

A comprehensive investigation of the variations in climatic cycles and the related impacts on the meteorological cycle is considered to be quite important. In addition to the examination of potential links between Atlantic and Pacific Ocean based climatic cycles and annual precipitation extremes, an evaluation of the degree of impact of the most correlated climatic cycles on regional precipitation extremes of Texas will be essential in applying the key findings of the research in real–time. Further, the different phases of climatic cycles are known to have a considerably variable effect on the regional hydrologic cycle (Knight et al. 2006, López-Moreno et al. 2011, Mo 2010, Kurtzman and Scanlon 2007). However, the effect of fluctuations in different phases of climatic cycles on hydrometeorologic regimes does not seem to have been evaluated. Therefore, as part of our third research objective we aim to quantify the sensitivity of annual precipitation extremes in both warm and cold phases of most correlated climatic cycles for different climate regions of Texas.

CHAPTER II

CLIMATIC CYCLES

In the second research objective, climatic variability is defined using five climatic cycles related to Atlantic and Pacific Oceans: (i) Atlantic Multidecadal Oscillation (AMO), (ii) North Atlantic Oscillation (NAO), (iii) Pacific Decadal Oscillation (PDO), (iv) Pacific North American Pattern (PNA), and (v) Southern Oscillation Index (SOI). Monthly data of Atlantic Multidecadal Oscillation (AMO), North Atlantic Oscillation (NAO), Pacific Decadal Oscillation (PDO), and Pacific North American Pattern (PNA) were obtained from the Earth System Research Laboratory database, and the monthly data of Southern Oscillation Index (SOI) was downloaded from Australian Government's Bureau of Meteorology database.

II.1 Atlantic Multidecadal Oscillation (AMO)

AMO is the globally–scoped multi–decadal scale oceanic temperature phenomenon (Kerr 2000), which has a significant impact on regional to hemispheric climate regimes (Wanner et al. 2008). Over the last 150 years, AMO has been identified as a coherent cycle of North Atlantic sea–surface temperatures (SSTs) with a period of about 60–90 years (Schlesinger and Ramankutty 1994, Knudsen et al. 2011). For the state of Texas, tropical cyclone precipitation is the major contributor of extreme precipitation (Zhu et al. 2013) and is found to be significantly connected with AMO (Nogueira and Keim 2010). In the hurricane season (August–October), a decreasing trend of mean precipitation is observed for an increasing trend of AMO; however, extreme precipitation shows a positive relationship with the warm phase of AMO (Curtis 2008). Further, for summertime, precipitation regimes in Texas are found to be influenced by the warm phase of AMO (Hu and Feng 2012).

II.2 North Atlantic Oscillation (NAO)

NAO is based on the north–south pressure gradients over the northern hemisphere of the Earth, the dynamics of which are still not well understood as compared to its counterparts (Hurrell et al. 2003b). It measures the anomalies in sea level pressure between the Icelandic low–pressure zone and the subtropic atmospheric high–pressure system centered over the Azores (Ottersen et al. 2001). For the western Atlantic area and across eastern and southern North America, NAO is characterized by the below normal geopotential heights (Hurrell and Deser 2010). This climatic phenomenon reduces the westerlies and causes high–latitude blocking of storm tracks, driving the advection of cold and dry air from Alaska and Canada into the United States, and eventually affecting the precipitation regimes in the case of Texas (Parazoo et al. 2015).

II.3 Pacific Decadal Oscillation (PDO)

PDO characterizes the pacific decadal variability in Northern Hemisphere climate, with temperature anomalies in the central North Pacific zone surrounded by anomalies of opposite sign in the Alaska gyre, off California, and toward the Tropics (Schneider and Cornuelle 2005). It is a robust multi–decadal climatic variability in SSTs centered over the extra–tropical North Pacific basin (MacDonald and Case 2005, Minobe 2000). The wet summertime conditions, extending from the southwest to the central United States, along with strong negative values in the northern part of the central and western United States, are found to be well–related with PDO (Barlow et al. 2001). The winter precipitation phase in Texas is observed to be drier for the cold PDO and wetter for the warm PDO (Goodrich and Walker 2011). PDO is the north Pacific component of the inter–decadal pacific oscillation, the cold phase of which results in increased autumn precipitation for Texas (Dai 2013).

II.4 Pacific North American Pattern (PNA)

PNA defines the anomalies in the mid– to upper–tropospheric geopotential height fields over the North Pacific Ocean (Wallace and Gutzler 1981). PNA pattern is a prominent feature of atmospheric low–frequency variability in the Northern Hemisphere extratropical region (between intermountain and southeastern United States) due to the thermal forcing from the equatorial Pacific (Kawamura et al. 1995, Shukla and Wallace 1983). A dipole pattern of precipitation anomalies extending from California to the southeastern United States is observed as a result of storm track changes in association with PNA (Trenberth and Hurrell 1994). This mechanism results in enhanced precipitation in the southern U.S. and diminished precipitation in the northern U.S. (Trenberth et al. 2003). Leathers et al. (1991) found wetter southeastern United States in the case of warm phase of PNA in winters, and Henderson and Robinson (1994) found more summertime precipitation than wintertime in the case of cold phase of PNA.

II.5 Southern Oscillation Index (SOI)

Southern Oscillation is the atmospheric mass cycle, based on coherent air exchanges between the eastern Pacific (Tahiti) and the western Pacific (Darwin)

(Trenberth and Caron 2000). SOI is measured as the normalized difference of the standardized sea–level pressures between these two Pacific ends (Yan et al. 2011). It is estimated as ten times the difference of sea level pressure of Tahiti and Darwin (Troup 1965), and is considered as the major indicator of El Niño–Southern Oscillation (ENSO) (Chiew and McMahon 2002). The increased moisture in the southwestern United States during Central Pacific (Eastern Pacific) El Niño events is owing to the south–westerly low level flow from the western (eastern) tropical Pacific Ocean (Weng et al. 2009).

CHAPTER III

CLIMATE REGIONS OF TEXAS

The state of Texas, with an approximate area of 173 million acres (ac), covers a broad range of ecosystems in its expanse. Mesquite and hardwood forests are dominant in the eastern end of Texas, with an accumulative acreage of 60 million ac. The prairies and temperate grasslands are mainly found in the northern and east–central regions, along with coastal prairies ecosystem in the vicinity of the Gulf Coast. The western part of Texas is predominantly covered by desert and arid regions, whereas the northeastern parts showcase wetlands and swamps (Griffith et al. 2004, Smith and Campbell 1996). The state also encompasses a wide–range of geography: extending from the Guadalupe peaks in the far west to the Gulf coast in the distant east, and from the sharp escarpments adjacent to the northwest Panhandle lowlands to the karst topography of the hill country in the central region and semi–tropical Lower Rio Grande Valley in the southern end (The Handbook of Texas Online, 2012). The presence of such dense geographical, topographical, and ecological units results in a highly diverse range of climate, incoherent regional weather patterns, and vast spatial variations in local/regional meteorology across the state (Nielsen-Gammon 2011). Therefore, adoption of a well–classified research approach is vital for understanding the variations in precipitation regimes of Texas. The state has been divided into various climate regions by the National Climatic Data Centre (NCDC) and the Köppen–Geiger Climate Classification system.

III.1 NCDC Climate Divisions of Texas

NCDC Climate Divisions for the United States have been widely used in analyzing climate change (Booth et al. 2012), hydrometeorological attributes (Vose et al. 2014), meteorological extremes (Houston and Changnon 2007, Tippett et al. 2014), and climatic indices (Gleason et al. 2008, Squires et al. 2014). NCDC delineated 344 climate divisions for the contiguous United States on the basis of similar attributes of vegetation, annual and monthly averages of temperature, and water–equivalent precipitation during the period of 1895–2013 (Karl and Koss 1984, Guttman and Quayle 1996). The shapefile of these climate divisions for the United States can be obtained from USGS Water Resources NSDI Node. Figure 1 illustrates 10 such climate divisions lying in the state of Texas: (i) High Plains, (ii) Low Rolling Plains, (iii) North Central, (iv) East Texas, (v) Trans Pecos, (vi) Edwards Plateau, (vii) South Central, (viii) Upper Coast, (ix) Southern, and (x) Lower Valley. The monthly average precipitation and temperature for these climate divisions are shown in Figure 2 and Figure 3, respectively. None of the weather stations later mentioned (Chapter V) lie in the Southern and Lower Valley, and hence the respective climate divisions' attributes are not analyzed. More details regarding the land cover and variations in weather characteristics of these climate divisions are provided in the 2012 State Water Plan Report of Texas Water Development Board.

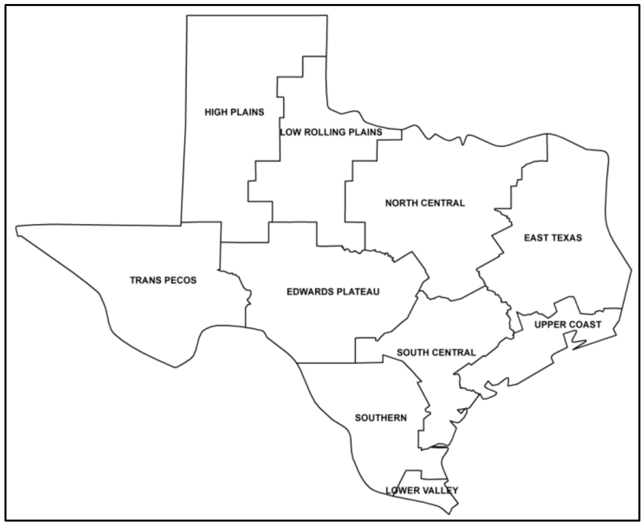

Figure 1: NCDC climate divisions of Texas

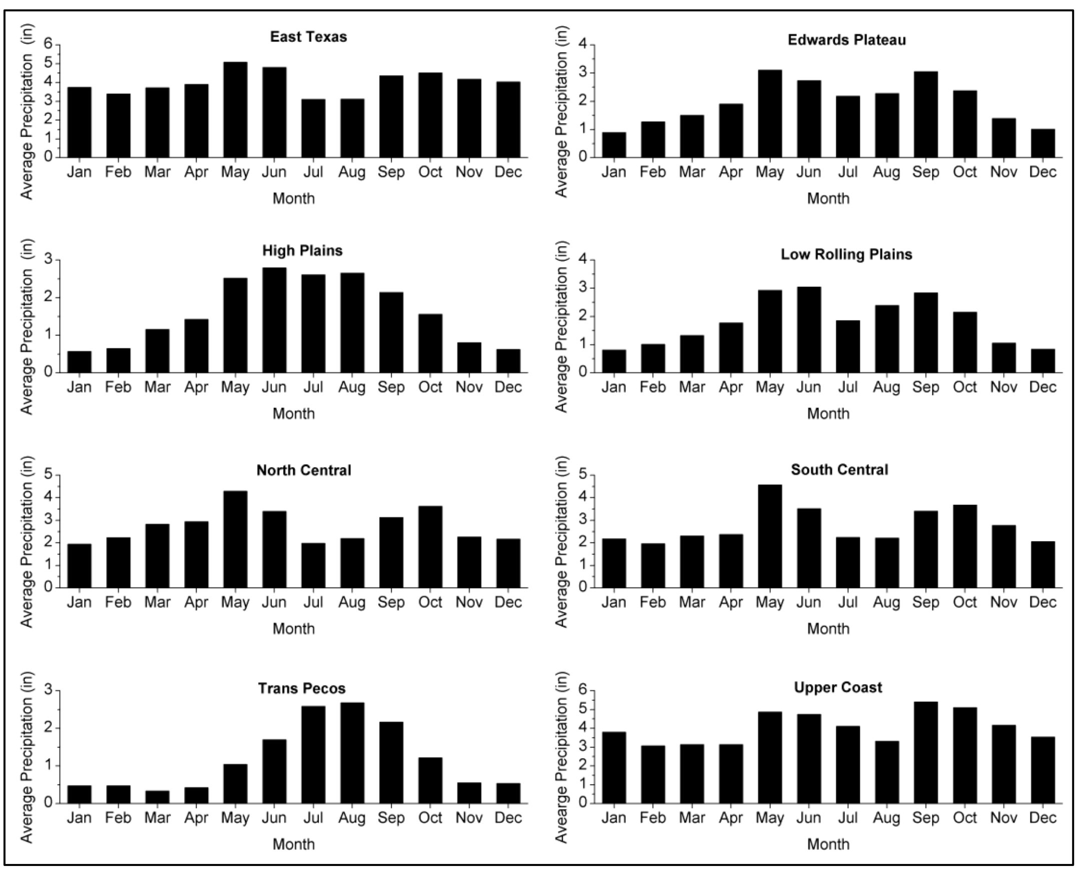

Figure 2: Monthly average precipitation for NCDC climate divisions of Texas

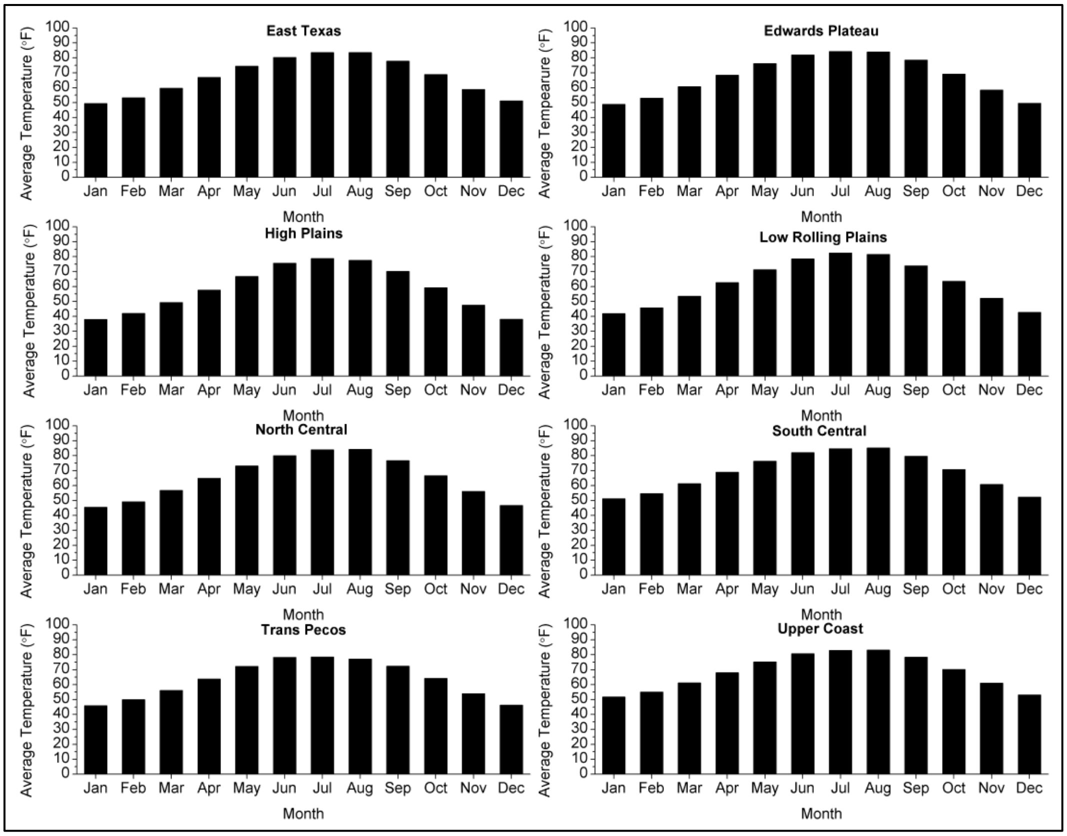

Figure 3: Monthly average temperature for NCDC climate divisions of Texas

III.2 Köppen–Geiger Climate Regions of Texas

Köppen–Geiger Climate Classification System is considered to be one of the most comprehensive climate classification systems for the entire world (Essenwanger 2001). The system is widely used in the fields of meteorology (Gnanadesikan and Stouffer 2006), hydrology (McMahon et al. 2007), and climate analysis (Diaz and Eischeid 2007, Rubel and Kottek 2010). The system delineates climate regions broadly on the basis of annual, seasonal, and monthly averages of weather variables and defines three characteristics for a region: (i) annual and monthly averages of temperature and rainfall, (ii) rainfall distribution, and (iii) temperature variation (Alvares et al. 2013, Kottek et al. 2006). Originally presented by Wladimir Köppen (Köppen 1900), the updated system developed by Rudolf Geiger (Geiger 1954) incorporates the regional climatology of 4279 weather stations world–wide for their entire period of record, and the observed data was interpolated using the 2–D thin–plate spline with the tension approach (Peel et al. 2007). The shapefile of climate regions for the entire world can be downloaded from the website of World Maps of Köppen–Geiger Climate Classification. The state of Texas is mainly divided into three regions: (i) Cold Desert/Semi–Arid Climate, (ii) Humid Subtropical Climate, and (iii) Warm Desert/Semi–Arid Climate, as shown in Figure 4.

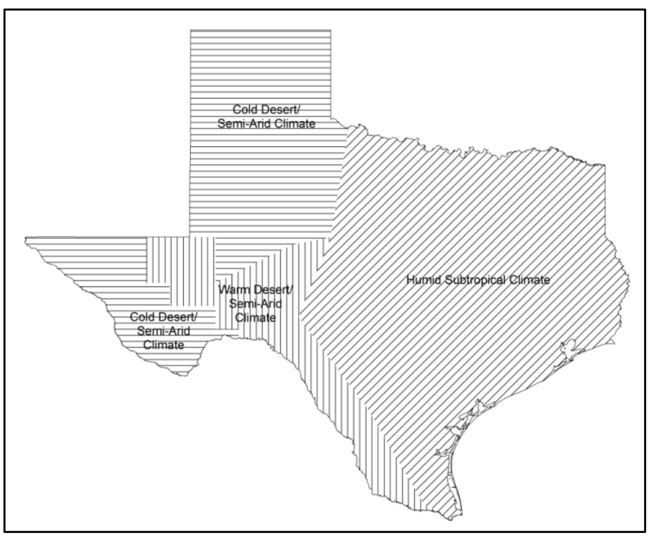

Figure 4: Köppen–Geiger climate regions of Texas

In this study the aforementioned NCDC climate divisions and Köppen–Geiger climate regions are merged in the following way. Here, the classification repeats a few of the NCDC climate divisions because of the aforementioned poor data coverage for the Southern and Lower Valley, and also because of the dual climate regimes in the Low Rolling Plains and Trans Pecos climate divisions.

(i) *Cold Desert/Semi–Arid climate region*: High Plains, Low Rolling Plains, and Trans Pecos.

(ii) *Humid Sub–Tropical climate region*: East Texas, Edwards Plateau, Low Rolling Plains, North Central, South Central, and Upper Coast.

(iii) *Warm Desert/Semi–Arid climate region*: Edwards Plateau and Trans Pecos.

CHAPTER IV

LITERATURE REVIEW

IV.1 Research Objective I

For this research objective, we aim to assess the decadal variability of wet seasons and extreme precipitation events for each climate region of Texas delineated by well–classified Köppen–Geiger Climate System. The assessment is based on the 3–month Standardized Precipitation Index (SPI) values for different climate regions that illustrate the wet periods' trends in seasons: (i) *Winter Season*: December to February, (ii) *Spring Season*: March to May, (iii) *Summer Season*: June to August, and (iv) *Autumn Season*: September to November.

McKee et al. (1993) developed SPI as an alternative to the Palmer Index for the purpose of drought monitoring and analysis in the state of Colorado. Primarily built for defining droughts, the index is now commonly used to determine the cumulative probability of precipitation events occurring at a weather station. The appropriately fitted inverse normal (Gaussian) function to the cumulative probability yields the SPI values at a desired time–scale (Guttman 1998), which further describes the number of standard deviations above and below the average precipitation at the weather station. In comparison to other physically–based precipitation indicators, the SPI is commonly used as an indicator of dry and wet seasons because of the ease in calculation with mere precipitation inputs and no prior parametric calibration, convenience in spatial invariant application, and robust illustration of trends in precipitation at differing time–scales for a given region (Zhang et al. 2009, Du et al. 2013, Li et al. 2008, Wu et al. 2007).

In the past, the SPI values were scrutinized for analyzing meteorological droughts and dry seasons for the state of Texas. For the detection of drought onset, Hayes et al. (1999) determined the SPI values at the scales of 1–, 5–, 6–, 9–, 10–, 11–, and 12–months for the 1996 drought. McRoberts and Nielsen-Gammon (2012) determined the SPI values for meteorological droughts in arid regions and reported the intensity and spatial extent of the 2008–09 drought in Texas. Recently, the SPI has also been used to analyze wet seasons/periods for the state of Texas. For the 2009 drought areas in southern Texas, NOAA National Centers for Environmental Information reported wetter conditions for December 2009 with 1– to 3–months SPI indices, and they also addressed long–term precipitation deficits with the SPI values computed at the time–scales of 9– to 24–months.

Table 1 lists the categories of wet seasons, defined on the basis of SPI thresholds given by McKee et al. (1993) and Du et al. (2013). Further, one–day downpours of the order of respective SPI threshold recurrence intervals listed in Table 2 were considered as extreme precipitation events. The respective thresholds of these extreme precipitation events are obtained by an appropriately fitted probability distribution (Hanson and Vogel 2008). Appendix A lists 47 probability distributions that were fitted for each weather station and ranked using the Kolmogorov–Smirnov (Chakravarti and Laha 1967), Anderson–Darling (Stephens 1974), and Chi–Squared (Greenwood and Nikulin 1996) tests.

Table 1: Wet season categories for Texas

S. No.	SPI range	Category of Season
1	0.00 to 0.99	Moderately Wet
2	1.00 to 1.99	Considerably Wet
3	≥ 2.00	Extremely Wet

Table 2: Recurrence interval of SPI values

S. No.	SPI	Probability of Occurrence	Recurrence Interval
1	0	0.500	2
2	1	0.159	6
3	2	0.023	44

The changing trends in precipitation regimes of different climate regions must be validated against the observed respective historical climatic variations. Most of the ecohydrological processes in Texas are significantly influenced by the regional surface temperatures (Lyons 1990, Schmandt et al. 2011). Climate regions with significant increments in these variables are highly likely to observe intensified wet climatic regimes because of the enhanced capability of atmosphere to hold moisture, and vice versa (Berg et al. 2013). Therefore, we also study the variation in three temperature–related variables: (i) average seasonal temperature (T_{avg}–S), (ii) mean of maximum daily temperature in the season (EMXT–S), and (iii) total number of days with projected maximum temperature exceeding 90ºF in the season (DX90–S), and examine its respective resonance with the determined decadal trends of wet seasons and extreme precipitation events for each climate region of Texas.

IV.2 Research Objective II

In order to attain an all–inclusive knowledge of regional precipitation regimes, we aim to evaluate their statistical links with variations in global–scaled climatic cycles. Power et al. (2006) showed a link between El Niño–Southern Oscillation (ENSO) and observed and simulated mean rainfall for Australia. Hill et al. (2011) examined the atmospheric circulation response triggered by tropical Pacific Ocean sea–surface temperature (SST) anomalies, which resulted in austral summer rainfall variability in South America. Folland et al. (2001) investigated the decadal changes in Northeast Brazil wet season precipitation with changing SST gradients between the north and south tropical Atlantic. Silva and Ambrizzi (2006) and Grimm (2003) assessed the impact of El Niño events and inter–El Niño variation on moisture transport and precipitation anomaly in subtropical South America. Enfield et al. (2001) analyzed multi–decadal and inter–annual precipitation patterns over the continental U.S. and linked them with varying phases of Atlantic Multidecadal Oscillation (AMO). Hu and Feng (2012) evaluated the joint impacts of AMO and ENSO on precipitation circulation in North America.

For this research objective we aim to quantify the impact of Atlantic and Pacific Ocean based climatic cycles (Chapter II) on the maximum daily precipitation events within a year ($P_{extreme}$) in the Köppen–Geiger climate regions of Texas. These $P_{extreme}$ data for a weather station can be classified using probability distributions (Section IV.1). The strength of the relationship between climatic cycles and extreme precipitation was tested using the Pearson Correlation Coefficient (Pearson 1920). Since the traditional Pearson method is affected by data outliers (Kim and Fessler 2004), we used the weighted average correlation coefficients for each weather station using the method described in Niven and Deutsch (2012). The effect of each outlier data point is diminished by incorporating the method of Leave–One–Out–Test (LOOT). The weighted correlation coefficient results in a more comprehensive reflection of the hydrometeorologic process (Krause et al. 2005).

In the field of hydrometeorology, the significance of research can only be defined with the respective clause of uncertainty (Montanari 2007, Ramos et al. 2010). Such analysis further helps perform sensitivity studies for the region. Therefore, we incorporated the factor of uncertainty by estimating the correlation coefficient at a high confidence interval. For the majority of hydrometeorological analysis, 95% confidence interval is considered appropriate by the state water boards for risk evaluation and management strategies (Francisco-Fernández and Quintela-del-Río 2016). The calculated correlation coefficients were further spatially interpolated using the Inverse Distance Weighted (IDW) interpolation method (Bartier and Keller 1996), which is an efficient and a considerably simpler method to interpolate precipitation characteristics for the spatially dense weather station networks (Chen and Liu 2012).

IV.3 Research Objective III

Evaluation of the intensified hydrologic cycle and the development of long–term water resources strategies require a comprehensive assessment of the impact of changing global climate and variability in climatic cycles at a smaller regional scale (Sorooshian et al. 2003). Sensitivity analysis with global–scale climatic cycles reveals the controlling mechanisms of precipitation regimes for a region (Gerlitz et al. 2016). Jones and Carvalho (2014) found the intensity of precipitation in the U.S. to be significantly sensitive to the Maddden–Julian Oscillation. Marani and Zanetti (2015) found the daily extreme rainfall events in Padova, Italy, to be mainly influenced by the variation in the North Atlantic Oscillation. Dore (2005) found increasing frequency and variance of tropical extreme precipitation events and quantified the respective potential links with major ocean currents and climatic cycles. But none of these studies attempted to examine the influence of different phases on regional precipitation extremes separately.

For this research objective, we aim to evaluate the sensitivity of annual precipitation extremes in both the warm and cold phases of most correlated climatic cycles (derived from second research objective) to annual precipitation extremes in different climate regions of Texas, using a linear least squares regression function devised by Bouwer et al. (2008). This statistical method has been widely used in the area of environmental decision making (Pianosi et al. 2016). Ward et al. (2010) used this regression function to assess the impact of El Niño–Southern Oscillation (ENSO) on mean annual, 1–day and 7–day maximum streamflow discharge for 609 stations across the world. Discussing the method as differentiated sensitivity analysis, we also analyzed the variation in the calculated sensitivity indices (with 95% confidence bounds) as compared to the integrated sensitivity analysis (with no distinct assessment for the warm and cold phases). The study concludes with an investigation of the spatial variation of sensitivity indices with varying hydrometeorological attributes, such as elevation, average precipitation, and average temperature, and the projected increments in the degree of annual precipitation extremes.

CHAPTER V

HYDROMETEOROLOGICAL DATA

Hydrometeorological data were obtained for numerous weather stations in different NCDC Climate Divisions from the National Climatic Data Center–Climate Data Online database, and then categorized amongst Köppen–Geiger Climate Regions, as per the classification explained in Chapter III. Only the weather stations with cent–percent data coverage were selected, which help minimize the overall uncertainty in research results.

V.1 Research Objective I

Data of monthly total precipitation (PRCP), extreme daily precipitation in a month (EMXP), average monthly temperature (T_{avg}), extreme maximum temperature for a month (EMXT), and total number of days with projected maximum temperature exceeding 90ºF in a month (DX90) for 21 weather stations, as shown in Figure 5, were obtained for a period of 40 years (1971–2010).

V.2 Research Objective II and III

Data of extreme daily precipitation in a month (EMXP), total precipitation in a month (PRCP), and average monthly temperature (T_{avg}) for 26 weather stations, as shown in Figure 6, were downloaded for a period of 49 years (1966–2014). The annual averages and the anomalies for precipitation and temperature required for the analyses were obtained using the aforementioned meteorological variables.

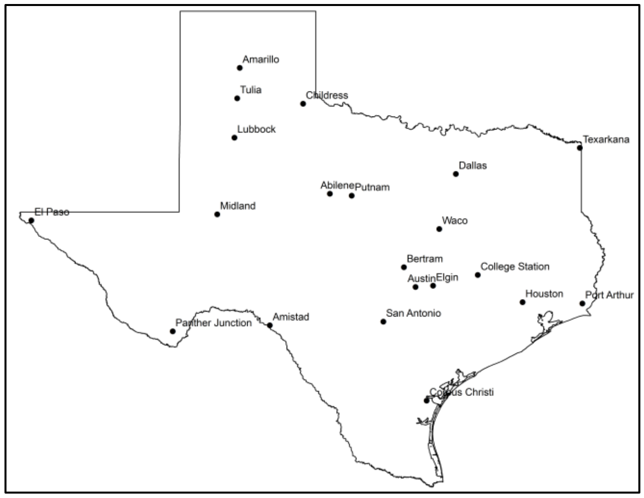

Figure 5: Weather stations with cent percent data coverage for monthly weather attributes for a period of 40 years (1971–2010) for Research Objective I

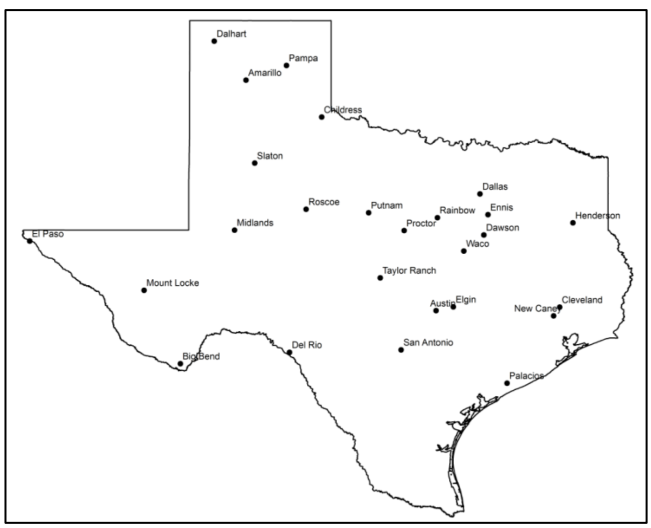

Figure 6: Weather stations with cent percent data coverage for monthly weather attributes for a period of 49 years (1966–2014) for Research Objective II and III

CHAPTER VI

STUDY METHODOLOGY

VI.1 Research Objective I

VI.1.1 Estimation of Standardized Precipitation Index

The Standardized Precipitation Index (SPI) was developed by McKee et al. (1993) to determine the anomalies in precipitation events or wet/dry seasons with respect to long–term normal conditions of the region at various time scales (Du et al. 2013). For this research objective, 3–month SPI values were determined, using monthly total precipitation estimates, to illustrate the seasonal trends of wet seasons in the different climate regions of Texas. Kumar et al. (2009) explained the complete procedure to calculate the SPI values for a weather station at a given timescale. In the past, SPI was quantified using various probability distributions, such as Pearson Type III, Lognormal, Exponential, and Extreme Value Distribution (Lloyd-Hughes and Saunders 2002, Thom 1966, Guttman 1999). However, the two–parameter gamma probability density function was widely accepted as the appropriate distribution to evaluate the SPI values (Wu et al. 2007, Kumar et al. 2013). For our case, the same gamma distribution (Equation 1) with the shape and scale parameters was incorporated to evaluate the SPI values, using SPI_SL_6 executable file developed by University of Nebraska, Nebraska (Svoboda et al. 2012).

$$f(x) = \frac{1}{\beta^{\alpha}\Gamma(\alpha)} x^{\alpha-1} e^{-x/\beta} \;\forall\, x > 0 \tag{1}$$

where α is the shape parameter, β is the scale parameter, and $\Gamma(\alpha)$ is the gamma function. Since the distribution is undefined at zero precipitation, the cumulative probability distribution was therefore derived using equation 2:

$$g(x) = p + (1 - p)\, f(x) \tag{2}$$

where p is the probability of zero precipitation.

VI.1.2 Extraction of Extreme Precipitation Events

Nielsen-Gammon et al. (2005) predicted a long–term upward trend in extreme precipitation events in Texas. The 47 probability distributions listed in Appendix A were fitted to annual precipitation extremes obtained from extreme daily precipitation in a month (EMXP) for the 21 weather stations. The appropriate distribution for each weather station was then determined by evaluating the rank–statistics of Kolmogorov–Smirnov (Chakravarti and Laha 1967), Anderson–Darling (Stephens 1974), and Chi–Squared (Greenwood and Nikulin 1996) tests, as explained in the following subsections.

VI.1.2.1 *Kolmogorov–Smirnov Test*

The Kolmogorov–Smirnov Test is based on the empirical cumulative distribution function. The Kolmogorov–Smirnov statistic (D_n) is defined as the supremum of the difference between the theoretical and the empirical cumulative distribution functions, as shown in equation 3.

$$D_n = \sup_x \left| F_n(x) - F(x) \right| \tag{3}$$

where $F_n(x)$ is the empirical CDF for a random sample x_1 , x_2 , ……. , x_n $\left[F_n(x)=\frac{1}{n}\times\{Number\ of\ Observations \leq x\}\right]$.

VI.1.2.2 *Anderson–Darling Test*

The Anderson–Darling test is used to determine if the sample data follows the population with the expected cumulative distribution function. The Anderson–Darling statistic (A^2) is based on the quadratic empirical distribution function, as shown in equation 4.

$$A^2=-n-\frac{1}{n}\sum_{j=1}^{n}(2j-1)+\left[\ln F(X_i)+\ln\left(1-F(X_{n-i+1})\right)\right] \tag{4}$$

where F is the fitted CDF.

VI.1.2.3 *Chi–Squared Test*

The Chi–Squared test is developed for the continuous sample data. The Chi–Squared statistic (χ^2) is based on the grouping of data into k number of bins of equal probability, as shown in equation 5.

$$\chi^2=\sum_{i=1}^{k}\frac{(O_i-E_i)^2}{E_i} \tag{5}$$

where O_i is the observed frequency, and E_i is the expected frequency $\left[E_i=F(x_2)-F(x_1)\text{ where } x_1,x_2 \text{ are limits of } i\right]$.

VI.2 Research Objective II

VI.2.1 Differentiated Correlation Analysis

Correlation analysis was done for the maximum daily precipitation within a year ($P_{extreme}$) and Atlantic and Pacific Ocean related climatic cycles (AMO, NAO, PDO, PNA, and SOI) using Pearson's correlation coefficient (Press et al. 1992). Since the main aim of this research objective was to investigate the respective relationships with annual precipitation extremes, $P_{extreme}$ data was differentiated using an appropriate probability distributions (Appendix A) into three ranges of probability of occurrence: (i) $\text{Return Period}_{P_{Extreme}}$ > 2 years, (ii) $\text{Return Period}_{P_{Extreme}}$ > 5 years, and (iii) $\text{Return Period}_{P_{Extreme}}$ > 10 years. The limited number of data points prevents further differentiation of $P_{extreme}$ for the correlation analysis. The fitted distributions were ranked using the aforementioned Kolmogorov–Smirnov, Anderson–Darling, and Chi–Squared tests, and the $P_{extreme}$ dataset was differentiated using the inverse CDF of the top–ranked probability distribution. The correlation coefficient was then calculated for each range.

VI.2.2 Weighted Average Correlation Analysis

The Pearson correlation coefficient described in Section VI.2.1 is affected by data outliers, as the sample means are sensitive to them (Kim and Fessler 2004). The effect is further intensified for the matrix of $P_{extreme}$, because of the fewer number of data points. Niven and Deutsch (2012) illustrated a method to estimate a robust correlation coefficient using the weighted average correlation approach through Leave–One–Out–Test (LOOT). For this research objective, the same approach was used to estimate the correlation coefficient for every range of extreme precipitation ($\text{Return Period}_{P_{Extreme}}$

greater than 2, 5, and 10 years) of every weather station mentioned in Chapter V. The methodology to ascertain correlation coefficients using LOOT method was as follows:

Step 1: Calculate the Pearson Correlation coefficient for a dataset of length *n*.

Step 2: Calculate the Pearson Correlation coefficient for the dataset after removing one of its entries. Reiterate the step *n* number of times for each entry.

Step 3: Determine the weight of each correlation coefficient using equation 6:

$$w_i = \left| r_a - r_i^{LOOT} \right|^{\beta} \tag{6}$$

where r_a is the actual correlation coefficient calculated in Step 1, r_i^{LOOT} is the correlation coefficient calculated in Step 2 after removing i^{th} data entry, and β is the weighing exponent determined by equation 7:

$$\beta = \begin{vmatrix} 1 + \dfrac{n}{12} \; \forall \beta \leq 15 \\ 15 \end{vmatrix} \tag{7}$$

It has to be noted here that the value of β is restricted to 15 due to computational limitations.

Step 4: Calculate the weighted average correlation (r_w^{LOOT}) using equation 8:

$$r_w^{LOOT} = \frac{\sum_{j=1}^{n} w_j r_j^{LOOT}}{\sum_{j=1}^{n} w_j} \tag{8}$$

VI.2.3 Uncertainty in Correlation Coefficients

The fewer number of $P_{extreme}$ data points leads to an uncertainty in the calculated correlation coefficient, and the band of uncertainty depends on both the number of data points and the calculated value of a correlation coefficient (Kalkomey 1997). The randomness of samples deviate the sample correlation from the calculated correlation. In the case of $P_{extreme}$ dataset, this randomness was incorporated by defining the sample correlation coefficient at 95% confidence interval, using the sample correlation distribution derived by the Fisher (1915) method (Equation 9).

$$P(c)=\left[\frac{(n-2)\Gamma(n-1)\left\{1-\left(r_w^{LOOT}\right)^2\right\}^{\frac{n-1}{2}}\left(1-c^2\right)^{\frac{n-4}{2}}}{\sqrt{2\pi}\,\Gamma\left(n-\frac{1}{2}\right)\left(1-r_w^{LOOT}c\right)^{\frac{2n-3}{2}}}\right]\times {}_2F_1\left(\frac{1}{2},\frac{1}{2},\frac{2n-1}{2},\frac{r_w^{LOOT}c+1}{2}\right) \tag{9}$$

where *n* is the number of data points, r_w^{LOOT} is the weighted average correlation in Section VI.2.2, *c* is the calculated correlation, $\Gamma(\ )$ is the gamma function, and ${}_2F_1$ is the hyper–geometric function given in equation 10:

$${}_2F_1(i,j,k,z)=\sum_{n=0}^{\infty}\frac{(i)_n(j)_n}{(k)_n}\frac{z^n}{n!} \tag{10}$$

where $(x)_n$ is the Pochhammer symbol: $(x)_n=x(x+1)(x+2)...(x+n-1)$.

VI.2.4 Spatial Interpolation of Correlation Coefficients

The Inverse Distance Weighted (IDW) interpolation method was employed to spatially interpolate the robust correlation coefficients for the state of Texas. IDW works on the principle that each station has a local influence, which decreases with longer distances (De By 2001). It creates a raster surface by averaging the correlation coefficients of each weather station data in its vicinity. A general form of the spatial interpolation method is shown in equation 11. The method is governed by its weighting factor, which itself depends on the user–defined denominator power factor '*p*'. To attain the significant interpolation results for this research objective, the value of power factor was kept as 2 (Lu et al. 2010).

$$r_i = \frac{\sum_i \left(r_w^{LOOT}\right)_i \omega\left(d_i\right)}{\sum_i \omega\left(d_i\right)} \tag{11}$$

where r_w^{LOOT} is the weighted average correlation in Section VI.2.2, $\omega\left(d_i\right)$ is the IDW weighting factor $\left[\omega\left(d_i\right) = \frac{1}{d_i^{\,p}}\right]$ and d_i is the distance from the known weather station.

VI.3 Research Objective III

In order to assess the sensitivity of annual precipitation extremes to the most correlated climatic cycles in different climate regions of Texas, sensitivity indices were determined using the linear least square regression function devised by Bouwer et al. (2008). The uncertainty (with 95% confidence bounds) in indices was analyzed for both integrated and differentiated analyses for each region. The study also quantified the spatial variation of indices with changing hydrometeorological attributes of weather stations. These attributes were interpolated for the region using the above mentioned IDW interpolation method. The analysis concludes with an assessment of empirical probability of occurrence of increased annual precipitation extremes with certain changes in the state of the most correlated climatic cycle. These empirical probability values were obtained by extrapolating the historical trends.

VI.3.1 Linear Least Square Regression

This study determined the sensitivity indices (β_1) using the simple linear least square regression (Bouwer et al. 2008), as shown in equation 12:

$$\ln\left(P_{extreme}^{i}\right)=\beta_0+\beta_1\left(CC_i\right)+\varepsilon_i \tag{12}$$

where CC_i is the state of most correlated climatic cycle, $P_{extreme}^{i}$ is the annual precipitation extreme, β_0 and β_1 are the coefficients, and ε_i is the residual. Here, $100\times\beta_1$ represents the percentage change in $P_{extreme}^{i}$ with a unit change in CC_i.

VI.3.2 Probability Distributions and Plotting Positions

For this research objective, we ranked the probability distributions for different climate regions of Texas, derived in Section VI.1.2, on the basis of Kolmogorov–Smirnov, Anderson–Darling, and Chi–Squared tests to determine the empirical probability of occurrence of historical and projected annual precipitation extremes in different climate regions of Texas in the following steps.

Step 1: Obtain the empirical probability distribution of annual precipitation extremes for a weather station using plotting positions (Cunnane 1978), as shown in equation 13.

$$\mathrm{Pr}_i=\frac{R_i-\alpha}{N+1-2\alpha} \tag{13}$$

where Pr_i is the empirical probability of occurrence, R_i is the rank of annual precipitation extreme (in the descending order of respective historical data), N is the total number of annual precipitation extremes, and α is the theoretical constant. Here, value of α is dependent on the top–ranked probability distribution by the aforementioned statistical tests.

Step 2: Derive upon a theoretical linear relationship between empirical probability of occurrence, function incorporating shape and scale parameters of the top–ranked distribution, and annual precipitation extremes.

Step 3: Determine the empirical probability of occurrence of historical and projected annual precipitation extremes, as per the consequent trendline, sensitivity index and certain change in the most correlated climatic cycle.

CHAPTER VII

RESULTS AND DISCUSSION

VII.1 Research Objective I

Figure 7 illustrates the long–term trend of 12–month SPI values along with total annual precipitation between 1971 and 2010 for 21 weather stations (Chapter V). The SPI curve shows alternative wet and dry cycles for the period of 40 years, but a close observation shows an intensified meteorological cycle for most of the stations with shortened periodicity of excess precipitation years, larger width of wet periods, and strengthened amplitude of SPI values in the last two decades. The average number of wet years in a decade increased from 4.9 years in 1971–1980 to 5.6 years in 2001–2010, with a peak of 5.9 years in 1991–2000. The average high of 12–month SPI values also showed a gradual increase from 1.3 in 1971–1980 to 1.8 in 2001–2010, with 8 weather stations demonstrating extremely wet years corresponding to the values exceeding 2.0 in the last decade (2001–2010) in comparison to only 4 weather stations illustrating the same for the entire period of 1971–2000.

The variation of 3–month SPI values and extreme precipitation events is discussed with respect to the season classification: (i) *December to February (DJF)*: Winter Season, (ii) *March to May (MAM)*: Spring Season, (iii) *June to August (JJA)*: Summer Season, and (iv) *September to November (SON)*: Autumn Season. The decadal variation of the total number of wet seasons categorized by the range of SPI thresholds (Table 1) is shown in Figure 8, and the total number of extreme precipitation events of the order of recurrence intervals listed in Table 2 is plotted in Figure 9 for the climate regions of Texas. Table 3 lists the thresholds of these events for each weather station along with their respective highest rank probability distribution and test statistics. The overall intensification or weakening of seasonal climate over the decades is attributed to the changing temperature–related variables (Chapter V) of the respective climate region. Tables B–1 to B–9 in Appendix B showcase the historical variation of average precipitation per season in the decade for different climate regions (for the range of SPI thresholds). Further, the respective variations in the seasonal temperature–related variables over the decades are listed from Table B–10 to B–18.

VII.1.1 Cold Desert/Semi–Arid Climate Region

The climate region showed an overall decline in the total number of moderately wet seasons between 1971–1990 and 1991–2010, as shown in Figure 8a. For all the four decades, the maximum number of moderately wet periods was observed in the spring season (MAM), followed by the summer season (JJA) for 1971–2000, and the winter season (DJF) for 2001–2010. The total number of moderately wet MAM seasons reduced from 77 in 1971–1990 to 64 in 1991–2010, but the magnitude of average precipitation per season increased from 2.7 in. to 3.2 in. for the respective time periods. In terms of average precipitation, for moderately wet periods, the JJA season was further found to be the dampest amongst all. Inspite of the sudden decline in the number of moderately wet seasons from 37 in 1971–1980 to 28~29 (per decade) for the period 1981–2010, the average precipitation per season in the decade increased from 6.3 in. in 1971–1980 to 7.6 in. for the period of 1981–2010. On the other hand, the winter

Table 3: Fitted probability distributions for weather stations of Texas

S. No.	Weather Station	Probability Distribution	Probability Distribution Test Statistic			Precipitation Thresholds (*in*)		
			Kolmogorov–Smirnov	Anderson–Darling	Chi–Squared	Recurrence Interval (*years*)		
						2	6	44
1	Amarillo	Wakeby	0.062	0.195	0.844	2.04	2.98	4.90
2	Lubbock	Wakeby	0.058	0.188	0.702	2.05	2.99	5.63
3	Midland	Log–Pearson 3	0.080	0.249	1.734	1.84	2.73	4.07
4	Tulia	Wakeby	0.071	0.241	3.304	2.05	3.09	5.22
5	Abilene	Inv. Gaussian (3P)	0.071	0.188	0.778	2.51	3.98	6.72
6	Childress	Wakeby	0.082	0.280	0.559	2.36	3.30	5.16
7	Dallas	Gumbel Max	0.065	0.231	0.446	3.13	4.37	6.18
8	Putnam	Log–Gamma	0.081	0.498	0.123	2.55	3.92	6.72

Table 3 Continued.

S. No.	Weather Station	Probability Distribution	Probability Distribution Test Statistic			Precipitation Thresholds (*in*)		
			Kolmogorov –Smirnov	Anderson –Darling	Chi–Squared	Recurrence Interval (*years*)		
						2	**6**	**44**
9	Waco	Wakeby	0.063	0.148	1.290	3.09	4.28	7.08
10	College Station	Dagum (4P)	0.049	0.151	0.223	3.45	4.90	7.49
11	Texarkana	Wakeby	0.058	0.181	2.084	3.69	4.91	5.69
12	El Paso	Wakeby	0.053	0.128	0.768	1.25	1.81	2.55
13	Panther Junction	Wakeby	0.061	0.152	1.085	1.84	2.40	3.36
14	Amistad	Wakeby	0.081	0.290	4.058	2.66	4.56	7.17
15	Bertram	Burr	0.068	0.124	0.104	3.10	4.79	9.30
16	Austin	Wakeby	0.056	0.150	0.862	3.19	4.93	7.28

Table 3 Continued.

S. No.	Weather Station	Probability Distribution	Probability Distribution Test Statistic			Precipitation Thresholds (*in*)		
			Kolmogorov–Smirnov	Anderson–Darling	Chi–Squared	Recurrence Interval (*years*)		
						2	**6**	**44**
17	Corpus Christi	Log–Pearson 3	0.058	0.156	0.381	3.78	5.89	9.31
18	Elgin	Wakeby	0.052	0.110	1.436	3.12	4.69	6.62
19	San Antonio	Wakeby	0.062	0.162	1.329	3.44	5.60	10.15
20	Houston	Dagum	0.105	0.404	0.978	4.10	6.56	12.77
21	Port Arthur	Wakeby	0.040	0.090	0.318	4.84	7.14	10.98

season (DJF) exhibited a constant rise both in the number and average of moderately wet periods from 22 wet seasons with an average of 1.7 in. in 1971–1980 to 29 wet seasons with an average of 3.2 in. in 2001–2010.

The climate region observed no significant change in the total number of considerably wet periods; however, remarkable seasonal variations are illustrated in Figure 8b. The maximum number of considerably wet periods in 1971–1990 was observed in the autumn season (SON), but the seasonal regime showed a decline for the period of 1991–2010 with a reduction in the total number of wet seasons from 33 to 18 and average precipitation per season in a decade from 11.0 in. to 10.7 in. The decade of 1981–1990 showed a sudden rise in the total number of considerably wet periods, mainly attributed to an approximate 250% increment for the winter season (DJF), spring season (MAM), and summer season (JJA). However, the average precipitation per season in the decade increased only for the DJF season from 2.3 in. to 3.8 in., whereas other seasons observed a 10~40% decline. The changes in the overall trend of DJF and JJA seasons were found to be insignificant in comparison with the intensified meteorology of the MAM season. The MAM season observed 13 wet periods with an average precipitation of 2.9 in. per season for the period of 1971–1990, and 21 wet periods with an average precipitation of 5.0 in. per season for the period of 1991–2010.

Unlike the moderately and considerably wet periods, the climate region observed a sharp three–fold increase in the total number of extremely wet seasons between the periods 1971–1990 and 1991–2010, as shown in Figure 8c. This increase was further observed because of the intensified meteorology of the winter season (DJF) and the spring season (MAM). In the case of the DJF season, the region observed 10 extremely wet periods with an average precipitation of 4.7 in. per season for the period of 1991–2010, in comparison to 2 extremely wet periods with an average precipitation of 5.0 in. per season for the period of 1971–1990. In the case of the MAM season, the extremely wet periods increased from 2 in 1971–1990 to 9 in 1991–2010, but the average precipitation per season for the respective periods differed by merely 0.6 in. On the other hand, the summer season (JJA) and autumn season (SON) showed no significant change in the total number of extremely wet periods; however, the average precipitation per season in a decade increased from 7.0 in. to 13.3 in. for the former and decreased from 15.3 in. to 9.3 in. for the latter for the periods between 1971–1990 and 1991–2010.

Figures 9a–9c illustrate that the climate region was likely to observe one–day extreme precipitation events of the order of SPI thresholds in the summer season (JJA) and autumn season (SON). No significant difference was detected in the total number of low–range extreme precipitation events (2 years $\leq$ Recurrence Interval < 6 years) in the JJA season, however the SON season observed a sudden decline: from 30 events in 1971–1990 to 17 events in 1991–2010. During 1971–1990, the low–range extremes occurred with an average of 2.3 in. and at an average periodicity of 1.9 years, with a maximum of 3.3 years and a minimum of 1.3 years. Further, during 1991–2010, the low–range extremes occurred with the same average but with an average periodicity of 2.3 years, with a maximum of 3.0 years and a minimum of 1.5 years. On the other hand, the mid–range extreme precipitation events (6 years $\leq$ Recurrence Interval < 44 years) doubled for the JJA season and halved for the SON season between the periods 1971–

1990 and 1991–2010. With no significant change in the average magnitude of events, the former observed events at an average interval of 4.7 years, with a maximum of 11.8 years and a minimum of 0.8 years, whereas the latter observed events at an average interval of 4.7 years, with a maximum of 8.4 years and a minimum of 1.9 years for the respective time periods. The high–range extreme precipitation events (Recurrence Interval $\geq$ 44 *yrs*) were also intensified, as 5 weather stations observed the events with an average of 5.4 in. (maximum of 7.5 in. and minimum of 2.8 in.) in the period 1991–2010 in comparison to only 2 weather stations, which observed the events with an average of 5.1 in. in the period 1971–1990.

The intensified climate winter season (DJF) in terms of different ranges of wet periods from 1971–1990 to 1991–2010 can be attributed to the rise in average seasonal temperature (T_{avg}–S) from 42.6ºF to 44.4ºF, slight increment in mean of maximum daily temperature in the season (EMXT–S) from 84.8ºF to 85.3ºF, and increased number of days with projected maximum temperature exceeding 90ºF in the season (DX90–S) from 2 to 11, for the respective time periods. The maximum number of moderately wet periods for every decade and significant increment in both considerably and extremely wet periods in the spring season (MAM) are well–explained by the slender rise in T_{avg}–S by 0.8ºF, significant increment in the mean of EMXT–S by 2.3ºF, and 21% increase in the total number of DX90–S for the periods 1971–1990 and 1991–2010. The dampest moderately and considerably wet periods, with a substantial increment in the average seasonal precipitation in extremely wet periods, exhibited double the number of mid–range extreme precipitation events with a significant reduction in respective maximum periodicity, and the increased number and intensity of high–range extreme precipitation events in the summer season (JJA) are mainly attributed to the additional 546 DX90–S days in the period 1991–2010 in comparison to period 1971–1990. On the other hand, the autumn seasons (SON) illustrate a mere increase in T_{avg}–S and DX90–S by 0.5ºF and 3.4% from 1971–1990 to 1991–2010, and a respective decline in EMXT–S by 1ºF, which translated into a decrease in the number of considerably wet periods, average seasonal precipitation in considerably and extremely wet periods, and the number of mid–range extreme precipitation events.

VII.1.2 Humid Sub–Tropical Climate Region

The climate region showed no significant variation in the total number of moderately wet periods amongst different seasons in all the four decades. However, the region observed a slight decline in the total number of moderately wet seasons between 1971–1990 and 1991–2010, as shown in Figure 8d. The summer season (JJA) and autumn season (SON) were found to be significantly wetter than the winter season (DJF) and spring season (MAM). With no major change in the number of moderately wet periods, historically the wettest JJA season observed a decrement in the average precipitation per season in the decade: from 11.9 in. in 1971–1990 to 10.8 in. in 1991–2010. On the other hand, the SON season observed a 19% decline in the total number of moderately wet periods, in spite of the increased average precipitation per season in the decade from 10.8 in. in 1971–1990 to 11.4 in. in 1991–2010. The DJF and MAM seasons further showed an increment of 1 in. in the average precipitation per season in the decade for the respective periods of 1971–1990 and 1991–2010, with no significant variation in the number of moderately wet periods except for the sudden decline for the MAM season in the decade of 2001–2010.

In the case of considerably wet periods, the climate region observed a constant increase from 70 seasons in 1971–1980 to 104 seasons in 2001–2010, as illustrated in Figure 8e. The summer season (JJA) observed the maximum number of considerably wet seasons for all the decades except 1991–2000, followed by the wetter autumn season (SON). In the case of the JJA season, a mere increase in the number of considerably wet periods was observed for the periods of 1971–1990 and 1991–2010, when the average precipitation per season in the decade decreased from 16.6 in. to 14 in., respectively. With no change in the average precipitation per season in the decade, the number of considerably wet periods increased from 41 in 1971–1990 to 55 in 1991–2010 for the SON season. The climatology of the winter season (DJF) and the spring season (MAM) was also found to be significantly intensified, mainly in terms of the number of considerably wet periods; from 19 in 1971–1990 to 42 in 1991–2010 for the former and from 34 in 1971–1990 to 47 in 1991–2010 for the latter. The average precipitation per season in the decade for DJF and MAM seasons observed a slight increase of 0.5 in. from 1971–1990 to 1991–2010.

The extremely wet periods for the climate regions quadrupled between the periods 1971–1990 and 1991–2010, majorly because of the intensified regimes of the winter season (DJF) which observed 17 such periods in the decade 1991–2000, as shown in Figure 8f. Inspite of this hike in the number of extremely wet periods, the average precipitation per season in the decade for DJF season decreased from 19.5 in. in 1971–

1990 to 15.6 in. in 1991–2000. In terms of average precipitation per season in the decade, the summer season (JJA) was found to be extremely wettest amongst all. The JJA season observed 5 extremely wet periods with an average precipitation of 20.4 in. per season in the decade 2001–2010, when the 1971–2000 period historical records for the season showed in total 5 such periods with an average precipitation of 19.0 in. per season in each decade.

The climate region was likely to observe one–day extreme precipitation events of the order of SPI thresholds in the autumn season (SON) and summer season (JJA), as shown in Figure 9d–9f. The meteorological regimes of low–range extreme precipitation events (2 years $\leq$ Recurrence Interval < 6 years) intensified moderately for the SON season, from 53 events in 1971–1990 to 61 events in 1991–2000, but weakened immensely for the JJA season because of the sudden decline in the decade 1991–2000, which merely observed 8 such events. The period 1971–1990 observed the occurrence of these events at a periodicity ranging between 1.0 years and 5.3 years, with an average of 2.2 years, whereas 1991–2010 observed them at a periodicity ranging between 1.2 years and 4.0 years, with an average of 2.0 years. No further significant changes were observed in terms of average magnitude of precipitation for the respective time periods. The region also observed a sudden rise in the total number of mid–range extreme precipitation events (6 years $\leq$ Recurrence Interval < 44 years) between periods 1971–1990 and 1991–2010, both for the SON and JJA seasons. The former observed 19 precipitation events in 1991–2010, in comparison to 9 events in 1971–1990, and latter observed 18 precipitation events in 1991–2010, in comparison to 12 events in 1971–

1990. With no significant change in the average magnitude, 1971–1990 observed the periodicity of 4.6 years (maximum of 11.8 years and minimum of 0.9 years), and 1991–2010 observed the periodicity of 3.7 years (maximum of 8.0 years and minimum of 0.3 years). The high–range extreme precipitation events (Recurrence Interval ≥ 44 years) were further likely to occur in the SON season and remained constant for the period of 1981–2010. Eight weather stations observed events with an average of 8.6 in. (maximum of 13.4 in. and minimum of 5.2 in.) in the period of 1991–2010, in comparison to only 3 weather stations which observed events with an average of 9.2 in. (maximum of 11.8 in. and minimum of 5.3 in.) in the period of 1971–1990.

The winter season (DJF) illustrated a small increase in every temperature–related variable during the periods 1971–1990 and 1991–2000; average seasonal temperature (T_{avg}–S) by 1.9ºF, mean of maximum daily temperature in the season (EMXT–S) by 0.1ºF, and total number of days with projected maximum temperature exceeding 90ºF in the season (DX90–S) by 30%, which resonated with the increased average precipitation per season in the decade for moderately wet periods, doubling the number of considerably wet periods, and immensely intensified regimes of extremely wet periods. The spring season (MAM) showed extremely similar changes in these temperature–related variables from the period 1971–1990 to 1991–2010 as the DJF season, which resulted in increments in average precipitation per season in the decade for moderately wet periods, number of considerably wet periods, and doubling the number of extremely wet periods in the latter two decades. The mere increase in T_{avg}–S and EMXT–S by 0.9ºF and 1.3ºF, coupled with the additional 409 DX90–S days in the period 1991–2010 in comparison to 1971–1990 translated into the observed seasonal climate shift in the summer season (JJA): from moderately and considerably wet periods to extremely wet periods, and from low–range extreme precipitation events to mid– and high–range extreme precipitation events. These extreme precipitation events are also found to be more frequent in the period 1991–2000, in terms of all maximum–minimum–average periodicities, in comparison to the period 1971–1990. Further, the autumn season (SON) illustrates both the strengthened and weakened climatic trends, such as declined number of moderately wet periods with increased average seasonal precipitation, increased number of considerably wet periods with no change in average seasonal precipitation, and increments in extreme precipitation events with no change in extremely wet periods. These seasonal climatic variations are mainly attributed to the slight increase in T_{avg}–S by 1.2ºF, trivial decrease in EMXT–S by 0.1ºF, and a mere 6% increment in DX90–S days from 1971–1990 to 1991–2010.

VII.1.3 Warm Desert/Semi–Arid Climate Region

The climate region showed a constant decadal decline in the total number of moderately wet seasons, as shown in Figure 8g. The maximum numbers of such periods (79) were observed in the spring season (MAM), which was determined to be least wet, followed by the summer season (JJA) (63) which was historically the wettest amongst all seasons. The MAM season further showed no significant change, neither in the total number of moderately wet periods nor in the average precipitation per season in a decade for the periods 1971–1990 and 1991–2010. On the other hand, the JJA season showed a significant decline for the same: the season observed 35 moderately wet periods with an average of 7.6 in. in 1971–1990 and 28 moderately wet periods with an average of 6.0 in. in 1991–2010. In the winter season (DJF), a similar decrement in the total number of moderately wet periods as the JJA season was observed for the periods of 1971–1990 and 1991–2010, with an increment in the average precipitation per season in a decade from 3.6 in. for former to 4.5 in. for latter.

In the climate region, the autumn season (SON) was determined to be historically dampest in terms of considerably wet periods, followed by the summer season (JJA), as shown in Figure 8h. The SON season observed a sharp decline both in the number and intensity of considerably wet periods, from 16 periods with an average of 10.8 in. per decade for 1971–1990 to 10 periods with an average of 8.9 in. per decade for 1991–2010. On the other hand, the JJA season showed no difference in the total number of considerably wet periods, but a slight decline of 0.4 in. in the average precipitation per season in a decade for the periods of 1971–1990 and 1991–2010. The climate observed almost an equal number of considerably wet periods for the winter season (DJF) and spring season (MAM) as the JJA season, where the former observed a decrement in the average precipitation per season in a decade from 3.1 in. in 1971–1990 to 2.8 in. in 1991–2010, and the latter observed an increment in the same from 2.7 in. in 1971–1990 to 3.7 in. in 1991–2010.

The total number of extremely wet periods doubled in the climate region between the time periods of 1971–1990 and 1991–2010, with no major seasonal variations, as shown in Figure 8i. These periods were equally distributed amongst the winter season (DJF), spring season (MAM), and summer season (JJA), where the JJA season was found to be the wettest followed by the DJF season. The average precipitation per season in a decade intensified for the JJA season from 8.7 in. in 1971–1990 to 10.5 in. in 1991–2010, whereas the same declined for the DJF season from 8.0 in. in 1971–1990 to 7.3 in. in 1991–2010. In the case of MAM season, the total number of extremely wet periods increased from 1 in 1971–1990 to 4 in 1991–2010, the former with an average precipitation of 1.0 in. per season in a decade and the latter with an average precipitation of 3.8 in. per season in a decade.

The climate region historically observed one–day extreme precipitation events of the order of SPI thresholds in the summer season (JJA) and autumn season (SON), as shown in Figures 9g–9i. Both seasons observed a sharp decline in the total number of low–range extreme precipitation events (2 years $\leq$ Recurrence Interval < 6 years) between the periods of 1971–1990 and 1991–2010; the former with a difference of 10 events and the latter with 5 events in the respective periods. The region observed no significant change in the average precipitation, however, the frequency of these events varied for the time periods, with periodicity ranging between 1.5 years and 1.9 years with an average of 1.7 years for the period 1971–1990, and between 1.7 years and 2.7 years with an average of 2.2 years for the period of 1991–2010. Unlike these events, the total mid–range extreme precipitation events (6 years $\leq$ Recurrence Interval < 44 years) increased for both the seasons, mainly in the JJA season which observed 6 events in the period of 2001–2010, when the historical record only had 3 such events in the season in the period 1971–2000. Further, with no significant difference in the average magnitude of precipitation, these extremes were also found to be even more spaced out in the data:

the average periodicity for the period 1971–1990 was determined to be 4.4 years with a maximum of 8.0 years and a minimum of 0.8 years, which eventually increased to 5.3 years with a maximum of 8.4 years and a minimum of 3.0 years for the period 1991–2010. Both of these time periods also witnessed a sole high–range extreme precipitation event (Recurrence Interval $\geq$ 44 years), the former of intensity 10.4 in. and latter of 2.8 in.

The winter season (DJF) observed an increment in the average seasonal temperature (T_{avg}–S) from 48.9ºF to 51.0ºF, mean of maximum daily temperature in the season (EMXT–S) from 85.8ºF to 86.5ºF, and total number of days with projected maximum temperature exceeding 90ºF in the season (DX90–S) by a day for the periods 1971–1990 and 1991–2010. These enhanced temperature–related variables resulted in seasonal shift in climatic regimes, with a decrement in moderately and considerably wet periods, and a corresponding significant increment in extremely wet periods. From 1971–1990 to 1991–2010, the spring season (MAM) illustrated no variation in moderately wet periods, increased average precipitation in considerably wet periods, and increments in both the number and the intensity of extremely wet periods, which resonate well with the increased T_{avg}–S by 1.5ºF, EMXT–S by 2.2ºF, and DX90–S days by 21%. Similar to DJF seasonal climate shift, the summer season (JJA) observed a decrement both in the number and the intensity of moderately wet periods, a decline in the average seasonal precipitation, and the reduced number of low–range extreme precipitation events from 1971–1990 to 1991–2010, but illustrated a significant rise in the dampest extremely wet periods and mid–range extreme precipitation events. This climatic shift can be attributed to the intensified seasonal temperature–related variables: T_{avg}–S by 1.8°F, EMXT–S by 0.5°F, and DX90–S days by 5%, for the respective time periods. Lastly, from 1971–1990 to 1991–2010, the autumn season (SON) illustrated an increment in T_{avg}–S from 66.1ºF to 67.5ºF, EMXT–S from 100.2ºF to 100.3ºF, and DX90–S days from 550 to 585 days, which mainly translated to no significant variations in moderately and extremely wet periods, mere decline in regimes of considerably wet periods and low–range extreme precipitation events, and slight rise in number of mid–range extreme precipitation events.

.

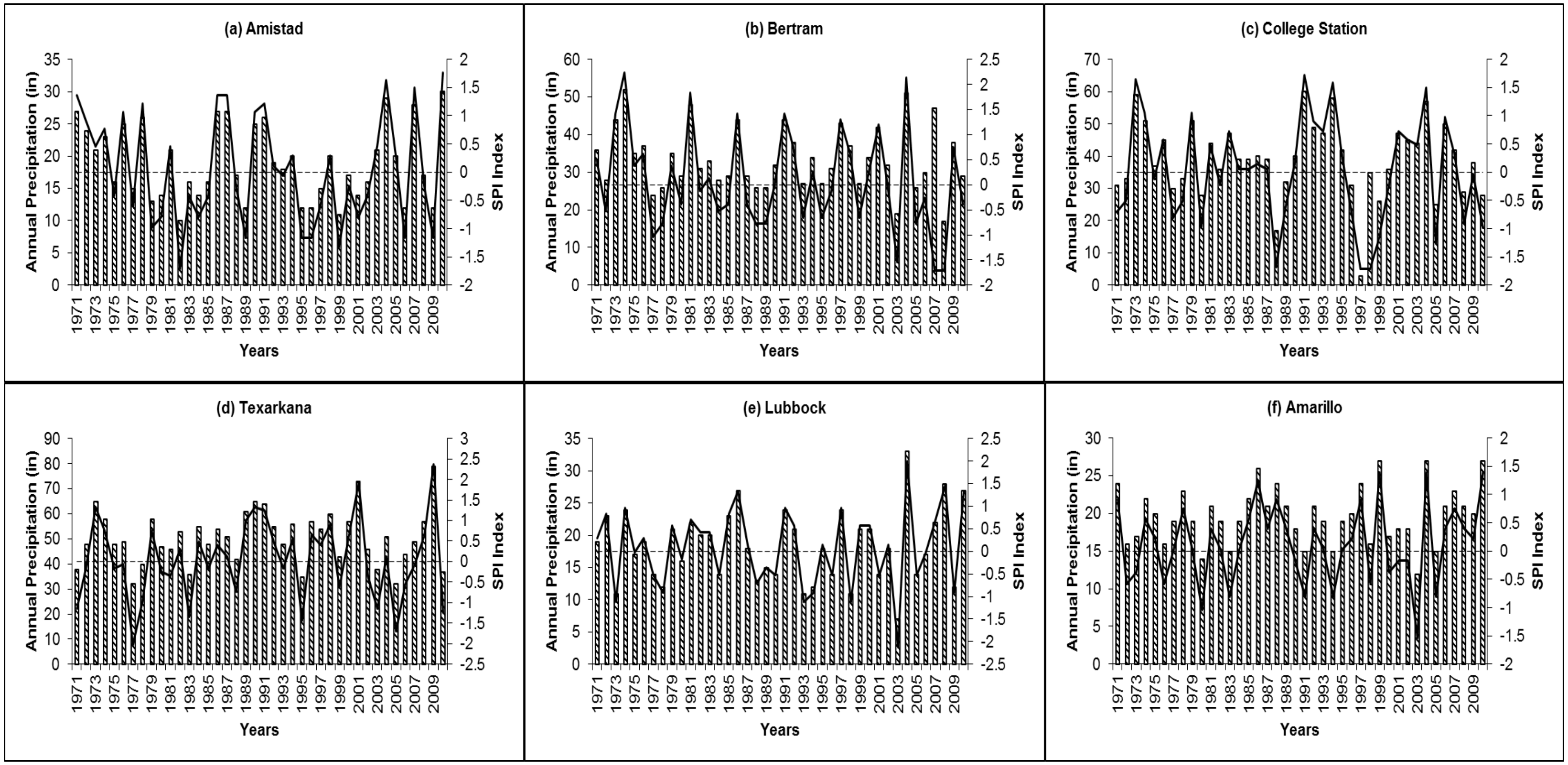

Figure 7: Annual precipitation trends in Texas

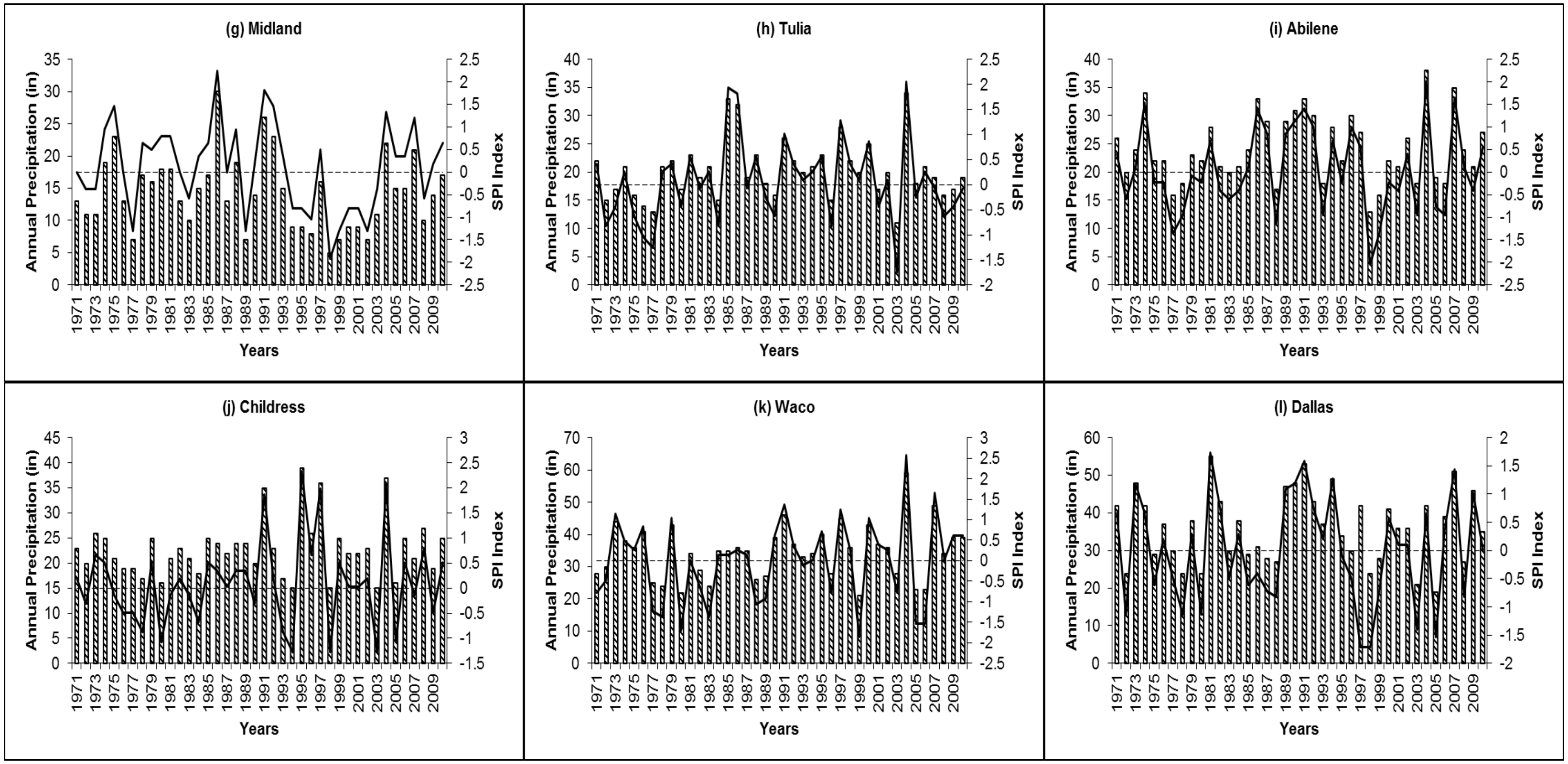

Figure 7 Continued.

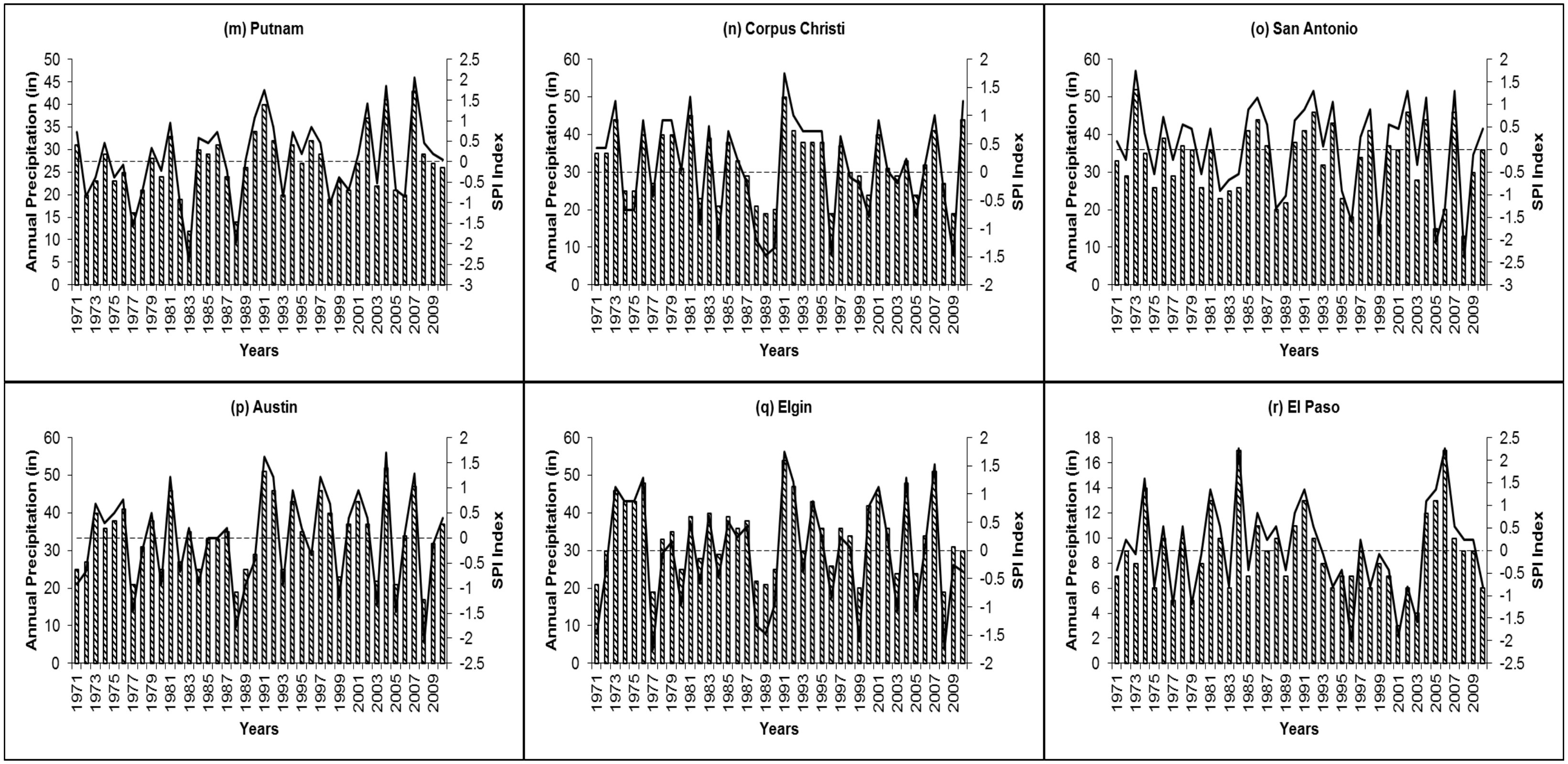

Figure 7 Continued.

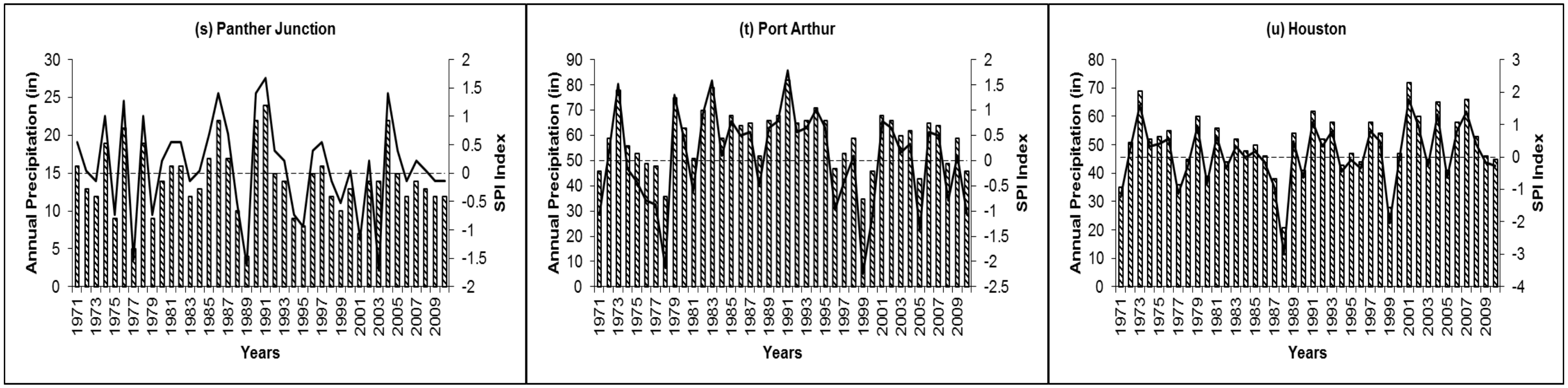

Figure 7 Continued.

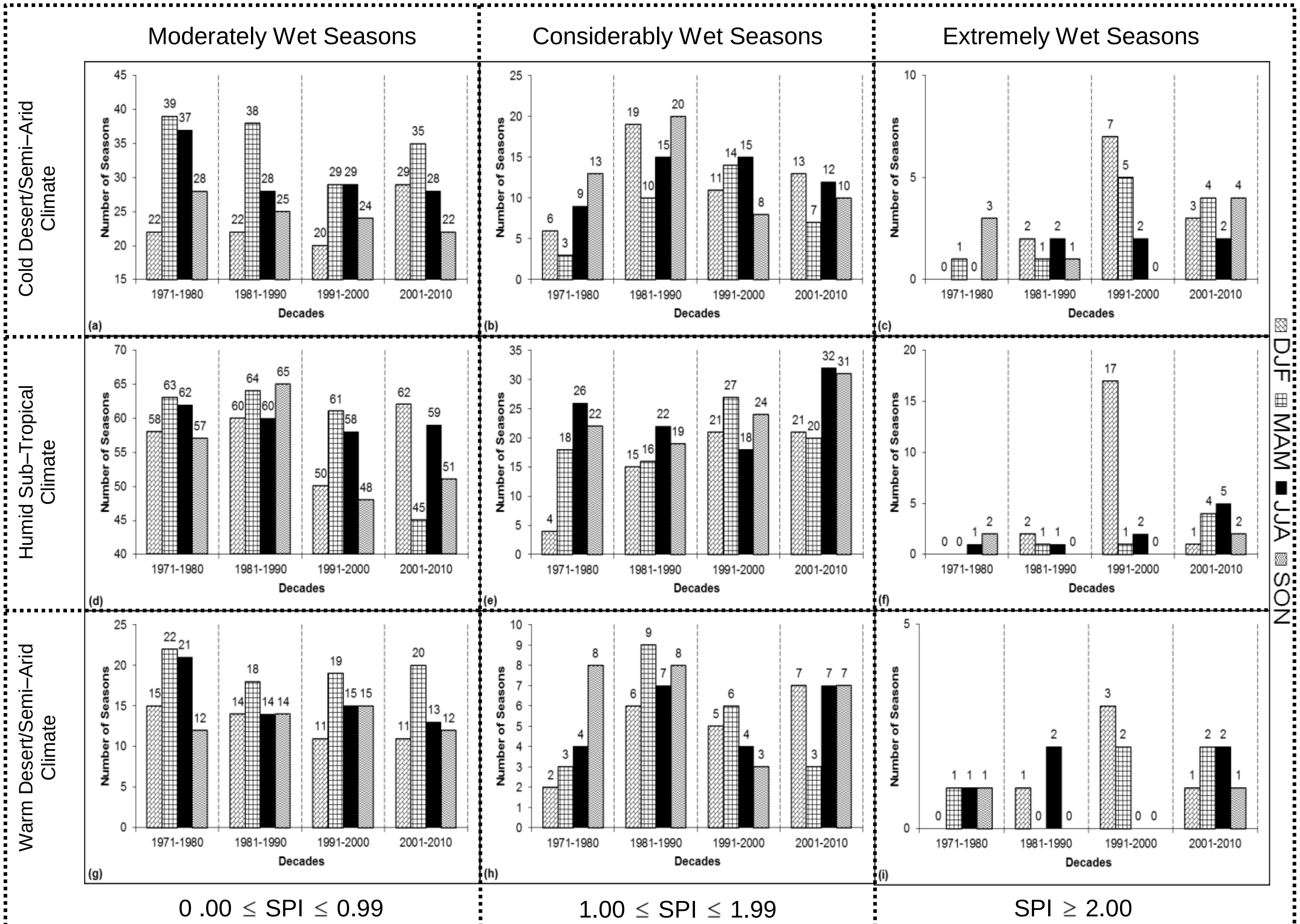

Figure 8: Decadal variation of wet seasons in Texas climate regions

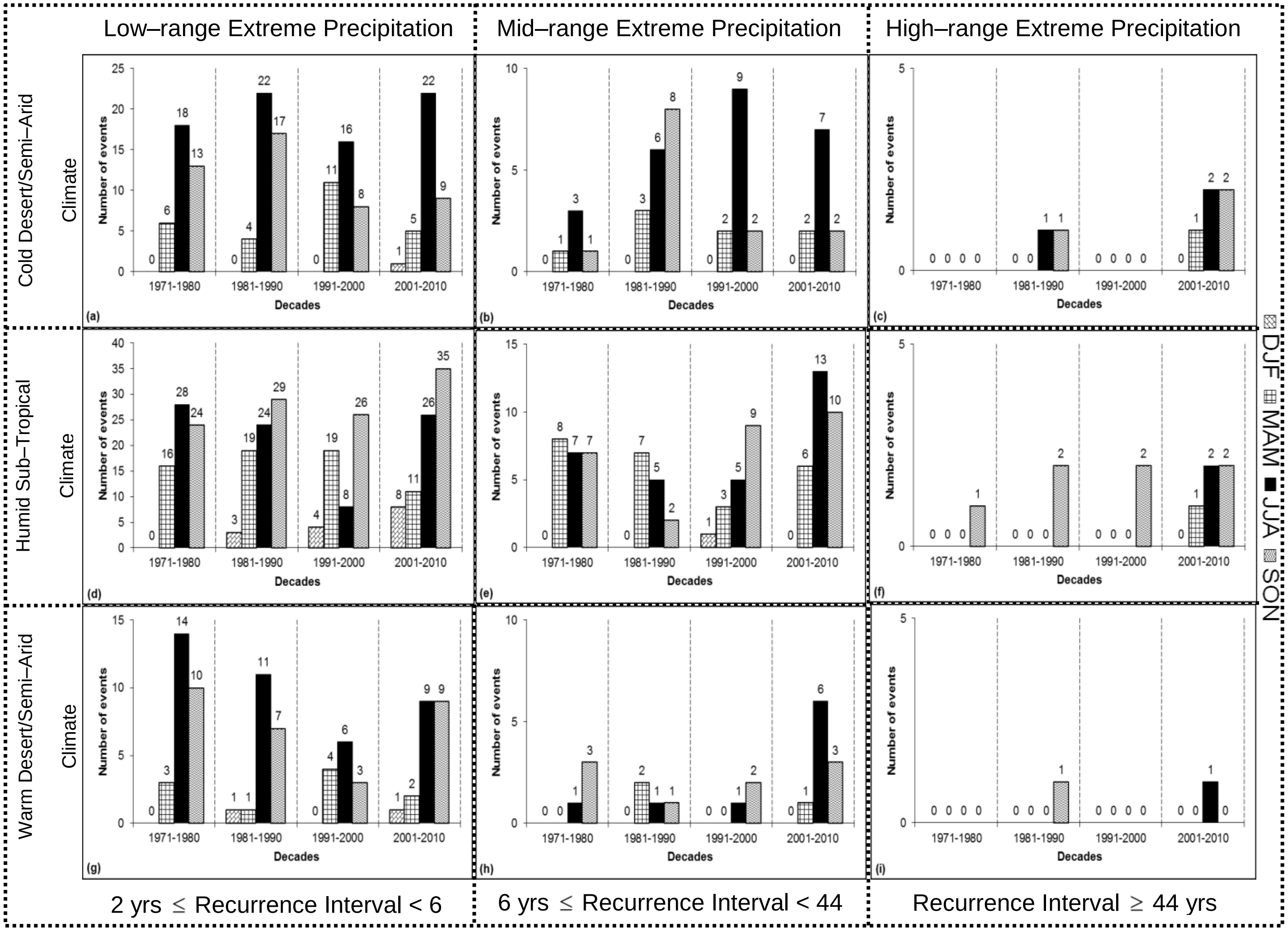

Figure 9: Decadal variation of extreme precipitation events in Texas climate regions

VII.2 Research Objective II

VII.2.1 Extraction of Precipitation Extremes for Texas Climate Divisions

Table 4 lists the fitted probability distributions for each Texas Climate Division delineated by National Climatic Data Center (NCDC), along with the respective statistics and ranking of Kolmogorov–Smirnov, Anderson–Darling, and Chi–Squared tests, and thresholds of each range of annual extremes.

VII.2.2 Relationship of Precipitation Extremes with Climatic Cycles

The statistical links between the annual precipitation extremes and Atlantic and Pacific Ocean based Climatic Cycles were analyzed using the weighted correlation approach explained in Section VI.2.2 for the various climate regions of Texas. In order to attain a comprehensive understanding of the impact of climatic cycles on the annual precipitation extremes, the absolute value of respective correlation coefficient greater than or equal to 0.6 is considered to be highly significant, and less than or equal to 0.2 is considered to be weak (Curtis 2008, Kurtzman and Scanlon 2007). Previous studies, such as Ropelewski and Halpert (1996), Lü et al. (2011), etc., quantified the relationship of climatic cycles and hydrologic processes without differentiating the hydroclimatic variable in ranges of recurrence intervals. These studies resulted in considerably weaker correlation coefficients at the appropriate time lags (i.e., 0.2 $\leq$ Correlation Coefficients $\leq$ 0.6) as the climate anomalies generated by these cycles mainly contributed to hydrometeorologic extremes. It can be observed from Figure 10 that only the $P_{extreme}$ data with a return period of greater than 10 years was found to be significantly affected by the Atlantic and Pacific Ocean related climatic cycles.

Table 4: Goodness–of–fit summaries for Texas climate divisions delineated by NCDC

NCDC Climate Division	Weather Station	Probability Distribution	Statistical Performance			Annual Extremes Thresholds (*in*)		
			Kolmogorov–Smirnov	Anderson–Darling	Chi–Squared	Return Period > (*years*)		
						2	5	10
East Texas	Henderson	Dagum (4–Parameter)	0.066	0.157	1.965	3.416	4.669	5.649
	New Caney	Generalized Extreme Value	0.040	0.098	0.118	4.189	5.824	6.996
Edwards Plateau	Del Rio	Burr (4–Parameter)	0.070	0.352	2.896	2.665	4.076	5.048
	Taylor Ranch	Wakeby	0.046	0.179	2.972	2.929	4.104	5.212
High Plains	Amarillo	Wakeby	0.056	0.178	1.226	1.984	2.725	3.335
	Dalhart	Wakeby	0.057	0.170	0.554	1.691	2.349	2.869
	Midland	Log Pearson 3	0.074	0.221	1.974	1.859	2.644	3.19

Table 4 Continued

NCDC Climate Division	Weather Station	Probability Distribution	Statistical Performance			Annual Extremes Thresholds (*in*)		
			Kolmogorov–Smirnov	Anderson–Darling	Chi–Squared	Return Period > (*years*)		
						2	5	10
High Plains	Pampa	Gamma	0.077	0.352	2.789	2.041	2.643	2.999
	Slaton	Burr (4–Parameter)	0.049	0.161	2.024	2.249	3.078	3.636
Low Rolling Plains	Childress	Wakeby	0.077	0.256	1.631	2.277	2.961	3.546
	Roscoe	Burr	0.063	0.160	0.650	2.577	3.549	4.395
North Central	Dallas	Error	0.067	0.266	0.798	2.984	3.696	4.049
	Dawson	Log–Gamma	0.061	0.244	1.230	3.376	4.596	5.499
	Ennis	Dagum (4–Parameter)	0.051	0.178	1.005	3.27	4.542	5.501
	Proctor	Johnson SB	0.064	0.139	0.148	3.23	4.653	5.605

Table 4 Continued

NCDC Climate Division	Weather Station	Probability Distribution	Statistical Performance			Annual Extremes Thresholds (*in*)		
			Kolmogorov–Smirnov	Anderson–Darling	Chi–Squared	Return Period > (*years*)		
						2	5	10
North Central	Putnam	Burr (4–Parameter)	0.072	0.320	0.786	2.599	3.667	4.468
	Rainbow	Generalized Extreme Value	0.070	0.334	1.400	3.108	4.278	5.083
	Waco	Generalized Logistic	0.077	0.164	0.342	2.986	3.853	4.46
South Central	Austin	Wakeby	0.062	0.187	0.339	3.084	4.351	5.281
	Elgin	Wakeby	0.060	0.145	2.428	3.118	4.264	5.168
	San Antonio	Generalized Logistic	0.534	0.177	0.328	3.307	4.856	6.141
Trans Pecos	Big Bend	Wakeby	0.052	0.173	1.029	1.833	2.325	2.649

Table 4 Continued

NCDC Climate Division	Weather Station	Probability Distribution	Statistical Performance			Annual Extremes Thresholds (*in*)		
			Kolmogorov–Smirnov	Anderson–Darling	Chi–Squared	Return Period > (*years*)		
						2	5	10
Trans Pecos	El Paso	Pearson 6 (4–Parameter)	0.066	0.216	0.499	1.252	1.681	1.951
	Mount Locke	Generalized Extreme Value	0.065	0.179	0.709	1.777	2.327	2.694
Upper Coast	Cleveland	Inverse Gaussian (3–Parameter)	0.054	0.189	1.703	4.039	5.809	7.123
	Palacios	Wakeby	0.061	0.214	2.034	4.807	6.453	7.474

Both the cold and warm desert/semi–arid climate regions were found to be highly impacted by the variations in the North Atlantic Oscillation (NAO). The humid sub–tropical climate region of Texas was found to be mainly influenced by the phases of the Atlantic Multidecadal Oscillation (AMO). The respective positive (negative) relationship defines either a higher mean or number of events of annual precipitation extremes in the warm (cold) phase of the respective climatic cycle, as summarized in Table 5–7. A few weather stations with extremely insignificant correlation coefficients were discarded for further analysis.

The AMO is known to define basin–scale SST anomalies in the North Atlantic region. On a broad scale, the warm phase of AMO responds with severe negative precipitation anomalies for North America, and the cold phase of AMO results with an above–average precipitation for the entire contiguous United States (Hu and Feng 2012). Murgulet et al. (2012) investigated the relationship of precipitation in Southern Texas and Atlantic and Pacific Ocean related climatic cycles, and concluded with strong inverse relationship between higher precipitation intensities and cold phase of AMO. Much of the extreme precipitation events in the humid sub–tropical climate region of Texas took place in summertime, and certain prevailing regional–scale circulation regimes of AMO are found to significantly impact the summertime precipitation in North America, especially the southwestern United States (Sutton and Hodson 2007, Hu and Feng 2008). During the cold phase of AMO, the seasonal rainfall is restrained to the southwestern United States because of the frequent northwesterly wind anomalies.

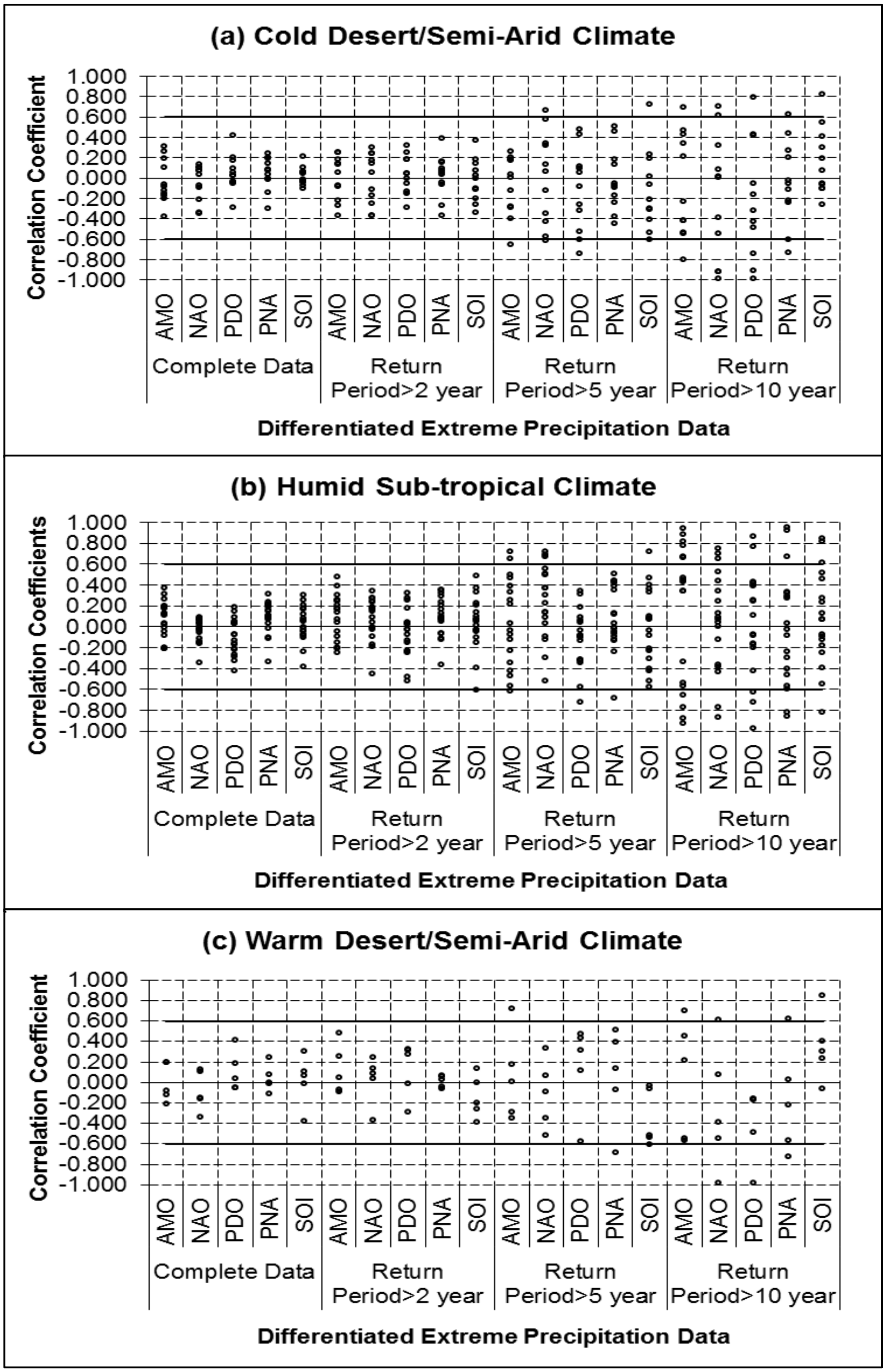

Figure 10: Correlation coefficients for the differentiated annual extreme precipitation ($P_{extreme}$) data for Texas climate regions

Further, the strong southerly low–level flow from the Gulf of Mexico, associated with its sea surface temperature (SST) anomalies, enhances the higher regional precipitation intensities in the phase (Feng et al. 2008). The southern part of Texas can be an exception to the large negative anomalies occurring during the warm phase of AMO for most parts of the Great Plains (Hu et al. 2011). The Atlantic and Gulf of Mexico coastlines of the United States are strongly influenced by the Tropical Cyclone Precipitation (Pielke Jr et al. 2008). AMO warm phases show a strong impact on the sea–surface temperature gradient from the equator poleward. It illustrates a significantly strong relationship with all the attributes of the Tropical Cyclone Precipitation in the southeastern United States (Nogueira and Keim 2010). During the warm phase of AMO, the cyclonic activity over the North Atlantic warm–pool region weakens the clockwise rotation of low–level winds around the North Atlantic subtropical high pressure system (NASH), enhancing the summertime precipitation for the southeastern United States (Hu and Feng 2008). Most of the major hurricane landfalls occurred during the warm phase of AMO (Goldenberg et al. 2001): three times higher than the cold phase of AMO, in case of Atlantic hurricanes exceeding category 3 (Sutton and Hodson 2005). The effect of AMO further strengthens (weakens) with the occurrence of El Niño (La Niña) events (Lu and Dong 2005).

The NAO is based on the surface sea–level pressure difference between the Sub–Tropical (Azores) High and the Sub–Polar (Icelandic) Low. The oscillation is known to have key impacts on the climatic regimes of temperature, precipitation, and storms in the Atlantic sector and the surrounding continents (Marshall et al. 2001), and play a central role in anthropogenic climate change. The changes in local surface temperatures in southeastern United States have been strongly influenced by the variations in NAO (Hurrell and Van Loon 1997). The warm phase of NAO, commonly known as Bermuda High, is a principal high pressure system of the North Atlantic Oscillation which influences the formation and path of tropical cyclones as well as climate patterns across Texas and the eastern United States (Lamb and Peppler 1991). During the warm phase, the aforementioned pressure systems are strengthened, leading to an increment in the pressure gradient over the North Atlantic. The phenomenon further results in an increased upper level winds and speed of westerlies, draining off the cold air from North America, and preventing it to move southwards, eventually causing above–average geopotential heights, higher temperatures, stronger storms, and overall wetter atmospheric patterns for the southeastern United States during the winter season. On the other hand, the cold phase of NAO weakens the westerlies, causing the reduced geopotential heights which allow the cold air to build up over Canada and move towards southeastern United States via a deepening trough. The phenomenon further leads to the energy phasing of the intense jet stream interactions, and results in colder and drier seasons for the state of Texas (Parazoo et al. 2015, Hurrell 2002). The NAO is also believed to modulate the site and intensity of Atlantic Meridional Overturning Circulation (MOC). Also, the oscillation rivals the El Niño–Southern Oscillation (ENSO) as the respective NAO warm phase intensifies the warmer temperature for Southeastern United States during the La Niña phase.

Table 5: Summary of the annual precipitation extremes' characteristics (in.) for Texas' Cold Desert/Semi–Arid climate region and its relationship with NAO

NCDC Climate Division	Weather Station	Correlation Coefficient with NAO	NAO–Warm Phase				NAO–Cold Phase			
			Count	Mean	Min	Max	Count	Mean	Min	Max
High Plains	Amarillo	–0.919	3	3.483	3.400	3.580	2	5.330	4.920	5.740
	Midlands	–0.384	1	3.590	3.590	3.590	4	4.073	3.290	4.750
	Pampa	0.321	2	3.480	3.420	3.540	3	3.430	3.390	3.500
	Slaton	–0.918	2	4.205	3.900	4.510	2	5.235	5.070	5.400
Trans Pecos	Big Bend	0.614	2	3.445	3.190	3.700	4	2.995	2.740	3.290
	El Paso	–0.984	3	2.240	2.200	2.260	1	2.840	2.840	2.840

Table 6: Summary of annual precipitation extremes' characteristics (in.) for Texas' Humid Sub–Tropical climate region and its relationship with AMO

NCDC Climate Division	Weather Station	Correlation Coefficient with AMO	AMO–Warm Phase				AMO–Cold Phase			
			Count	Mean	Min	Max	Count	Mean	Min	Max
East Texas	Henderson	–0.537	2	7.195	6.250	8.140	2	9.285	7.520	11.050
	New Caney	0.339	2	9.360	8.500	10.220	2	8.940	8.600	9.280
Edwards Plateau	Del Rio	0.450	4	6.610	5.580	7.110	1	6.250	6.250	6.250
	Taylor Ranch	–0.567	1	7.370	7.370	7.370	3	9.507	5.470	12.270
Low Rolling Plains	Childress	0.468	4	4.425	3.570	5.160	1	5.320	5.320	5.320
	Roscoe	0.343	2	7.265	6.250	8.280	2	5.400	4.600	6.200
North Central	Dallas	0.885	2	4.815	4.390	5.240	2	4.135	4.050	4.220
	Dawson	–0.772	2	6.070	5.960	6.180	3	7.557	5.750	8.950
	Ennis	–0.926	1	6.400	6.400	6.400	4	7.595	6.930	8.200

Table 6 Continued

NCDC Climate Division	Weather Station	Correlation Coefficient with AMO	AMO–Warm Phase				AMO–Cold Phase			
			Count	Mean	Min	Max	Count	Mean	Min	Max
North Central	Proctor	0.428	3	6.947	5.740	8.370	2	6.300	5.850	6.750
	Putnam	0.664	5	5.320	4.660	6.230	3	4.797	4.510	5.000
	Rainbow	–0.339	3	5.827	5.300	6.580	3	5.917	5.750	6.000
	Waco	0.818	3	6.293	5.070	7.980	1	4.470	4.470	4.470
South Central	Austin	0.779	3	6.943	6.240	7.550	3	5.630	5.550	5.680
	Elgin	0.669	2	6.075	6.050	6.100	3	6.700	5.300	9.200
	San Antonio	0.938	2	10.565	9.870	11.260	3	7.440	6.260	9.520
Upper Coast	Cleveland	–0.657	2	7.980	6.960	9.000	2	11.115	9.060	13.170
	Palacios	–0.876	1	8.630	8.630	8.630	4	8.758	8.580	8.910

Table 7: Summary of the annual precipitation extremes' characteristics (in.) for Texas' Warm Desert/Semi–Arid climate region and its relationship with NAO

NCDC Climate Division	Weather Station	Correlation Coefficient with NAO	NAO–Warm Phase				NAO–Cold Phase			
			Count	Mean	Min	Max	Count	Mean	Min	Max
Edwards Plateau	Del Rio	–0.383	1	6.250	6.250	6.250	4	6.610	5.580	7.110
Trans Pecos	Big Bend	0.614	2	3.445	3.190	3.700	4	2.995	2.740	3.290
	El Paso	–0.984	3	2.240	2.200	2.260	1	2.840	2.840	2.840

VII.2.3 Estimation of 95% Confidence Interval Sample Correlation

The inherently random process of the annual precipitation extremes coupled with the severe scarcity of data makes it highly spatio–temporally uncertain for hydrometeorologic regions (Dingman 2015). Hence, it is necessary to incorporate the uncertainty estimation. As mentioned in Section VI.2.3, the sampling distribution for each weather station was determined using the equation defined in Fisher (1915), and the sample correlation at 95% confidence interval was estimated. Figures 11–13 illustrate the sample correlation distribution for the Texas climate regions and Figure 14 shows the band between the calculated correlation at the selected stations and the estimated sample correlation at 95% confidence interval. It can observed that sample correlation coefficients were highly significant (i.e., $|Sample\,Correlation| \geq 0.6$) in determining the relationship of climatic cycles and annual precipitation extremes.

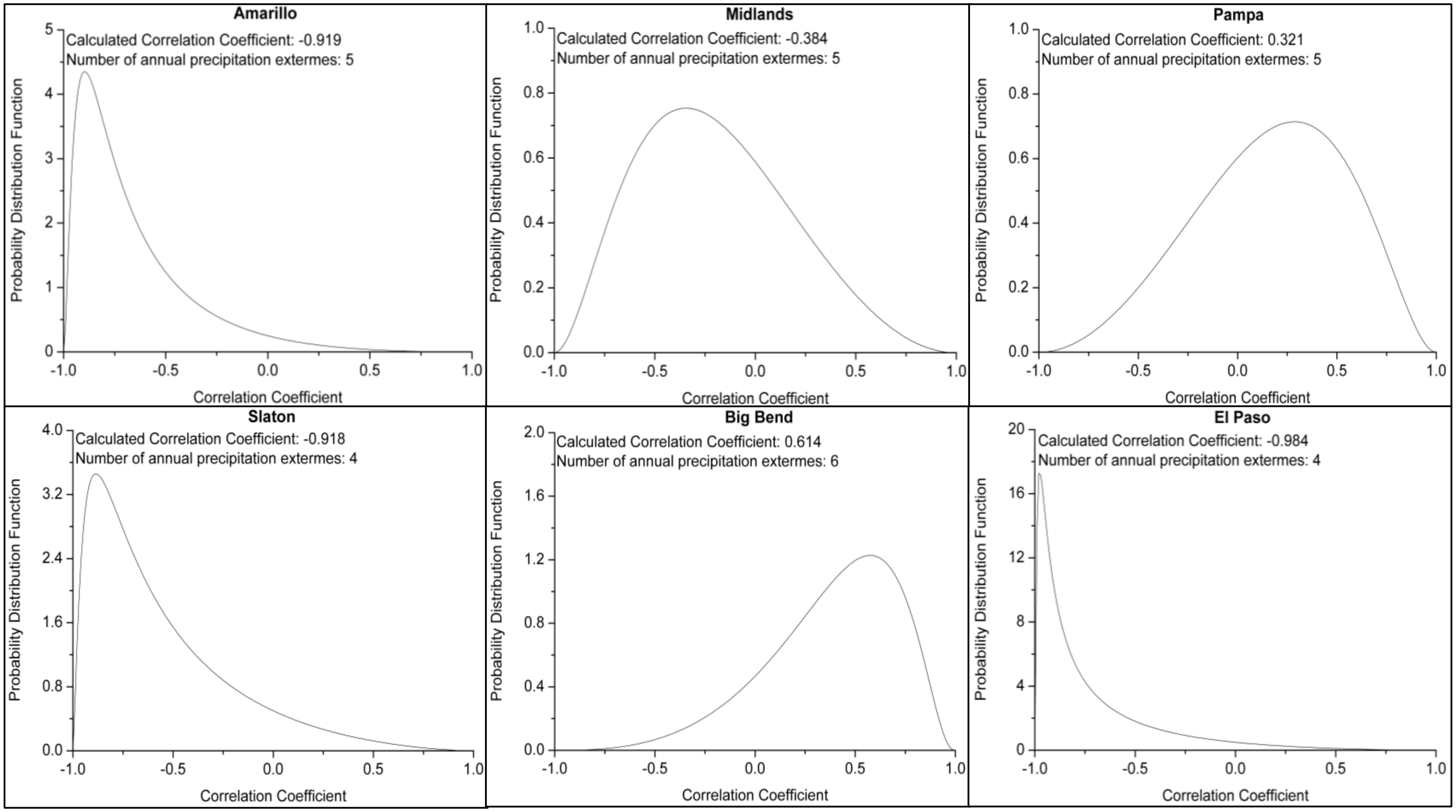

Figure 11: Sampling distribution for the robust correlation coefficient with the North Atlantic Oscillation (NAO) for the Cold Desert/Semi–Arid climate region of Texas

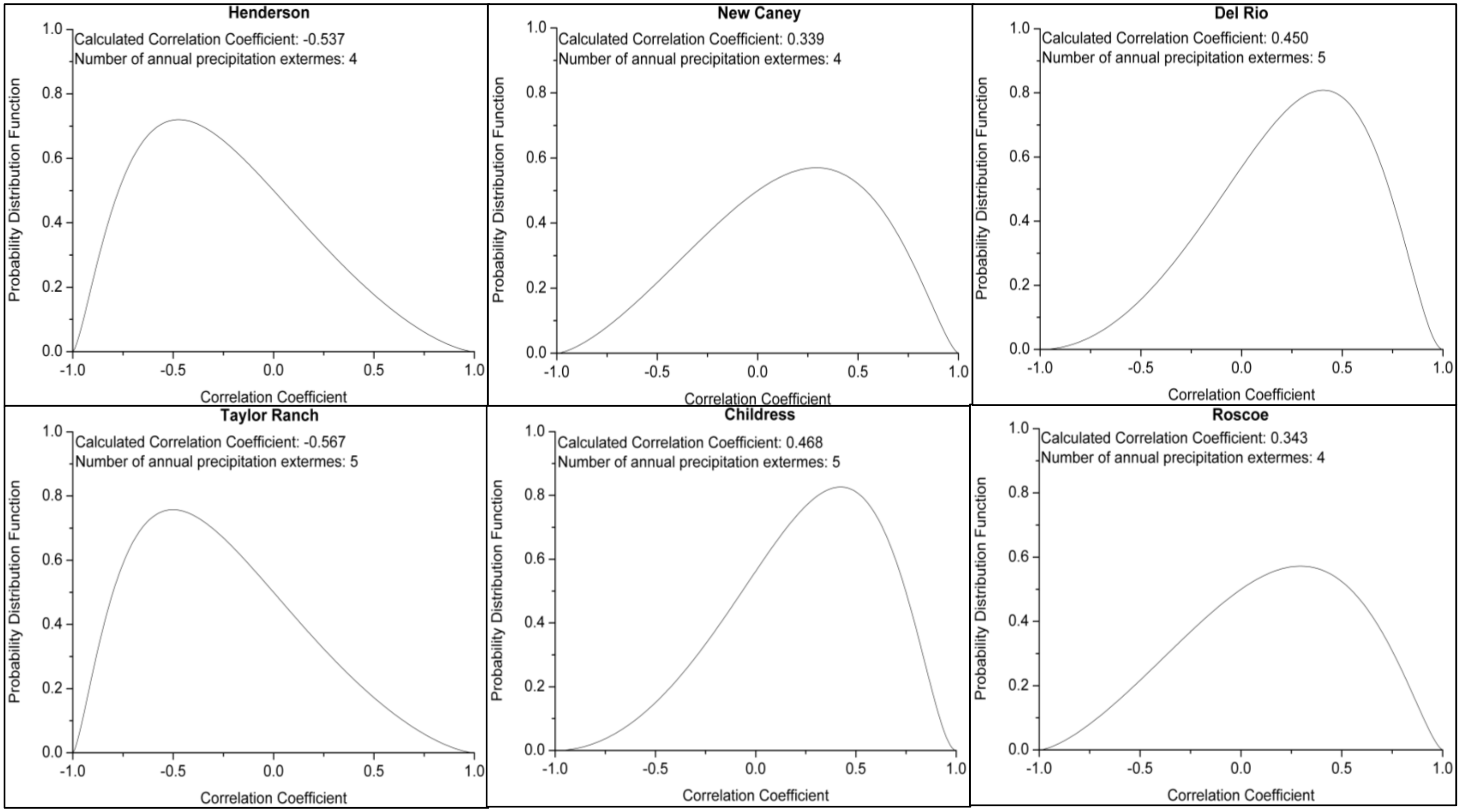

Figure 12: Sampling distribution for the robust correlation coefficient with the Atlantic Multidecadal Oscillation (AMO) for the Humid Sub–Tropical climate region of Texas

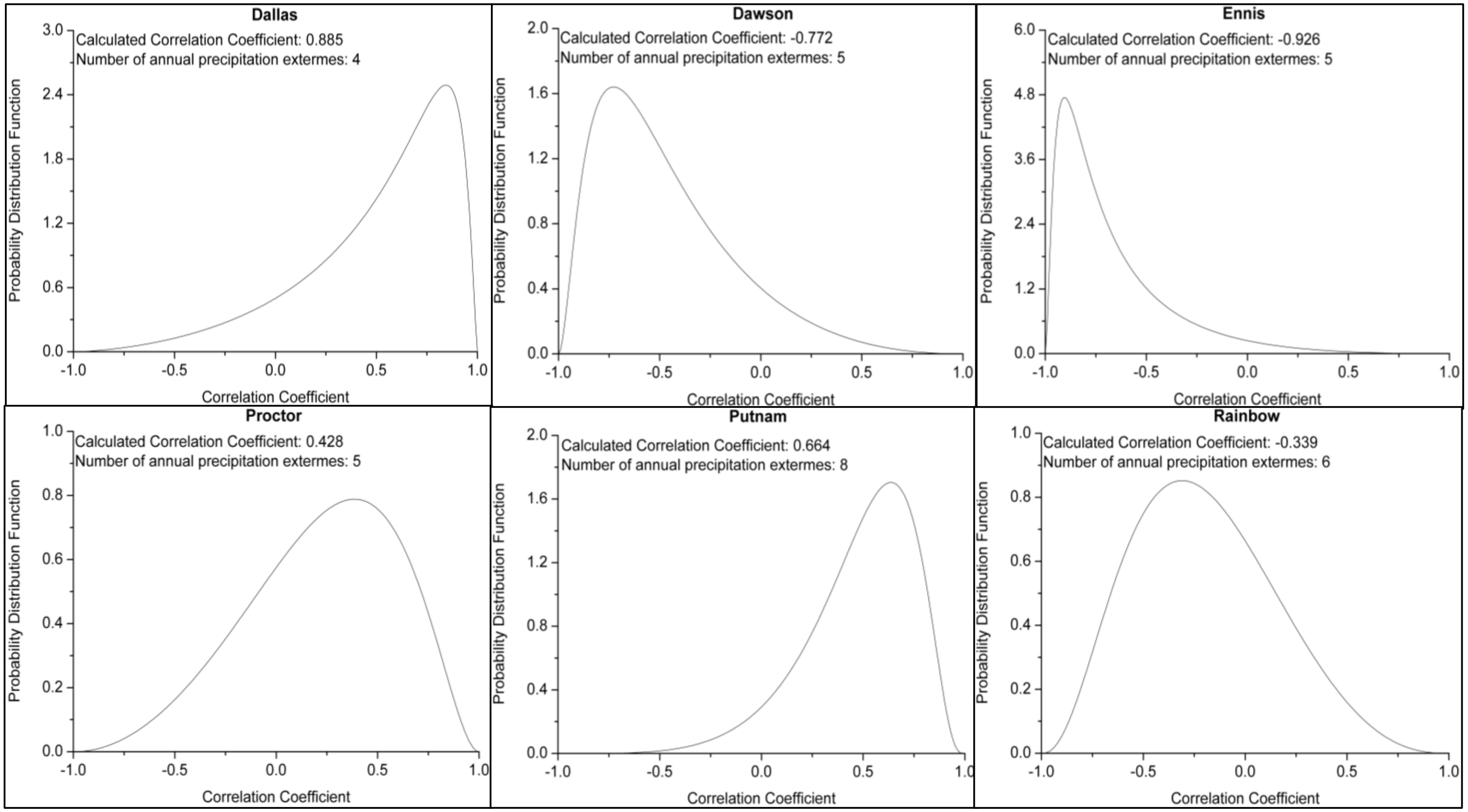

Figure 12 Continued.

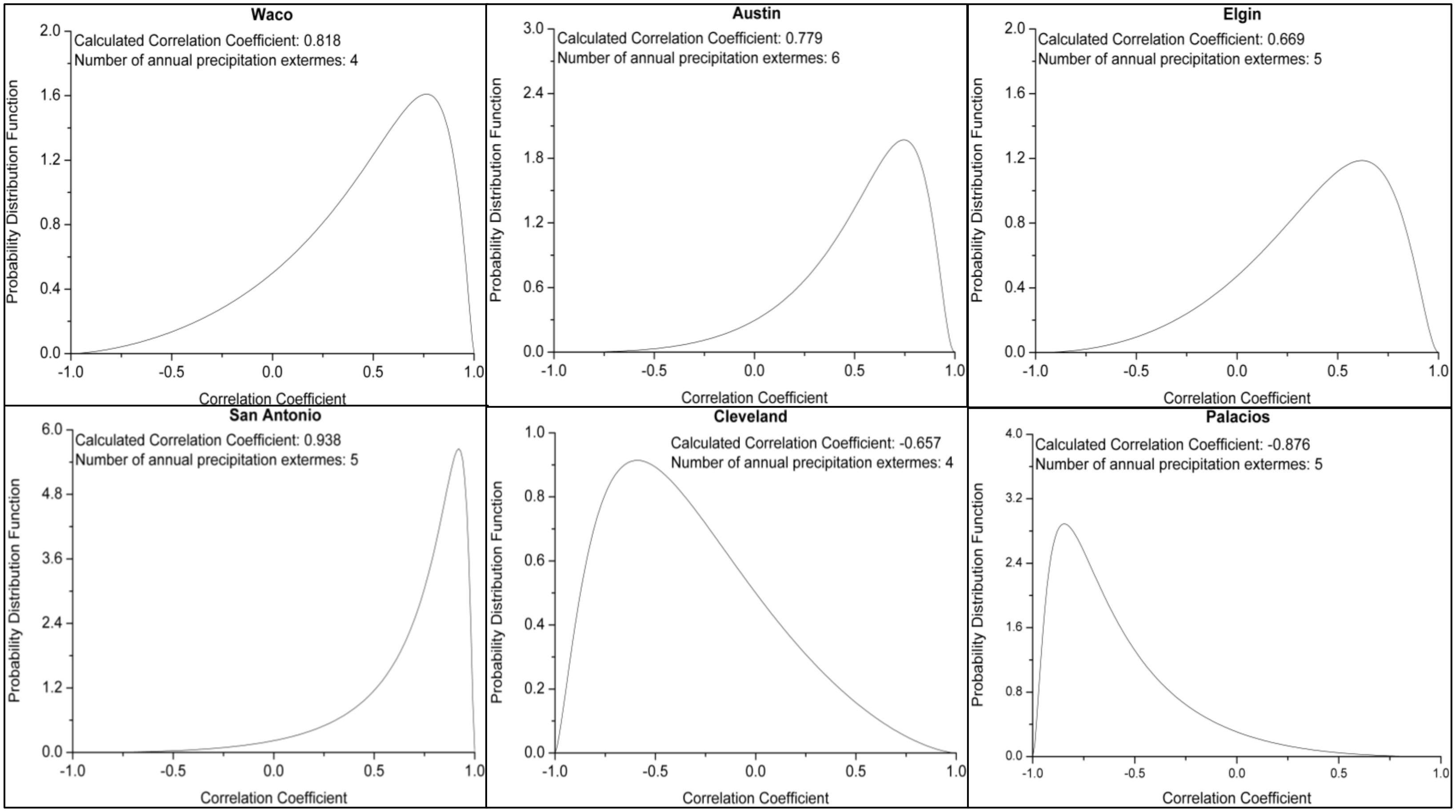

Figure 12 Continued.

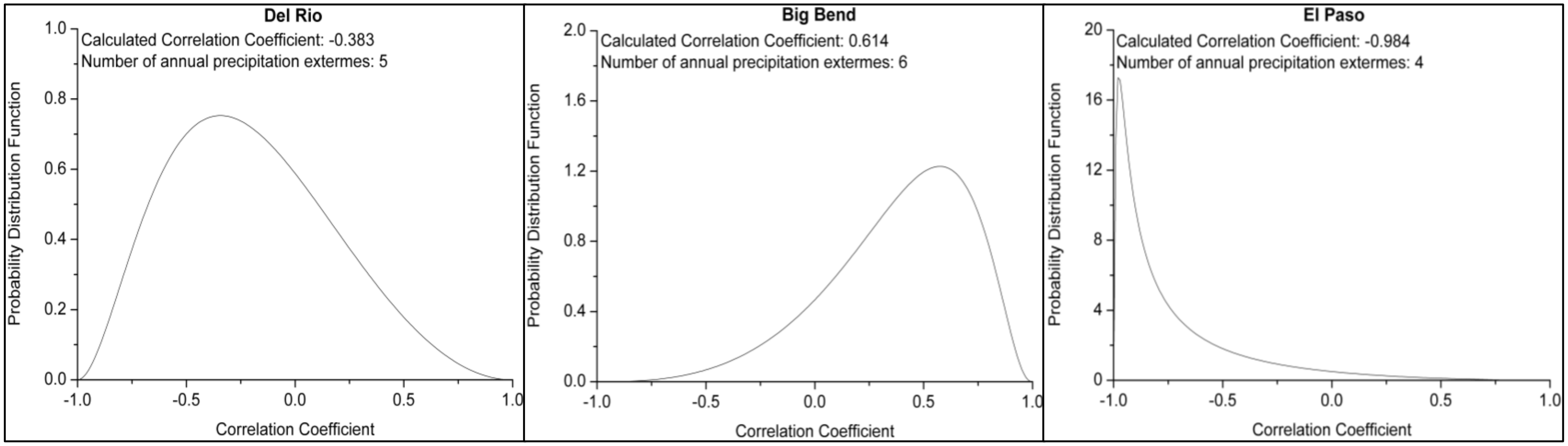

Figure 13: Sampling distribution for the robust correlation coefficient with the North Atlantic Oscillation (NAO) for the Warm Desert/Semi–Arid climate region of Texas

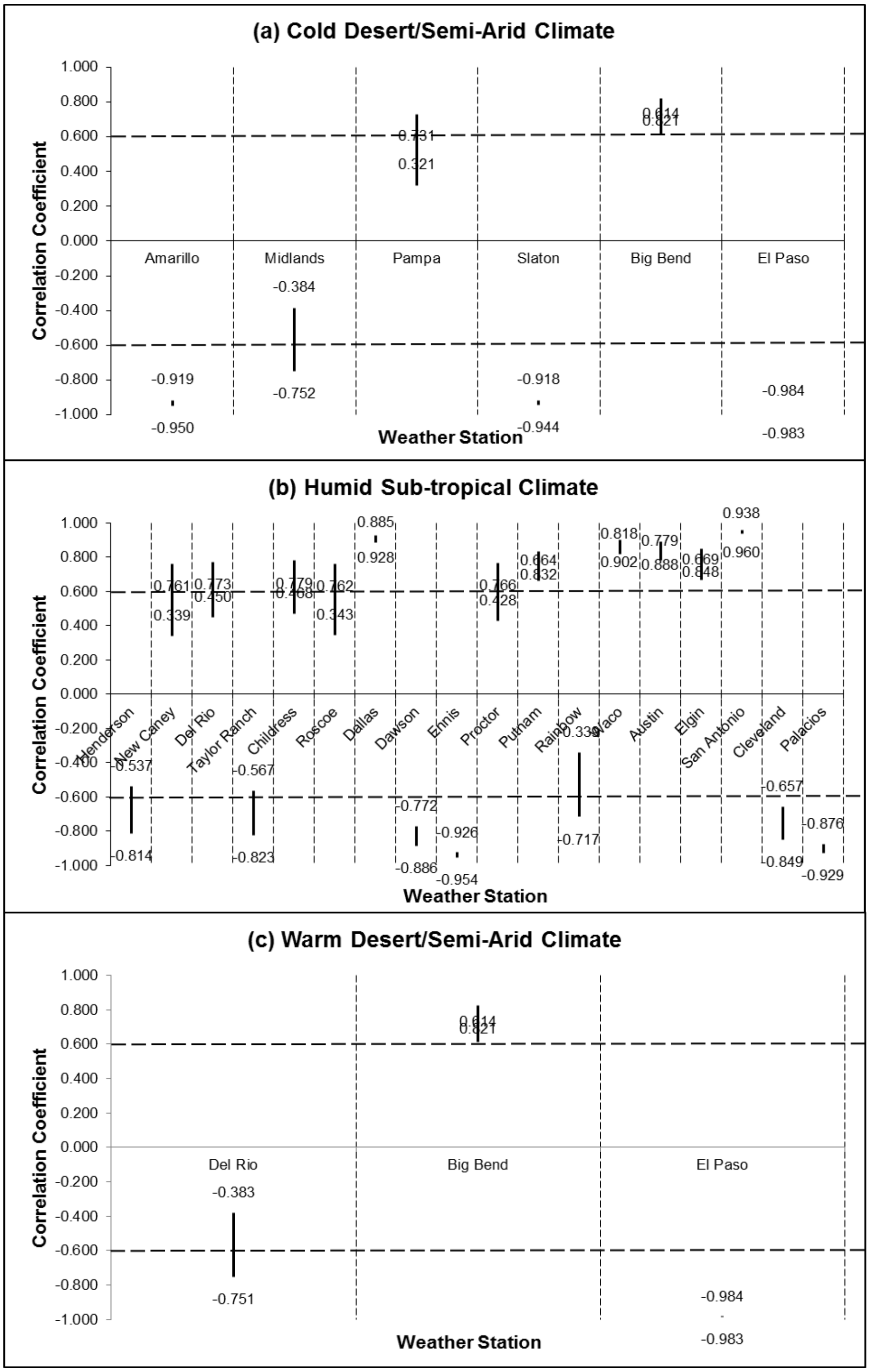

Figure 14: Uncertainty band of the calculated correlation coefficient and sample correlation at the 95% confidence interval

VII.2.4 Variation of Correlation Coefficients with Topographic and Climatic Attributes

The Inverse Distance Weighted (IDW) interpolation method was employed to generate the graduated color plots for displaying the variation of correlation coefficients across the state of Texas for different climate regions: (i) Cold Desert/Semi–Arid Climate (Figure 15), (ii) Humid Sub–Tropical Climate (Figure 16), and (iii) Warm Desert/Semi–Arid Climate (Figure 17). The method resonated with Tobler's Law of Geography (Tobler 1970), as the interpolated coefficients were found to be similar to the calculated correlation coefficients in the vicinity, as shown in the respective figures.

Texas offers a wide variety of geography, extending from the mountainous peaks in western Texas to piney woods, swamps, and gulf coast in eastern Texas, and from farmland in north central Texas to plain ranches in southern Texas. Such elevation differences directly contribute to the regional precipitation variability (Haiden and Pistotnik 2009). Heavy precipitation events are also driven by the atmospheric variations due to higher temperatures (Berg et al. 2013). The increased capability of atmosphere to hold the water vapor amplifies the probability of higher regional precipitation. Global climate change, variations in climatic cycles, and modest changes in winds have intensified the precipitation regimes in spatio–temporally variable wetter hydrologic regions (Trenberth 2011, Fan et al. 2013). Therefore, regional total precipitation also acts as an attribute for the heavy precipitation events. Here, the trend of calculated correlation coefficients of annual precipitation extremes and Atlantic and Pacific Ocean based Climatic Cycles is further studied with key precipitation attributes: (i) elevation (m) , (ii) average temperature (ºF), and (ii) average precipitation (in.) at the weather stations. The climatic factors of average temperature and precipitation were incorporated in two ways: monthly averages and anomaly of monthly and annual averages in the month of extremes.

VII.2.4.1 *Weather Station Elevation*

Figure 15a, 16a, and 17a illustrate the variation of relationship of annual precipitation extremes ($P_{extreme}$) with climatic cycles, with changing elevation of the weather stations in the Cold Desert/Semi–Arid, Humid Sub–Tropical, and Warm Desert/Semi–Arid climate regions of Texas, respectively. For the Cold Desert/Semi–Arid Climate Region, weather stations in the same range of elevation resulted in an incoherent correlation relationship. For example, in the High Plains climate division, the correlation coefficient for Pampa and Slaton was determined to be 0.321 and –0.918, respectively, in spite of the differences in station elevation by mere 21 m. For the Warm Desert/Semi–Arid Climate regions, the similar relationship in Trans Pecos climate division was followed up. Therefore, no significant impact of the weather station elevation was observed for the calculated correlation coefficients for both Cold and Warm Desert/Semi–Arid Climate regions of Texas. In the Humid Sub–Tropical Climate region, which mainly comprises the area of plains, farmlands, swamps, and coasts, the same relationship is vaguely governed by the weather station elevation. As illustrated in Figure 16a, weather stations with higher elevation (i.e., climate divisions of Low Rolling Plains, Edwards Plateau, and eastern end of North Central ranging within the elevation between 350 m and 750 m) are likely to receive the regional maximum daily precipitation within a year in the warm phase of AMO. The respective weather stations, such as Del Rio, Childress, Roscoe, Proctor, and Putnam, observed 18 10–years or greater recurrence $P_{extreme}$ events with an average of 6.113 in. in the warm phase of AMO in comparison to 9 10–years or greater recurrence $P_{extreme}$ events with an average 5.613 in. in the cold phase of AMO. However, the respective correlation coefficients were considerably weaker, i.e., with an average of 0.471 and standard deviation of 0.118.

VII.2.4.2 *Average Temperature at the Weather Station*

The influence of climatic attributes on the relationship of climatic cycles and extreme precipitation was incorporated in two ways: (i) averages in the month of extremes, and (ii) anomaly of extremes' month averages with annual averages. For the Cold Desert/Semi–Arid Climate region, as shown in Figure 15b, weather stations with higher average temperature in the month of extremes (70ºF–80ºF), such as Amarillo, Midlands, and El Paso, are expected to receive highly intensified $P_{extreme}$ in the cold phase of NAO. The weather stations observed 7 10–years or greater recurrence $P_{extreme}$ events in both warm and cold phases of NAO; however, the average precipitation exceeded in latter by 1 in. Further, weather stations with lower average temperature (<70ºF) in the month of extremes, such as Big Bend and Pampa, resulted in comparatively weaker positive relationships between NAO and annual precipitation extremes (average correlation coefficient $\approx$ 0.468). The average temperatures of weather stations in the Humid Sub–Tropical Climate region in the month of extreme precipitation lie in the range from 62ºF to 82ºF, and the heavy precipitation events are likely to occur in the warm phase of AMO in Central Texas with higher average temperatures (>72*ºF*), as shown in Figure 16b. These potential links are illustrated by weather stations, such as

Childress, Roscoe, Del Rio, Elgin, Austin, Proctor, and Putnam, which observed 23 10–years or greater recurrence $P_{extreme}$ events with an average of 6.226 in. in the warm phase of AMO in comparison to 15 10–years or greater recurrence $P_{extreme}$ events with an average of 5.771 in. in the cold phase of AMO. Further, for the Warm Desert/Semi–Arid Climate region, no significant impact of the average temperature of stations on the calculated correlation coefficient was observed, as shown in Figure 17b.

The temperature anomalies, i.e., the difference in the average temperature in the month of extremes and annual averages, resulted in rather contrasting observations. For the Cold Desert/Semi–Arid Climate region, in spite of the significant relationship between average temperature in the month of extremes and the calculated correlation coefficients, the similar temperature anomalies of the respective weather stations, for example, El Paso and Pampa ($\approx$13ºF), and Midlands and Slaton ($\approx$7–10ºF) showed differing relationships between NAO and extreme precipitation, as shown in Figure 15d. This signifies that the link of climatic cycles and extreme precipitation for the region is considerably independent of the temperature anomalies. The same independence between the attributes is also observed for the Humid Sub–Tropical Climate region, as weather stations with lower temperature anomalies (<1ºF), such as Dallas, Dawson, Waco, and Cleveland, or with higher temperature anomalies (>12ºF) resulted in significantly different relationships between climatic cycles and annual precipitation extremes, as shown in Figure 16d. And the Warm Desert/Semi–Arid climate region is more likely to receive annual precipitation extremes in the cold phase of NAO where higher historical temperature anomaly (>12ºF) is observed and in the warm phase of NAO where lower historical temperature anomaly (<1ºF) is observed (Figure 17d).

VII.2.4.3 *Average Total Precipitation at the Weather Stations*

Figures 15c, 16c, and 17c illustrate the variation of calculated correlation coefficients (between climatic cycles and extreme precipitation) with changing average total precipitation in the month of extremes at the weather stations in the Cold Desert/Semi–Arid Climate, Humid Sub–Tropical Climate, and Warm Desert/Semi–Arid Climate regions of Texas, respectively. For both the Cold and Warm Desert/Semi–Arid climate regions, the calculated correlation coefficients between NAO and annual precipitation extremes are not found to be influenced by the changing average total precipitation at the weather stations, as shown by the case of Amarillo and Pampa (with correlation coefficients of –0.919 and 0.321 respectively, when the average total precipitation ranged between 2.5–2.7 in.) for the former and Big Bend and El Paso (with correlation coefficients of 0.614 and –0.984, respectively, when the average total precipitation ranged between 1.3–1.7 in.) for the latter. However, for the Humid Sub–Tropical Climate region, stations with higher average total precipitation (≥ 4 in.), at the eastern end, are more likely to observe extreme precipitation in the cold phase of AMO, whereas stations in central Texas with lower average total precipitation (≤ 3 in.) show the strong likelihood of extreme precipitation in the warm phase of AMO. For example, Cleveland, Ennis, and Palacios along the Gulf Coast observed 10 10–years or greater recurrence $P_{extreme}$ events in the cold phase of AMO with an average of 9.156 in. in comparison to 4 10–years or greater recurrence $P_{extreme}$ events with an average of 7.670

in. in the warm phase of AMO. Further, weather stations in North Central climate division, such as Dallas, Putnam, and Waco, received 10 10–years or greater recurrence $P_{extreme}$ events in the warm phase of AMO with an average of 5.476 in. in comparison to 6 10–years or greater recurrence $P_{extreme}$ events with an average of 4.467 in. in the cold phase of AMO.

Even though the correlation coefficients in the Cold and Warm Desert/Semi–Arid Climate regions of Texas were not influenced by average total precipitation at the weather stations, contrastingly both the regions showed considerably stronger link with the total precipitation anomalies. In both climate regions, the weather stations with greater positive total precipitation anomaly (>0.7 in.) tend to attain a higher (lower) chance of receiving intensified extreme precipitation in the cold (warm) phase of NAO. It is illustrated in the case of Amarillo and El Paso in the Cold Desert/Semi–Arid Climate region (Figure 15e), and in Del Rio and El Paso in the Warm Desert/Semi–Arid Climate region (Figure 17e) for which the average of 10–years or greater recurrence $P_{extreme}$ events in the cold phase of NAO exceeded by 1.223 and 0.480 in. respectively. Further for the Humid Sub–Tropical Climate region, total precipitation anomalies showed a similar but slightly weaker impact than the total precipitation on the calculated correlation coefficients, i.e., greater is the positive (negative) precipitation anomaly, more is the chance of receiving extreme precipitation in the cold (warm) phase of AMO. This impact of precipitation anomalies can be observed in the case of Dawson, Ennis, Cleveland, and Palacios which collectively observed 13 10–year or greater recurrence $P_{extreme}$ events in the cold phase of AMO with an average of 8.756 in. in comparison to 6

10–year or greater recurrence $P_{extreme}$ events with an average of 7.270 in. in the warm phase of AMO, as shown in Figure 16e.

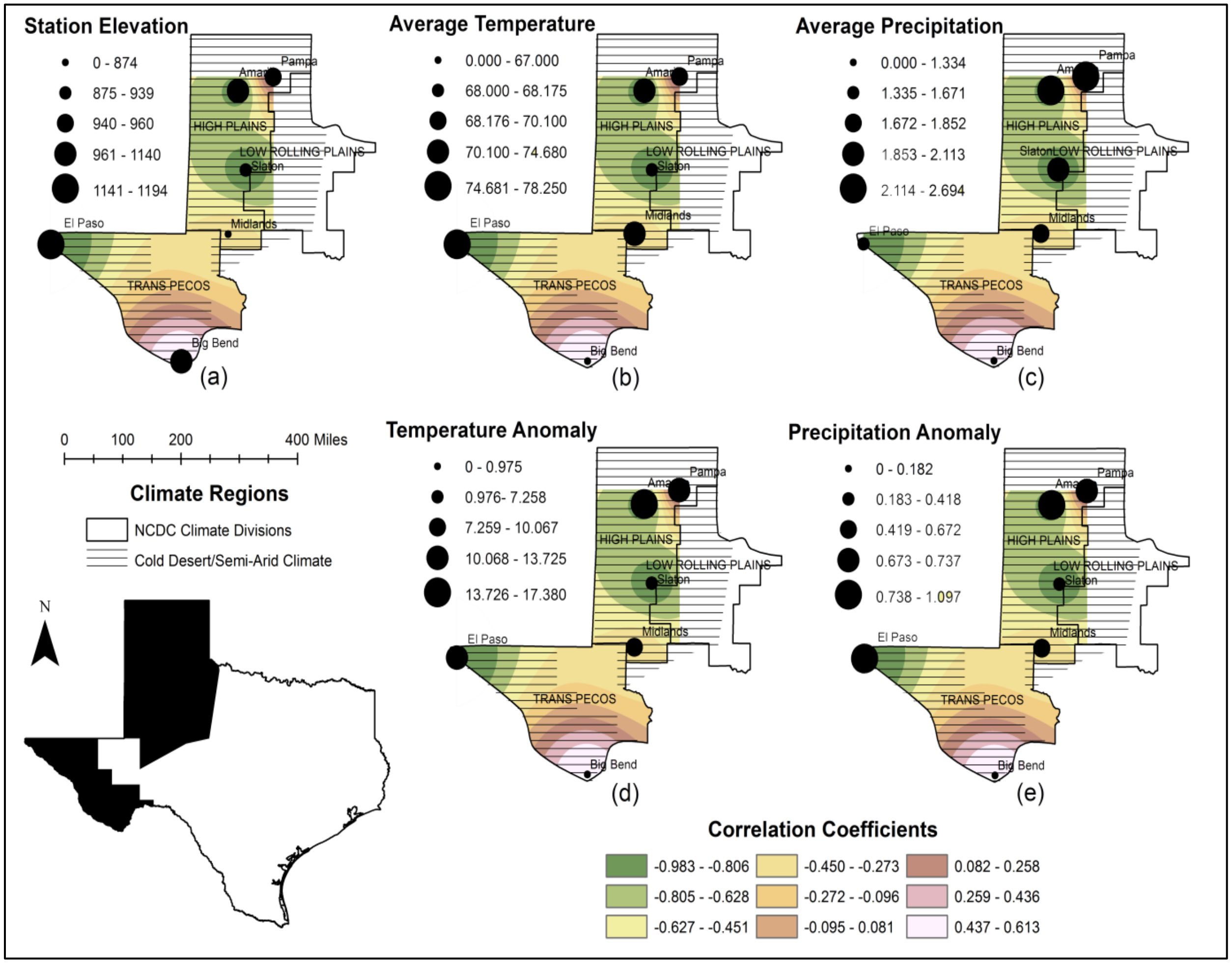

Figure 15: Variation of correlation coefficients in Cold Desert/Semi–Arid climate region of Texas and its relationship with topographic and climatic attributes

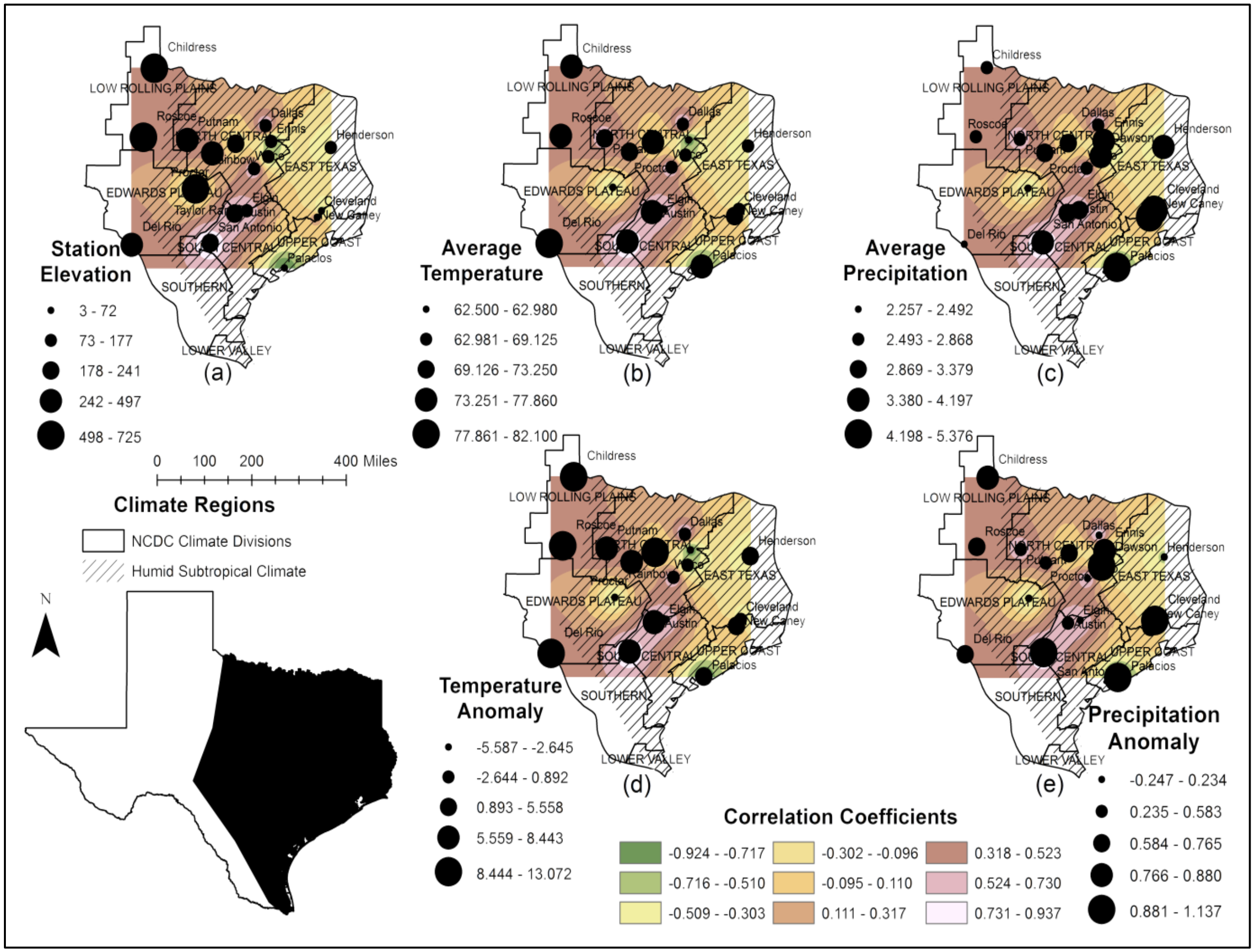

Figure 16: Variation of correlation coefficients in Humid Sub–Tropical climate region of Texas and its relationship with topographic and climatic attributes

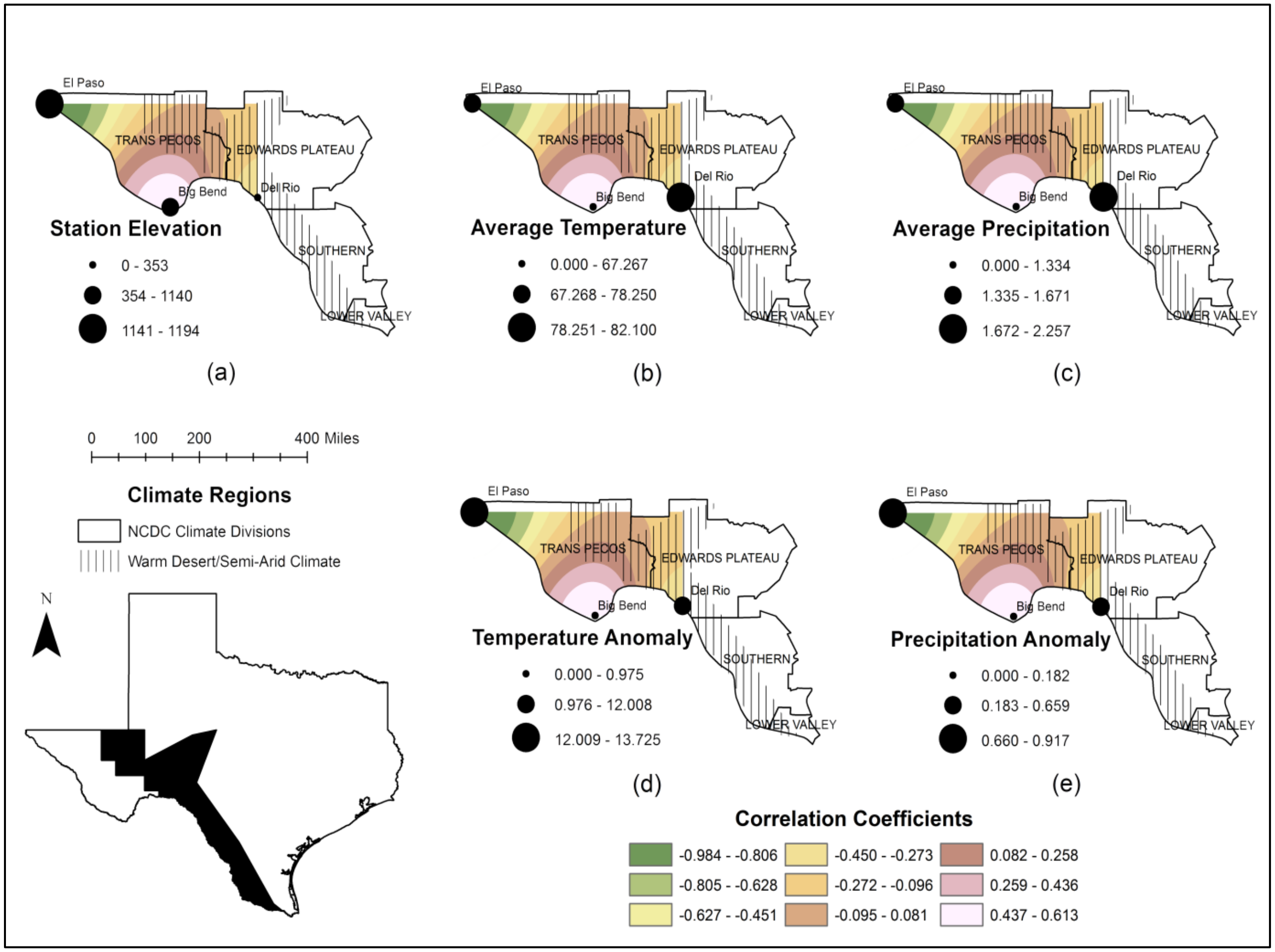

Figure 17: Variation of correlation coefficients in Warm Desert/Semi–Arid climate region of Texas and its relationship with topographic and climatic attributes

VII.3 Research Objective III

VII.3.1 Variation in Sensitivity Indices

For Research Objective II it was determined that the 10–year or greater recurrence interval annual precipitation extremes ($P_{extreme}$) were significantly influenced by the variations in North Atlantic Oscillation (NAO) and Atlantic Multidecadal Oscillation (AMO) for Cold and Warm Desert/Semi–Arid Climate region, and Humid Sub–Tropical Climate region of Texas, respectively. Figure 18 shows the sensitivity indices calculated for respective $P_{extreme}$ events with variations in most correlated climatic cycles, and Figure 19 shows the max–min–average plots of 95% confidence bounds in the corresponding lower–end limits, calculated values, and higher–end limits of sensitivity indices in integrated and differentiated analysis for different climate regions. The absolute value of sensitivity indices less than or equal to 0.1 was considered to be a weak to no–influence of the climatic cycle on $P_{extreme}$ events. It is observed from Figure 19 that there are significant differences in the sensitivity indices determined using the integrated analysis and the proposed differentiated analysis.

For Cold Desert/Semi–Arid Climate region, the $P_{extreme}$ events at only Slaton weather station were found to be fairly influenced by the variation in NAO, as per the integrated sensitivity analysis, as shown in Figure 18. The respective index for integrated analysis was determined to be –0.126, whereas the impact was clearly intensified with the variation in warm phase of NAO with an index value of –0.308. Overall, $P_{extreme}$ events at the majority of stations in the climate region were not found to be sensitive to the variation in NAO as shown by the indices ranging between –0.126 and 0.029 with an average of –0.039. The indices increased in the case of differentiated sensitivity analysis: ranging between –0.220 and 0.186 for the cold phase of NAO and between –0.308 and 0.156 for the warm phase of NAO, but the corresponding considerable increments in uncertainty were also observed with respective lower bounds going up to –0.506 and –0.609 and upper bounds up to 0.519 and 0.373, as shown in Figure 19. A similar relationship was also observed in the case of Warm Desert/Semi–Arid Climate region, where only Taylor Ranch weather station showed considerably acceptable links in differentiated sensitivity analysis with an index value of 0.156 in the cold phase of NAO and –0.130 in the warm phase of NAO, as illustrated in Figure 18. Similar to the Cold Desert/Semi–Arid Climate region, here the regional $P_{extreme}$ events were also not found to be sensitive to the variation in NAO, as shown in Figure 19, with indices ranging between –0.085 and 0.018, –0.220 and 0.156, and –0.130 and 0.014 for integrated sensitivity analysis, and cold and warm phase differentiated sensitivity analysis, respectively. The uncertainty from lower to higher bound for latter also increased from –0.224 to 0.109 in integrated analysis, to lower bounds going up to –0.506 and –0.615 and upper bounds up to 0.489 and 0.369 in cold and warm phase differentiated analysis, respectively. Due to these insignificant and highly uncertain values of sensitivity indices, further analyses were not done for both the Cold and Warm Desert/Semi–Arid Climate regions.

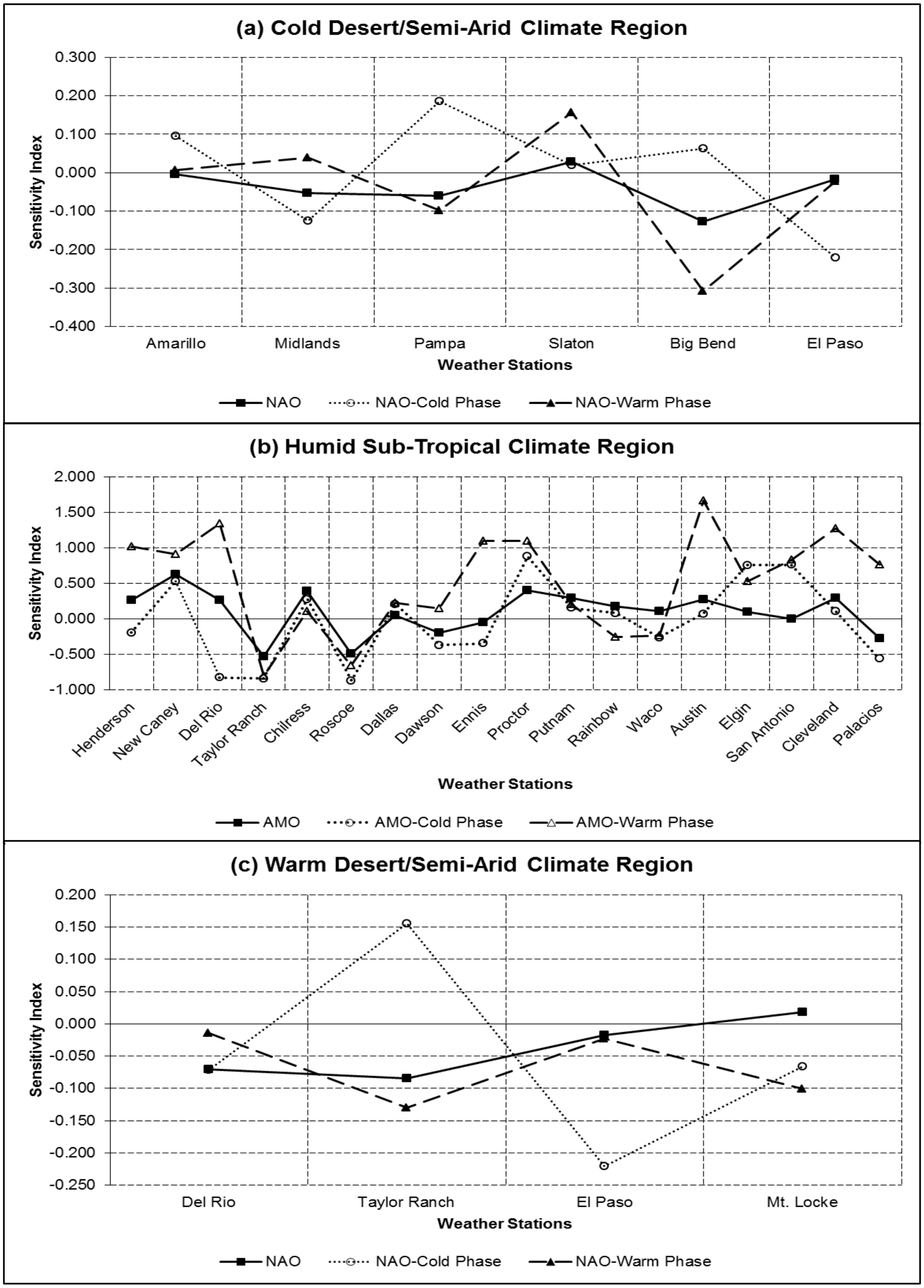

Figure 18: Sensitivity indices for Texas climate regions

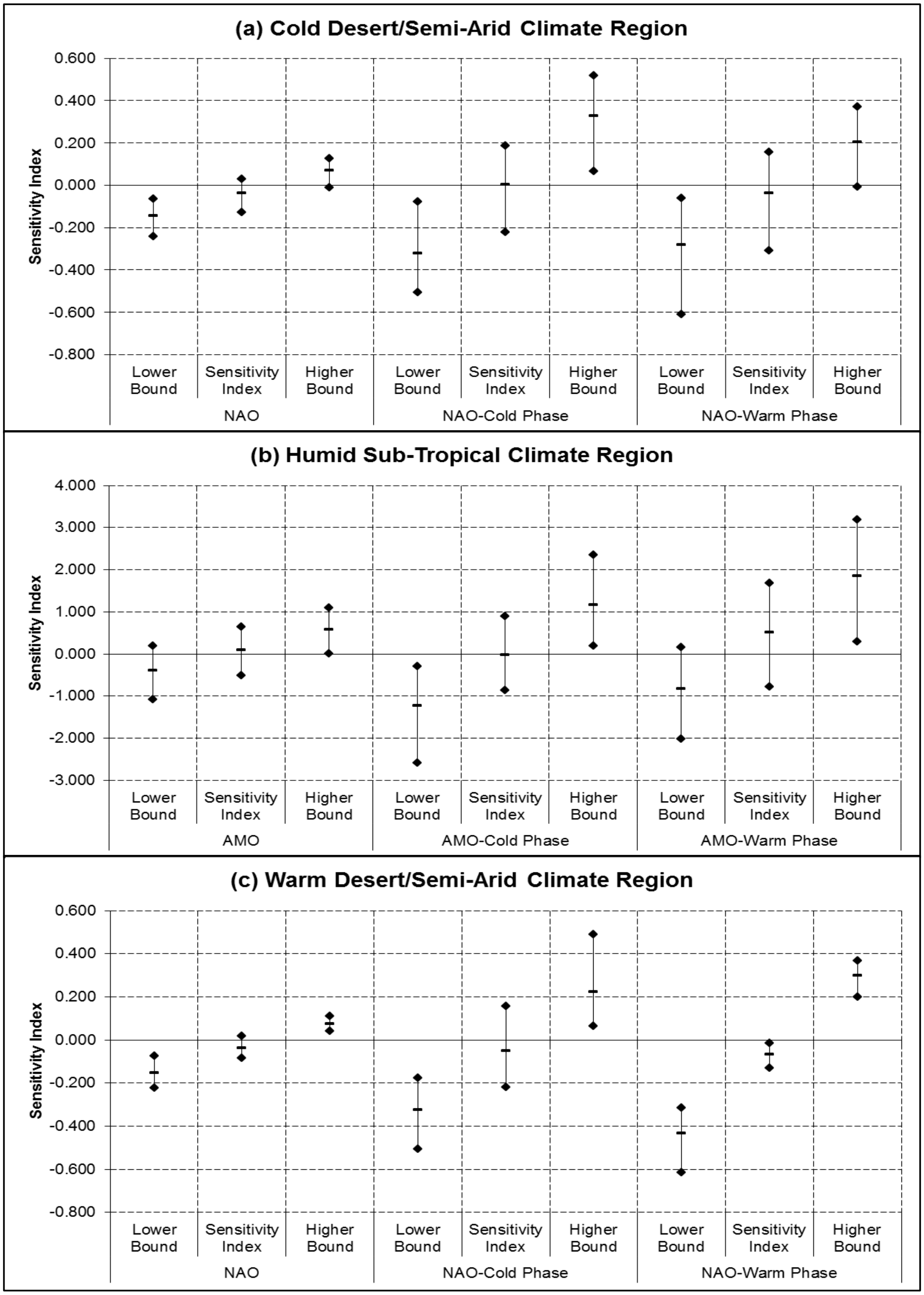

Figure 19: Uncertainty in differentiated sensitivity analysis

On the contrary, weather stations in the Humid Sub–Tropical Climate region were found to be highly sensitive to the variations in AMO. The sensitivity indices ranged between 0.526 and 0.627 in the integrated analysis, which were further intensified in the cold phase differentiated analysis (between –0.868 and 0.876) and the warm phase differentiated analysis (–0.800 and 1.661), as shown in Figure 19. The climate region mainly receives extreme precipitation events with the effect of tropical cyclone activities (Zhu et al. 2013), which are found to be significantly influenced with changes in the state of AMO (Nogueira and Keim 2010). The geographical features of Balcones Escarpment (Nielsen et al. 2016), Gulf of Mexico (Kimmel Jr et al. 2016), and increasing rate of urbanization (Zhao et al. 2016, Gunn 2016) make the climate region prone to devastating floods after heavy precipitation events. Further analyses of variation of sensitivity indices and degree of projected $P_{extreme}$ events for the Humid Sub–Tropical Climate region were done in the following sections.

VII.3.2 Variation of Sensitivity Indices with Changing Hydrometeorological Attributes

The annual precipitation extremes for a region vary with changing local hydrometeorological attributes, as described in Section VII.2.4. Therefore, we studied the variation in sensitivity indices for Humid Sub–Tropical Climate region determined in Section VII.3.1 (for both warm and cold phases of AMO), with changing hydrometeorological attributes of 18 regional weather stations: (i) elevation, (ii) average precipitation, and (iii) average temperature. The latter two were incorporated as both averages in the month of extremes and anomalies computed as the difference in averages in the month of extremes and in the year, as elucidated in Section VII.2.4.2 and VII.2.4.3.

Figure 20 illustrates the calculated sensitivity indices in the cold phase differentiated sensitivity analysis. Here the indices were not found to be affected by the variations in the above mentioned hydrometeorological attributes. For example, Chilress and Taylor Ranch have a mere elevation difference of 36.9 m, but the $P_{extreme}$ events sensitivity to the changes in the state of AMO were found to be 0.393 and –0.526 respectively, as shown in Figure 20a. Further, in the case of Proctor and Putnam, the average temperature ranged between 72–73ºF and average temperature anomaly between 7–8ºF, as shown in Figure 20b and 20d, respectively, however, the corresponding cold phase calculated sensitivity was determined to be 0.876 and 0.157. The similar weaker links were also observed for average precipitation and precipitation anomaly, as shown in Figure 20c and 20e, respectively, where stations such as Roscoe and Dallas with average precipitation between 2.5–2.6 in. and San Antonio and Cleveland with precipitation anomaly between 0.9–1.0 in. showed significantly dissimilar sensitivity indices.

The variation of calculated sensitivity indices in the case of $P_{extreme}$ events and warm phase of AMO (differentiated analysis) is shown in Figure 21. It is observed from Figure 21a that the increase in $P_{extreme}$ events at weather stations with lower ground elevation, such as Henderson, Cleveland, New Caney, and Palacios, was highly sensitive to the increment in the AMO state, with indices values ranging from 0.768 to 1.274; whereas in the case of weather stations with higher ground elevation, such as Roscoe and

Taylor Ranch, a projected increase in $P_{extreme}$ events was expected with a decrement in the AMO state. The indices for the region were not found to be significantly impacted by the variation in average temperature and temperature anomalies at the weather stations, as shown in Figure 21b and 21d, respectively. Stations, such as Chilress and Roscoe, with average temperature ranging between 74–76ºF and temperature anomaly between 0.7–0.9ºF possessed different links between $P_{extreme}$ events and warm states of AMO with corresponding indices of 0.104 and –0.652. Figure 21c illustrates that weather stations with higher average precipitation (>4 in.), such as Henderson, New Caney, Cleveland, and Palacios, tended to experience a rise in $P_{extreme}$ events in warmer states of AMO with indices exceeding 0.7, however, a similar relationship could not be established between $P_{extreme}$ events and precipitation anomalies, as shown in Figure 21e.

VII.3.3 Analysis of Projected Annual Precipitation Extremes

The Wakeby, Burr XII, and Inverse Gaussian distributions were found to be the top–three ranked probability distributions for describing the variation of $P_{extreme}$ events for Humid Sub–Tropical Climate region. The Wakeby distribution was rejected as per the Anderson–Darling test statistic for Henderson, Proctor, Rainbow, Waco, and Cleveland weather stations. Therefore, in this study, the Burr XII Distribution was selected for describing the empirical probability of occurrence of historical and projected $P_{extreme}$ events. The value of theoretical constant 'α' for the Burr XII distribution is 0.4 (Cunnane 1978).

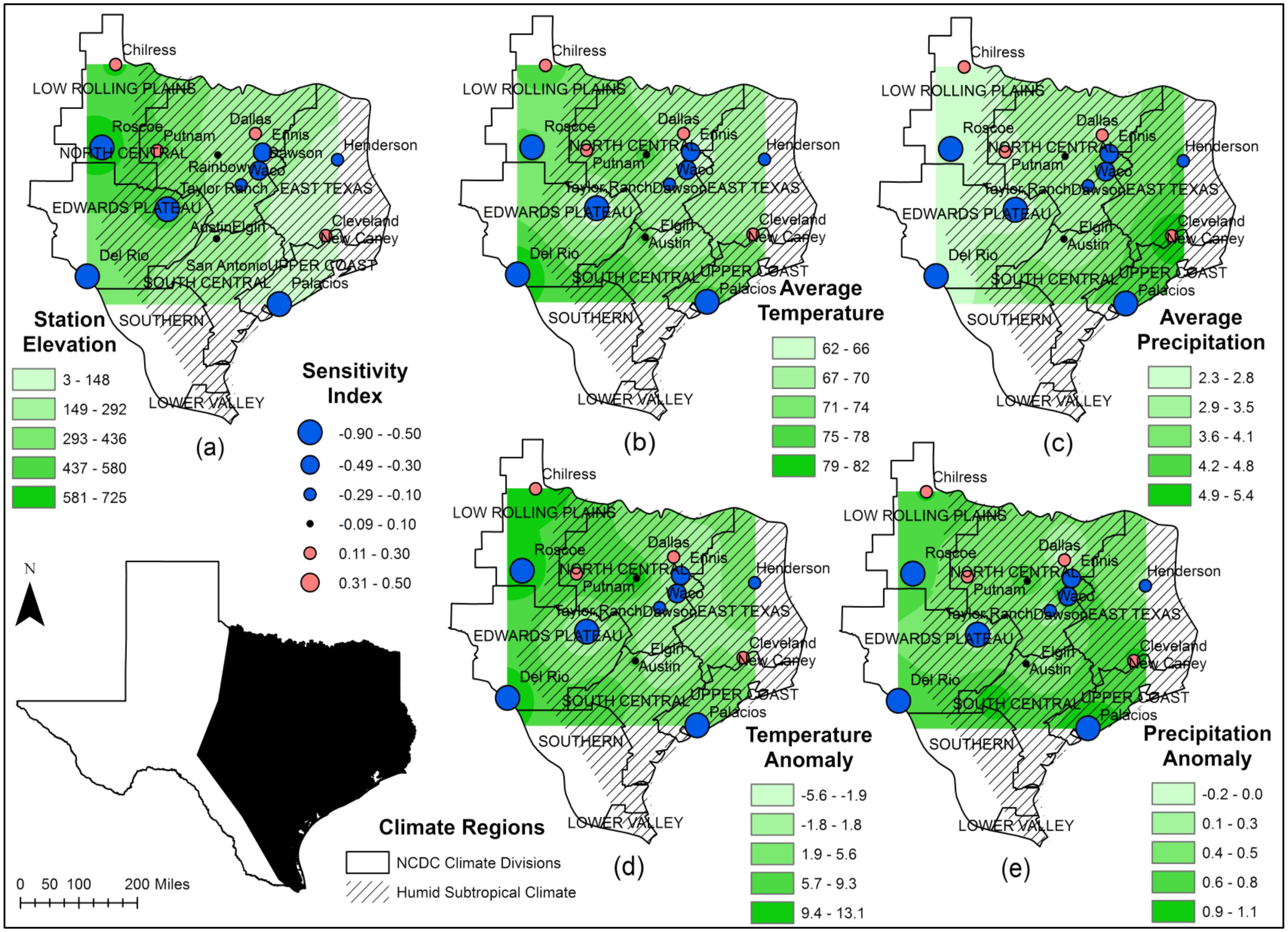

Figure 20: Variation of sensitivity indices in Humid Sub–Tropical climate region in cold phase of AMO

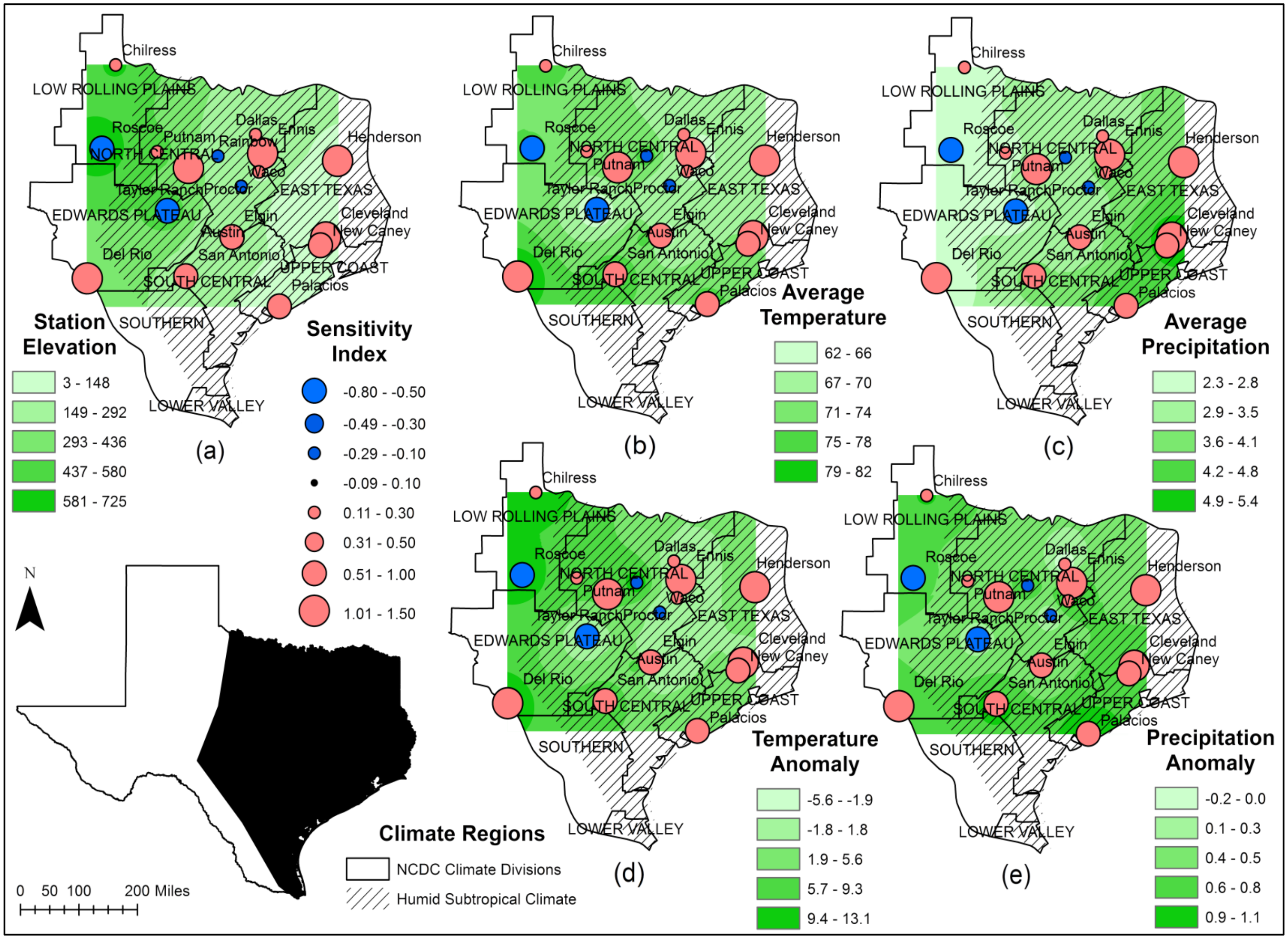

Figure 21: Variation of sensitivity indices in humid sub–tropical climate region in warm phase of AMO

The probability density function (PDF) and cumulative distribution function (CDF) of Burr XII distribution are shown Equations 14 and 15 respectively. Equations 16 and 17 derive the theoretical linear relationship between logarithmic transformations of the CDF.

$$f(x) = \frac{\alpha k \left(\frac{x}{b}\right)^{a-1}}{b\left(1+\left(\frac{x}{b}\right)^{a}\right)^{k+1}} \tag{14}$$

$$F(x) = 1-\left(1+\left(\frac{x}{b}\right)^{a}\right)^{-k} \tag{15}$$

where *k* and *a* are the continuous shape parameter (*k* > 0; *a* > 0), and *b* is the continuous scale parameter (*b* > 0). Rearranging equation 15 and taking logarithms on both sides, we get a linear relationship between $g(x,k,a,b) \equiv k\log\left(1+\left(\frac{x}{b}\right)^{a}\right)$ and $f(F(x)) \equiv \log\left(\frac{1}{1-F(x)}\right)$,

$$\left(1+\left(\frac{x}{b}\right)^{a}\right)^{-k} = 1-F(x) \tag{16}$$

$$\log\left(\frac{1}{1-F(x)}\right) = k\log\left(1+\left(\frac{x}{b}\right)^{a}\right) \tag{17}$$

The goodness of fit of the Burr XII distribution for $P_{extreme}$ events at 18 weather stations of Humid Sub–Tropical Climate region is illustrated in Figure 22. The respective trendlines agree well with the aforementioned theoretical linear relationship of the distribution in equation 17. Between 1966 and 2014, the highest recorded historical increase (decrease) in AMO state for consecutive months was found to be 0.238 (–0.228). For a weather station in the Humid Sub–Tropical Climate region with positive (negative) sensitivity index, increments in $P_{extreme}$ events were determined with a corresponding change in the AMO state by 0.238 (–0.228). Table 8 lists the thresholds of 10–year recurrence interval $P_{extreme}$ events in the climate region as per the inverse–CDF of Burr XII distribution. Figure 23 illustrates the max–min–average plots of empirical probability of occurrence of 10–year or greater recurrence interval historical and projected $P_{extreme}$ events. The projected increased $P_{extreme}$ events from integrated sensitivity analysis of all the weather stations resulted in a 0–40% decrease in empirical probability of occurrence with an average decrease of 20%, whereas in the case of differentiated sensitivity analysis it decreased by 11–63% with an average decrease of 35%.

Table 8: Thresholds of 10–year recurrence interval annual precipitation extremes in Humid Sub–Tropical climate region as per Burr XII distribution

S. No.	**Weather Station**	**Precipitation (*in*.)**
1	Henderson	5.71
2	New Caney	6.9
3	Del Rio	4.91
4	Taylor Ranch	5.39

Table 8 Continued

S. No.	Weather Station	Precipitation (*in*.)
5	Chilress	3.55
6	Roscoe	4.39
7	Dallas	4.03
8	Dawson	5.5
9	Ennis	5.51
10	Proctor	5.44
11	Putnam	4.5
12	Rainbow	5.06
13	Waco	4.48
14	Austin	5.13
15	Elgin	5.09
16	San Antonio	6.24
17	Cleveland	7.17
18	Palacios	7.33

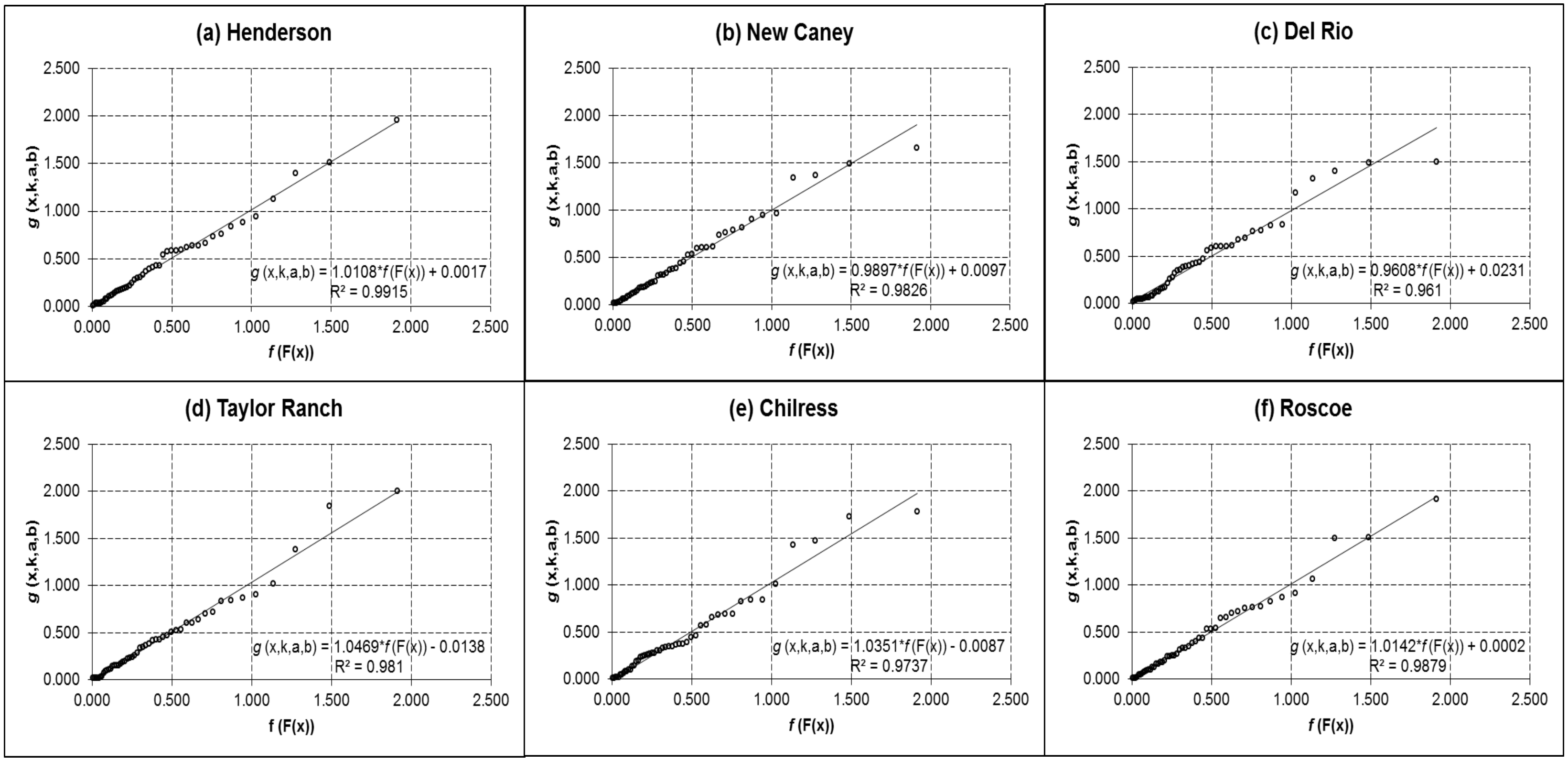

$$\left\{ g\left(x,k,a,b\right) \equiv k\log\left(1+\left(\frac{x}{b}\right)^{a}\right);\, f\left(F\left(x\right)\right) \equiv \log\left(\frac{1}{1-F\left(x\right)}\right)\right\}$$

Figure 22: Variation of the fit of Burr distribution for annual precipitation extremes (in.) in Humid Sub–Tropical climate region

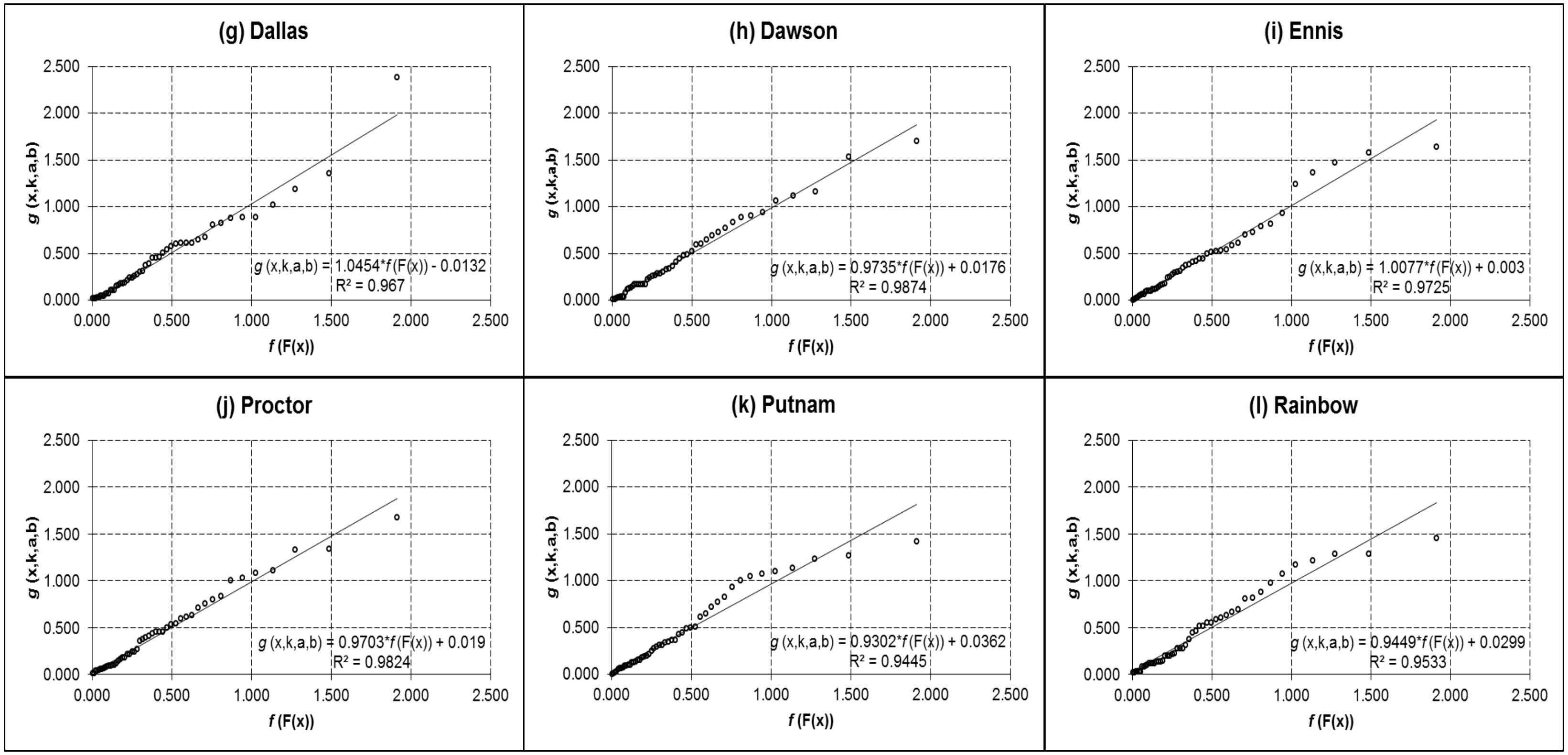

$$\left\{ g\left(x,k,a,b\right) \equiv k\log\left(1+\left(\frac{x}{b}\right)^{a}\right);\ f\left(F\left(x\right)\right) \equiv \log\left(\frac{1}{1-F\left(x\right)}\right) \right\}$$

Figure 22 Continued.

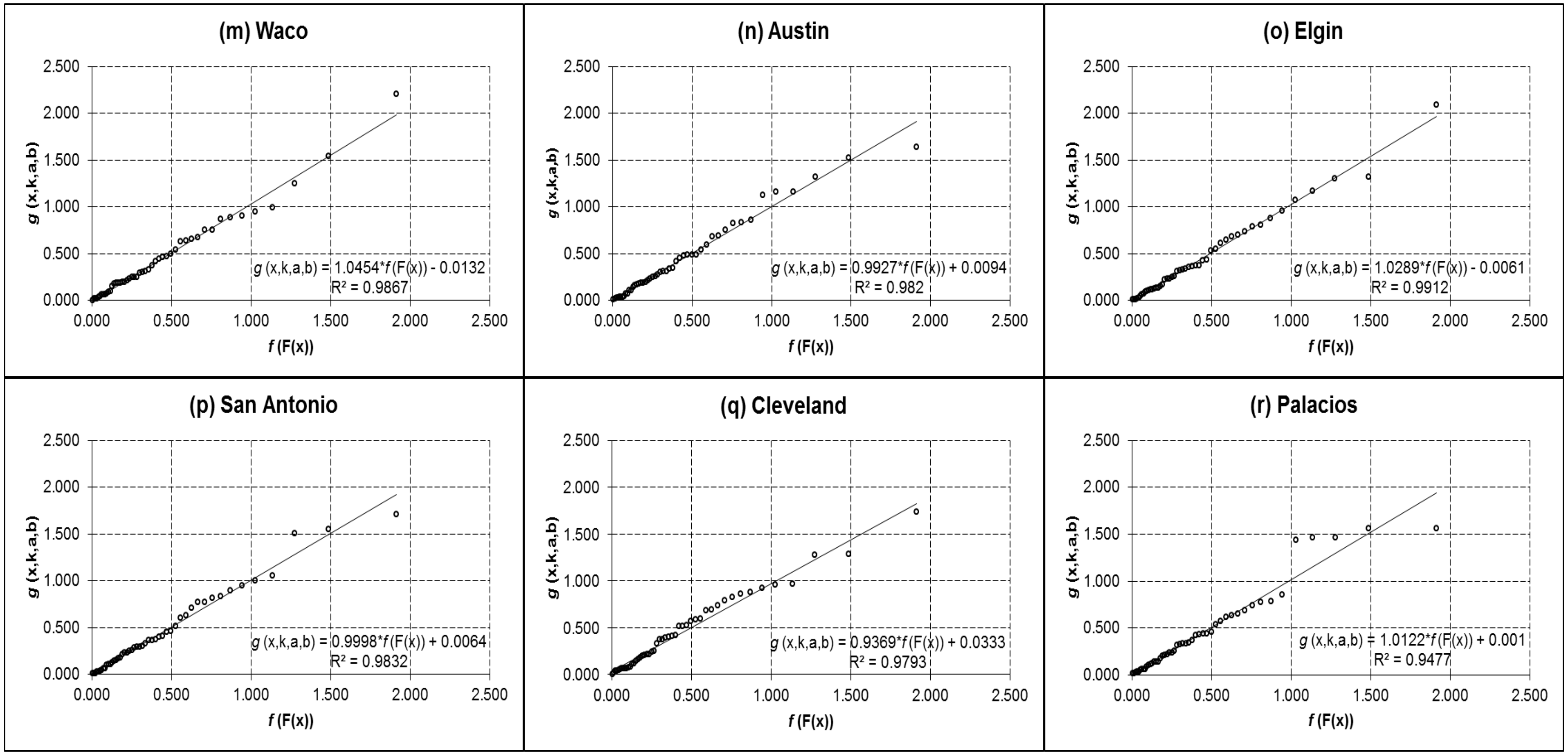

$$\left\{ g(x,k,a,b) \equiv k \log\left(1+\left(\frac{x}{b}\right)^{a}\right);\ f\left(F(x)\right) \equiv \log\left(\frac{1}{1-F(x)}\right) \right\}$$

Figure 22 Continued.

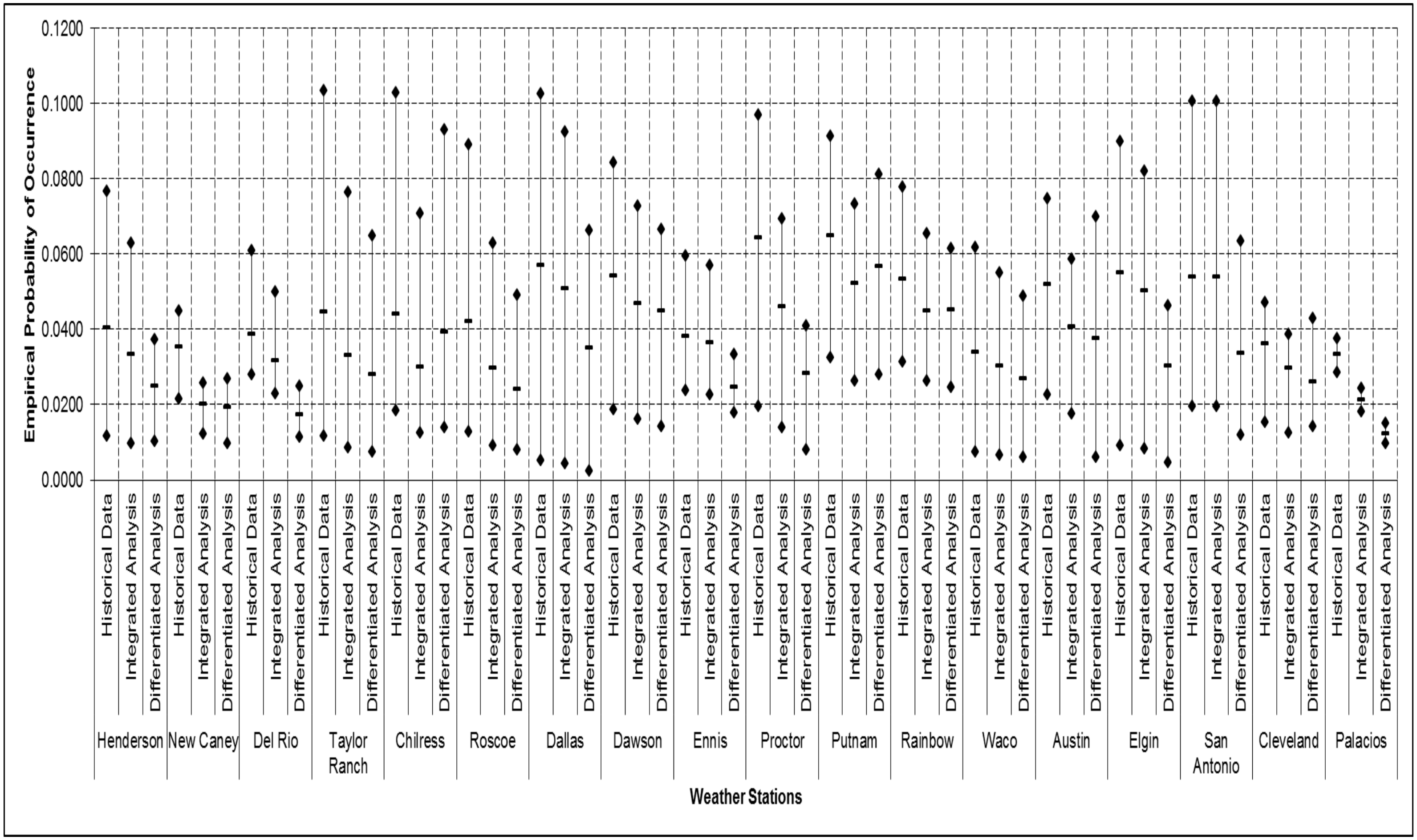

Figure 23: Degree of annual precipitation extremes in Humid Sub–Tropical climate region with respect to highest recorded consecutive month variation in AMO

CHAPTER VIII

SUMMARY AND CONCLUSION

Hydrometeorological literature unanimously predicts an overall intensified meteorology for the state of Texas (Karl 2009, Anderson et al. 2016, Melillo et al. 2014); however, their respective quantification failed to incorporate the highly spatially–variant geographical, topographical, and meteorological differences of the climate regions of the state. This research is based on the long–term seasonal climatic variations of the regions delineated by Köppen–Geiger Climate System: (i) Cold Desert/Semi–Arid Climate, (ii) Humid Sub–Tropical Climate, and (iii) Warm Desert/Semi–Arid Climate. For Research Objective I, a comprehensive analysis is done for the meteorological regimes of these climate regions, based upon the Standardized Precipitation Index (SPI) at a time scale of 3–months (McKee et al. 1993) and annual precipitation extremes ($P_{extreme}$). The observed changes in different ranges of wet periods and extreme precipitation events are further validated with the various temperature–related variables: (i) average seasonal temperature (T_{avg}–S), (ii) mean of maximum daily temperature in the season (EMXT–S), and (iii) total number of days with projected maximum temperature exceeding 90ºF in the season (DX90–S). Based on the Pearson Correlation approach coupled with Leave–One–Out–Test (LOOT) the results of Research Objective II illustrate that high–range extreme precipitation events across Texas are found to be significantly more correlated to Atlantic and Pacific Ocean based climatic cycles, in comparison to low– and mid–range extremes. The corresponding sample correlations for the extreme precipitation at

95% confidence interval were also found to be highly significant. This study is further extended in Research Objective III, where sensitivity of $P_{extreme}$ events is quantified to both warm and cold phases of the most correlated climatic cycles (differentiated sensitivity analysis) for the aforementioned climate regions, using linear least squares regression function (Bouwer et al. 2008). Significant differences are observed in sensitivity indices for different climate regions of Texas. Amongst these climate regions, the spatial variation of these statistical attributes is also studied with changing hydrometeorological properties of weather stations: (i) station elevation, (ii) average temperature, and (iii) average total precipitation.

It is determined under Research Objective I that in terms of changing climatic regimes of wet seasons, the Cold Desert/Semi–Arid Climate region observed an overall decrement in the total number of moderately wet seasons, no significant difference but extensive seasonal variations in the total number of considerably wet periods, and a three–fold increase in the total number of extremely wet seasons between the periods 1971–1990 and 1991–2010. The climate region is further likely to observe extreme precipitation events in the JJA and SON seasons, where the former observed an increment in both mid– and high–range extreme precipitation events and no significant difference in low–range extreme precipitation events, and the latter showed a decline in both low– and mid–range extreme precipitation events and a slight rise in high–range extreme precipitation events from 1971–1990 to 1991–2010. The region further illustrated significant seasonal variations in terms of average magnitude of precipitation and periodicity of events in different ranges of extremes. These changing climatic regimes can be attributed to the extensively variant and intensified temperature–related variables from 1971–1990 to 1991–2010, most remarkable of which are the increments in T_{avg}–S by 1.8ºF for DJF season, EMXT–S by 2.3ºF and DX90–S days by 21% for MAM season, and an additional 546 DX90–S days for JJA season. Based upon the statistical links determined under Research Objective II, the region is further found to be influenced by NAO, and the respective relationship is found to be mainly governed by historical average temperatures and temperature anomalies in the month of extremes, respectively. The stations with higher (lower) average temperature for the former and greater (lower) positive average temperature anomalies for the latter in the month of extremes have the tendency of receiving extreme precipitation in cold (warm) phase of NAO. However, sensitivity analysis in Research Objective III reveals that the $P_{extreme}$ events at the climate region are not sensitive to the variations in NAO.

The results of Research Objective I showed that the Humid Sub–Tropical Climate region illustrated no significant trend in the total number of moderately wet periods, whereas the region observed a constant increment for considerably wet periods from 1971–1980 to 2001–2010, and quadrupled the number of extremely wet periods in the period 1991–2010, in comparison to 1971–1990, with respect to a major shift in climatic regime for the DJF season. The extreme precipitation events are further likely to occur in the JJA and SON seasons. The respective climatic regimes observed a sharp intensification with increased number and decreased periodicity of low–, mid–, and high–range extremes. The only exception to the same is only the JJA season which illustrated a decline in the total number of low–range extreme precipitation events for the decade 1991–2000. Such changes in precipitation regimes are further attributed to the certain increments in temperature–related variables from 1971–1990 to 1991–2010, such as the increased T_{avg}–S for the DJF and SON seasons by 1.9ºF and 1.2ºF, amplified EMXT–S for MAM and JJA season by 1.8ºF and 1.3ºF, and rise in DX90–S days MAM and JJA season by 322 and 409 days. Under Research Objective II, these annual precipitation extremes ($P_{extreme}$) are shown to be impacted by the variations in AMO, and the stations with higher total precipitation or greater positive total precipitation anomaly are likely to receive extreme precipitation in the cold phase of AMO, and vice versa. Further, the $P_{extreme}$ events are determined to be significantly sensitive to the changing regimes of AMO, under Research Objective III. The respective sensitivity indices ranged between –0.526 and 0.627 for integrated sensitivity analysis, when no distinct phase of AMO is analyzed, and this band further gets intensified for the differentiated sensitivity analysis($Sensitivity\ Index_{Cold\ Phase} \in [-0.868, 0.876]; Sensitivity\ Index_{Warm\ Phase} \in [-0.800, 1.661]$). In the case of warm phase differentiated analysis, weather stations of the climate region with lower elevation and higher average precipitation are tremendously likely to observe a higher degree of $P_{extreme}$ events in warmer AMO states; however, no such statistical relationship could be established for cold phase differentiated analysis. Also, with respect to highest recorded historical change in AMO, the integrated sensitivity analysis determines a 20% decrement in empirical probabilities of projected $P_{extreme}$ events, whereas the differentiated sensitivity analysis determines an intensified decline of 35% in the same for the climate region.

In the case of the Warm Desert/Semi–Arid Climate region significant shifts in climatic regimes of wet seasons are observed, as determined under Research Objective I. The region illustrated a considerable decline in the total number of moderately and considerably wet periods, and low–range extreme precipitation events, and the simultaneous increments in the total number of extremely wet periods and mid–range extreme precipitation events. Similar to the other climate regions, the JJA and SON seasons are highly probable of observing extreme precipitation events. Here, 6 mid–range extremes occurred in the JJA season during 2001–2010, when historically the season observed merely 3 such events for the entire period of 1971–2000. Both of these seasons further observed a significant decline in terms of maximum–minimum–average periodicities of low– and mid–range extreme precipitation events. These shifts in precipitation regimes can be attributed to the following increments in temperature–related variables from 1971–1990 to 1991–2010; increased T_{avg}–S for DJF season from 48.9ºF to 51.0ºF, EMXT–S for MAM season from 101.2ºF to 103.4ºF, and DX90–S for MAM and JJA season by 125 and 119 days respectively. Similar to the Cold Desert/Semi–Arid Climate region, statistical links are observed between regional $P_{extreme}$ events and states of NAO under Research Objective II, but these events are not to be substantially sensitive to the variations in NAO.

This research illustrates noteworthy seasonal variations of the influence of changing climatic regimes on the meteorological processes of wet periods and extreme precipitation events in different climate regions of Texas. These analyses will aid regional water boards to understand the historical trends, which would help them prepare well for the making crucial decisions for managing water resources as per future climate change. The attributes of long–term predictability of climatic cycles classify them as potential indicators for analyzing and forecasting extreme precipitation with varying climate in Texas. Further, the classified approach of the differentiated sensitivity analysis will aid future research in developing a novel perspective while analyzing the statistical links between regional precipitation and global–scaled climatic cycles.

REFERENCES

Alvares, C. A., J. L. Stape, P. C. Sentelhas, G. de Moraes, J. Leonardo & G. Sparovek (2013) Köppen's climate classification map for Brazil. *Meteorologische Zeitschrift*, 22**,** 711-728.

Anderson, B. T., D. J. Gianotti, G. Salvucci & J. Furtado (2016) Dominant Time Scales of Potentially Predictable Precipitation Variations across the Continental United States. *Journal of Climate*, 29**,** 8881-8897.

Barlow, M., S. Nigam & E. Berbery (2001) ENSO, Pacific decadal variability, and US summertime precipitation, drought, and stream flow. *Journal of Climate,* 14**,** 2105-2128.

Bartier, P. M. & C. P. Keller (1996) Multivariate interpolation to incorporate thematic surface data using inverse distance weighting (IDW). *Computers & Geosciences,* 22**,** 795-799.

Bell, J. E., S. C. Herring, L. Jantarasami, C. Adrianopoli, K. Benedict, K. Conlon, V. Escobar, J. Hess, J. Luvall & C. P. Garcia-Pando (2016) Impacts of Extreme Events on Human Health. Chapter 4. *The Impacts of Climate Change on Human Health in the United States: A Scientific Assessment*. U.S. Global Change Research Program, Washington, DC, 99-128.

Berg, P., C. Moseley & J. O. Haerter (2013) Strong increase in convective precipitation in response to higher temperatures. *Nature Geoscience,* 6**,** 181-185.

Blunden, J. & D. S. Arndt (2016) State of the Climate in 2015. *Bulletin of the American Meteorological Society*, 97**,** Si-S275.

Booth, E. L., J. M. Byrne & D. L. Johnson (2012) Climatic changes in western North America, 1950–2005. *International Journal of Climatology,* 32**,** 2283-2300.

Bouwer, L. M., J. E. Vermaat & J. C. Aerts (2008) Regional sensitivities of mean and peak river discharge to climate variability in Europe. *Journal of Geophysical Research: Atmospheres,* 113**,** D19103.

Cai, W., P. Whetton & A. Pittock (2001) Fluctuations of the relationship between ENSO and northeast Australian rainfall. *Climate Dynamics,* 17**,** 421-432.

Chakravarti, I. M. & R. G. Laha. 1967. In *Handbook of methods of applied statistics,* ed. McGraw-Hill. New York, NY: John Wiley & Sons.

Chan, J. C. & W. Zhou (2005) PDO, ENSO and the early summer monsoon rainfall over south China. *Geophysical Research Letters,* 32**,** L08810.

Chen, F.-W. & C.-W. Liu (2012) Estimation of the spatial rainfall distribution using inverse distance weighting (IDW) in the middle of Taiwan. *Paddy and Water Environment,* 10**,** 209-222.

Chiew, F. H. & T. A. McMahon (2002) Global ENSO-streamflow teleconnection, streamflow forecasting and interannual variability. *Hydrological Sciences Journal,* 47**,** 505-522.

Cunnane, C. (1978) Unbiased plotting positions—a review. *Journal of Hydrology,* 37**,** 205-222.

Curtis, S. (2008) The Atlantic multidecadal oscillation and extreme daily precipitation over the US and Mexico during the hurricane season. *Climate Dynamics*, 30**,** 343-351.

Dai, A. (2013) The influence of the inter-decadal Pacific oscillation on US precipitation during 1923–2010. *Climate dynamics,* 41**,** 633-646.

De By, R. 2001. Principles of Geographic Information Systems, ITC Educational Textbook Series; 1, ITC Enschede. Enschede, The Netherlands: ISBN 90-6164-200-0.

Diaz, H. F. & J. K. Eischeid (2007) Disappearing "alpine tundra" Köppen climatic type in the western United States. *Geophysical Research Letters,* 34**,** L18707.

Dingman, S. L. 2015. *Physical hydrology*. Long Grove, IL: Waveland press.

Dore, M. H. (2005) Climate change and changes in global precipitation patterns: what do we know? *Environment international,* 31**,** 1167-1181.

Du, J., J. Fang, W. Xu & P. Shi (2013) Analysis of dry/wet conditions using the standardized precipitation index and its potential usefulness for drought/flood monitoring in Hunan Province, China. *Stochastic environmental research and risk assessment,* 27**,** 377-387.

Enfield, D. B., A. M. Mestas-Nuñez & P. J. Trimble (2001) The Atlantic multidecadal oscillation and its relation to rainfall and river flows in the continental US. *Geophysical Research Letters,* 28**,** 2077-2080.

Essenwanger, O. 2001. Classification of climates, world survey of climatology 1C, general climatology. Elsevier, Amsterdam.

Fan, H., J. Hu & D. He (2013) Trends in precipitation over the low latitude highlands of Yunnan, China. *Journal of Geographical Sciences,* 23**,** 1107-1122.

Feng, S., R. J. Oglesby, C. M. Rowe, D. B. Loope & Q. Hu (2008) Atlantic and Pacific SST influences on Medieval drought in North America simulated by the Community Atmospheric Model. *Journal of Geophysical Research: Atmospheres,* 113**,** D11101

Fisher, R. A. (1915) Frequency distribution of the values of the correlation coefficient in samples from an indefinitely large population. *Biometrika,* 10**,** 507-521.

Folland, C. K., A. W. Colman, D. P. Rowell & M. K. Davey (2001) Predictability of northeast Brazil rainfall and real-time forecast skill, 1987–98. *Journal of Climate,* 14**,** 1937-1958.

Francisco-Fernández, M. & A. Quintela-del-Río (2016) Comparing Simultaneous and Pointwise Confidence Intervals for Hydrological Processes. *PloS one,* 11**,** e0147505.

Geiger, R. (1954) Landolt-Börnstein–Zahlenwerte und Funktionen aus Physik, Chemie, Astronomie, Geophysik und Technik, alte Serie Vol. 3. *Ch. Klassifikation der Klimate nach W. Köppen.–Springer, Berlin***,** 603-607.

Gerlitz, L., S. Vorogushyn, H. Apel, A. Gafurov, K. Unger-Shayesteh & B. Merz (2016) A statistically based seasonal precipitation forecast model with automatic predictor selection and its application to central and south Asia. *Hydrology and Earth System Sciences,* 20**,** 4605.

Gleason, K. L., J. H. Lawrimore, D. H. Levinson, T. R. Karl & D. J. Karoly (2008) A revised US climate extremes index. *Journal of Climate*, 21**,** 2124-2137.

Gnanadesikan, A. & R. J. Stouffer (2006) Diagnosing atmosphere-ocean general circulation model errors relevant to the terrestrial biosphere using the Köppen climate classification. *Geophysical research letters,* 33**,** L22701.

Goldenberg, S. B., C. W. Landsea, A. M. Mestas-Nuñez & W. M. Gray (2001) The recent increase in Atlantic hurricane activity: Causes and implications. *Science,* 293**,** 474-479.

Goodess, C. & P. Jones (2002) Links between circulation and changes in the characteristics of Iberian rainfall. *International Journal of Climatology,* 22**,** 1593-1615.

Goodrich, G. B. & J. M. Walker (2011) The influence of the PDO on winter precipitation during high-and low-index ENSO conditions in the eastern United States. *Physical Geography,* 32**,** 295-312.

Greenwood, P. E. & M. S. Nikulin. 1996. *A guide to chi-squared testing*. New York, NY: John Wiley & Sons.

Griffith, G. E., S. A. Bryce, J. M. Omernik, J. Comstock, A. Rogers, B. Harrison, S. Hatch & D. Bezanson. 2004. *Ecoregions of Texas*. Corvallis, OR: US Geological Survey.

Grimm, A. M. (2003) The El Niño impact on the summer monsoon in Brazil: regional processes versus remote influences. *Journal of Climate,* 16**,** 263-280.

Gunn, J. R. 2016. Urban Patterns and Flood Damage in Texas Coastal Watersheds. College Station, TX: Texas A&M University.

Guttman, N. B. 1998. Comparing the palmer drought index and the standardized precipitation index1. 113-121. Wiley Online Library.

--- (1999) Accepting the standardized precipitation index: a calculation algorithm. *JAWRA Journal of the American Water Resources Association,* 35**,** 311-322.

Guttman, N. B. & R. G. Quayle (1996) A historical perspective of US climate divisions. *Bulletin of the American Meteorological Society,* 77**,** 293-303.

Haiden, T. & G. Pistotnik (2009) Intensity-dependent parameterization of elevation effects in precipitation analysis. *Advances in Geosciences,* 20**,** 33-38.

Hanson, L. S. & R. Vogel. 2008. The probability distribution of daily rainfall in the United States. In *World Environmental and Water Resources Congress*, 1-10.

Hayes, M. J., M. D. Svoboda, D. A. Wilhite & O. V. Vanyarkho (1999) Monitoring the 1996 drought using the standardized precipitation index. *Bulletin of the American Meteorological Society,* 80**,** 429-438.

Henderson, K. G. & P. J. Robinson (1994) Relationships between the pacific/north american teleconnection patterns and precipitation events in the south-eastern USA. *International Journal of Climatology,* 14**,** 307-323.

Hill, K., A. Taschetto & M. England (2011) Sensitivity of South American summer rainfall to tropical Pacific Ocean SST anomalies. *Geophysical Research Letters,* 38**,** L01701.

Houston, T. G. & S. A. Changnon (2007) Freezing rain events: a major weather hazard in the conterminous US. *Natural hazards,* 40**,** 485-494.

Hu, Q. & S. Feng (2008) Variation of the North American summer monsoon regimes and the Atlantic multidecadal oscillation. *Journal of Climate,* 21**,** 2371-2383.

--- (2012) AMO-and ENSO-driven summertime circulation and precipitation variations in North America. *Journal of Climate,* 25**,** 6477-6495.

Hu, Q., S. Feng & R. J. Oglesby (2011) Variations in North American summer precipitation driven by the Atlantic Multidecadal Oscillation. *Journal of Climate,* 24**,** 5555-5570.

Hurrell, J., Y. Kushnir, G. Ottersen & M. Visbeck (2003a) The North Atlantic Oscillation: climatic significance and environmental impact. AGU. *Geophysical Monograph Series,* 134.

Hurrell, J., Y. Kushnir, G. Ottersen & M. Visbeck. 2003b. An overview of the North Atlantic oscillation. *The North Atlantic Oscillation: climatic significance and environmental impact*. Wiley Online Library, 1-35.

Hurrell, J. W. (2002) Decadal trends in the North Atlantic oscillation. *Climate Change: Evaluating recent and future climate change,* 4**,** 201.

Hurrell, J. W. & C. Deser (2010) North Atlantic climate variability: the role of the North Atlantic Oscillation. *Journal of Marine Systems,* 79**,** 231-244.

Hurrell, J. W. & H. Van Loon. 1997. Decadal variations in climate associated with the North Atlantic Oscillation. In *Climatic Change at High Elevation Sites*, 69-94. Springer.

Johansson, Å. (2007) Prediction skill of the NAO and PNA from daily to seasonal time scales. *Journal of climate,* 20**,** 1957-1975.

Jones, C. & L. M. Carvalho (2014) Sensitivity to Madden–Julian Oscillation variations on heavy precipitation over the contiguous United States. *Atmospheric Research,* 147**,** 10-26.

Kalkomey, C. T. (1997) Potential risks when using seismic attributes as predictors of reservoir properties. *The Leading Edge,* 16**,** 247-251.

Karl. 2009. *Global climate change impacts in the United States*. New York, NY: Cambridge University Press.

Karl & W. J. Koss. 1984. *Regional and national monthly, seasonal, and annual temperature weighted by area, 1895-1983*. National Climatic Data Center.

Kawamura, R., M. Sugi & N. Sato (1995) Interdecadal and interannual variability in the northern extratropical circulation simulated with the JMA global model. Part I: Wintertime leading mode. *Journal of climate,* 8**,** 3006-3019.

Kerr, R. A. (2000) A North Atlantic climate pacemaker for the centuries. *Science,* 288**,** 1984-1985.

Kim, J. & J. A. Fessler (2004) Intensity-based image registration using robust correlation coefficients. *IEEE transactions on medical imaging,* 23**,** 1430-1444.

Kimmel Jr, T. M., J. Nielsen-Gammon, B. Rose & H. M. Mogil (2016) The Weather and Climate of Texas: A Big State With Big Extremes. *Weatherwise,* 69**,** 25-33.

Knight, J. R., C. K. Folland & A. A. Scaife (2006) Climate impacts of the Atlantic multidecadal oscillation. *Geophysical Research Letters,* 33.

Knudsen, M. F., M.-S. Seidenkrantz, B. H. Jacobsen & A. Kuijpers (2011) Tracking the Atlantic Multidecadal Oscillation through the last 8,000 years. *Nature Communications,* 2**,** 178.

Köppen, W. (1900) Versuch einer Klassifikation der Klimate, vorzugsweise nach ihren Beziehungen zur Pflanzenwelt. *Geographische Zeitschrift,* 6**,** 593-611.

Kottek, M., J. Grieser, C. Beck, B. Rudolf & F. Rubel (2006) World map of the Köppen-Geiger climate classification updated. *Meteorologische Zeitschrift,* 15**,** 259-263.

Krause, P., D. Boyle & F. Bäse (2005) Comparison of different efficiency criteria for hydrological model assessment. *Advances in Geosciences,* 5**,** 89-97.

Kripalani, R. & A. Kulkarni (2001) Monsoon rainfall variations and teleconnections over South and East Asia. *International Journal of Climatology,* 21**,** 603-616.

Kumar, M. Bindi, A. Crisci & G. Maracchi (2013) Detection of variations in precipitation at different time scales of twentieth century at three locations of Italy. *Weather and Climate Extremes,* 2**,** 7-15.

Kumar, C. Murthy, M. Sesha Sai & P. Roy (2009) On the use of Standardized Precipitation Index (SPI) for drought intensity assessment. *Meteorological applications,* 16**,** 381-389.

Kurtzman, D. & B. R. Scanlon (2007) El Nino–Southern Oscillation and Pacific Decadal Oscillation impacts on precipitation in the southern and central United States: Evaluation of spatial distribution and predictions. *Water Resources Research,* 43.

Lamb, P. & R. Peppler. 1991. West Africa, Teleconnections Linking Worldwide Climate Anomalies MH Glantz, RW Katz, N. Nicholls, 121–190. New York, NY: Cambridge Univ. Press.

Leathers, D. J., B. Yarnal & M. A. Palecki (1991) The Pacific/North American teleconnection pattern and United States climate. Part I: Regional temperature and precipitation associations. *Journal of Climate,* 4**,** 517-528.

Li, W., R. Fu, R. I. N. Juarez & K. Fernandes (2008) Observed change of the standardized precipitation index, its potential cause and implications to future climate change in the Amazon region. *Philosophical Transactions of the Royal Society of London B: Biological Sciences,* 363**,** 1767-1772.

Lloyd-Hughes, B. & M. A. Saunders (2002) A drought climatology for Europe. *International journal of climatology,* 22**,** 1571-1592.

López-Moreno, J., S. Vicente-Serrano, E. Morán-Tejeda, J. Lorenzo-Lacruz, A. Kenawy & M. Beniston (2011) Effects of the North Atlantic Oscillation (NAO) on combined temperature and precipitation winter modes in the Mediterranean mountains: observed relationships and projections for the 21st century. *Global and Planetary Change,* 77**,** 62-76.

Lü, A., S. Jia, W. Zhu, H. Yan, S. Duan & Z. Yao (2011) El Niño-Southern Oscillation and water resources in the headwaters region of the Yellow River: links and potential for forecasting. *Hydrology and Earth System Sciences,* 15**,** 1273-1281.

Lu, H., E. Ip, J. Scott, P. Foster, M. Vickers & L. L. Baxter (2010) Effects of particle shape and size on devolatilization of biomass particle. *Fuel*, 89**,** 1156-1168.

Lu, R. & B. Dong (2005) Impact of Atlantic sea surface temperature anomalies on the summer climate in the western North Pacific during 1997–1998. *Journal of Geophysical Research: Atmospheres,* 110**,** D16102.

Lyons, S. W. (1990) Spatial and temporal variability of monthly precipitation in Texas. *Monthly weather review*, 118**,** 2634-2648.

MacDonald, G. M. & R. A. Case (2005) Variations in the Pacific Decadal Oscillation over the past millennium. *Geophysical Research Letters*, 32**,** L08703

Mantua, N. J. & S. R. Hare (2002) The Pacific decadal oscillation. *Journal of oceanography,* 58**,** 35-44.

Marani, M. & S. Zanetti (2015) Long-term oscillations in rainfall extremes in a 268 year daily time series. *Water Resources Research,* 51**,** 639-647.

Marshall, J., Y. Kushnir, D. Battisti, P. Chang, A. Czaja, R. Dickson, J. Hurrell, M. McCARTNEY, R. Saravanan & M. Visbeck (2001) North Atlantic climate variability: phenomena, impacts and mechanisms. *International Journal of Climatology,* 21**,** 1863-1898.

McKee, T. B., N. J. Doesken & J. Kleist. 1993. The relationship of drought frequency and duration to time scales. In *Proceedings of the 8th Conference on Applied Climatology,* 179-183. American Meteorological Society Boston, MA.

McMahon, T. A., M. C. Peel, R. M. Vogel & G. G. Pegram (2007) Global streamflows–Part 3: Country and climate zone characteristics. *Journal of Hydrology,* 347**,** 272-291.

McRoberts, D. B. & J. W. Nielsen-Gammon (2012) The use of a high-resolution standardized precipitation index for drought monitoring and assessment. *Journal of Applied Meteorology and Climatology,* 51**,** 68-83.

Melillo, J. M., T. Richmond & G. Yohe (2014) Climate change impacts in the United States. *Third National Climate Assessment*.

Minobe, S. (2000) Spatio-temporal structure of the pentadecadal variability over the North Pacific. *Progress in Oceanography,* 47**,** 381-408.

Mishra, A. K. & V. P. Singh (2010) Changes in extreme precipitation in Texas. *Journal of Geophysical Research: Atmospheres,* 115**,** D14106.

Mo, K. C. (2010) Interdecadal modulation of the impact of ENSO on precipitation and temperature over the United States. *Journal of Climate,* 23**,** 3639-3656.

Montanari, A. (2007) What do we mean by 'uncertainty'? The need for a consistent wording about uncertainty assessment in hydrology. *Hydrological Processes,* 21**,** 841-845.

Murgulet, V., R. Hay & M. Lopez. 2012. Climate Phenomena Impact on South Texas Rainfall Patterns. In *AGU Fall Meeting Abstracts,* 0165.

Nielsen-Gammon, J. W. (2011) The changing climate of Texas. *The impact of global warming on Texas***,** 39-68.

Nielsen-Gammon, J. W., F. Zhang, A. M. Odins & B. Myoung (2005) Extreme rainfall in Texas: Patterns and predictability. *Physical Geography,* 26**,** 340-364.

Nielsen, E. R., R. S. Schumacher & A. M. Keclik (2016) The effect of the Balcones Escarpment on three cases of extreme precipitation in Central Texas. *Monthly Weather Review,* 144**,** 119-138.

Niven, E. B. & C. V. Deutsch (2012) Calculating a robust correlation coefficient and quantifying its uncertainty. *Computers & Geosciences,* 40**,** 1-9.

Nogueira, R. C. & B. D. Keim (2010) Annual volume and area variations in tropical cyclone rainfall over the eastern United States. *Journal of Climate,* 23**,** 4363-4374.

Ottersen, G., B. Planque, A. Belgrano, E. Post, P. C. Reid & N. C. Stenseth (2001) Ecological effects of the North Atlantic oscillation. *Oecologia,* 128**,** 1-14.

Parazoo, N. C., E. Barnes, J. Worden, A. B. Harper, K. B. Bowman, C. Frankenberg, S. Wolf, M. Litvak & T. F. Keenan (2015) Influence of ENSO and the NAO on terrestrial carbon uptake in the Texas-northern Mexico region. *Global Biogeochemical Cycles,* 29**,** 1247-1265.

Pearson, K. (1920) Notes on the history of correlation. *Biometrika,* 13**,** 25-45.

Peel, M. C., B. L. Finlayson & T. A. McMahon (2007) Updated world map of the Köppen-Geiger climate classification. *Hydrology and earth system sciences discussions,* 4**,** 439-473.

Pianosi, F., K. Beven, J. Freer, J. W. Hall, J. Rougier, D. B. Stephenson & T. Wagener (2016) Sensitivity analysis of environmental models: A systematic review with practical workflow. *Environmental Modelling & Software,* 79**,** 214-232.

Pielke Jr, R. A., J. Gratz, C. W. Landsea, D. Collins, M. A. Saunders & R. Musulin (2008) Normalized hurricane damage in the United States: 1900–2005. *Natural Hazards Review,* 9**,** 29-42.

Power, S., M. Haylock, R. Colman & X. Wang (2006) The predictability of interdecadal changes in ENSO activity and ENSO teleconnections. *Journal of Climate,* 19**,** 4755-4771.

Press, W. H., S. A. Teukolsky, W. T. Vetterling & B. P. Flannery. 1992. Numerical Recipes in C. New York, NY: Cambridge Univ. Press.

Pryor, S. C., D. Scavia, C. Downer, M. Gaden, L. Iverson, R. Nordstrom, J. Patz & G. P. Robertson (2014) Midwest. Climate change impacts in the United States. *The third national climate assessment*.

Quadrelli, R. & J. M. Wallace (2004) A simplified linear framework for interpreting patterns of Northern Hemisphere wintertime climate variability. *Journal of Climate*, 17**,** 3728-3744.

Ramos, M. H., T. Mathevet, J. Thielen & F. Pappenberger (2010) Communicating uncertainty in hydro-meteorological forecasts: mission impossible? *Meteorological Applications*, 17**,** 223-235.

Renard, B. & U. Lall (2014) Regional frequency analysis conditioned on large-scale atmospheric or oceanic fields. *Water Resources Research*, 50**,** 9536-9554.

Ropelewski, C. F. & M. S. Halpert (1996) Quantifying southern oscillation-precipitation relationships. *Journal of climate*, 9**,** 1043-1059.

Rubel, F. & M. Kottek (2010) Observed and projected climate shifts 1901–2100 depicted by world maps of the Köppen-Geiger climate classification. *Meteorologische Zeitschrift*, 19**,** 135-141.

Schlesinger, M. E. & N. Ramankutty (1994) An oscillation in the global climate system of period 65-70 years. *Nature*, 367**,** 723-726.

Schmandt, J., G. R. North & J. Clarkson. 2011. *The Impact of Global Warming on Texas*. Austin, TX: University of Texas Press.

Schneider, N. & B. D. Cornuelle (2005) The forcing of the pacific decadal oscillation*. *Journal of Climate*, 18**,** 4355-4373.

Shukla, J. & J. Wallace (1983) Numerical simulation of the atmospheric response to equatorial Pacific sea surface temperature anomalies. *Journal of the Atmospheric Sciences*, 40**,** 1613-1630.

Silva, G. & T. Ambrizzi (2006) Inter-El Niño variability and its impact on the South American low-level jet east of the Andes during austral summer? two case studies. *Advances in Geosciences,* 6**,** 283-287.

Smith, V. D. & L. S. Campbell. 1996. *Exploring Texas ecoregions*. Austin TX: Texas Parks and Wildlife Department.

Sorooshian, S., B. Imam, S. Mahani, T. Pagano & M. Whitaker (2003) Hydrologic sciences and water resources management issues in a changing world. *Developments in Water Science,* 50**,** 83-92.

Squires, M. F., J. H. Lawrimore, R. R. Heim Jr, D. A. Robinson, M. R. Gerbush & T. W. Estilow (2014) The regional snowfall index. *Bulletin of the American Meteorological Society,* 95**,** 1835-1848.

Stephens, M. A. (1974) EDF statistics for goodness of fit and some comparisons. *Journal of the American statistical Association,* 69**,** 730-737.

Stocker, T., D. Qin, G. Plattner & L. Alexander (2013) Technical summary in IPCC AR5 WG1 2013. *National Aeronautics and Space Administration Goddard Institute for Space Studies.*

Sutton, R. T. & D. L. Hodson (2005) Atlantic Ocean forcing of North American and European summer climate. *science,* 309**,** 115-118.

--- (2007) Climate response to basin-scale warming and cooling of the North Atlantic Ocean. *Journal of Climate,* 20**,** 891-907.

Svoboda, M., M. Hayes & D. Wood (2012) Standardized precipitation index user guide. *World Meteorological Organization Geneva, Switzerland*.

Thom, H. C. S. 1966. *Some methods of climatological analysis*. Geneva, Switzerland: Secretariat of the World Meteorological Organization Geneva.

Tippett, M. K., A. H. Sobel, S. J. Camargo & J. T. Allen (2014) An empirical relation between US tornado activity and monthly environmental parameters. *Journal of Climate,* 27**,** 2983-2999.

Tobler, W. R. (1970) A computer movie simulating urban growth in the Detroit region. *Economic geography,* 46**,** 234-240.

Trenberth, K. E. (2011) Changes in precipitation with climate change. *Climate Research,* 47**,** 123-138.

Trenberth, K. E. & J. M. Caron (2000) The Southern Oscillation revisited: Sea level pressures, surface temperatures, and precipitation. *Journal of Climate,* 13**,** 4358-4365.

Trenberth, K. E., A. Dai, R. M. Rasmussen & D. B. Parsons (2003) The changing character of precipitation. *Bulletin of the American Meteorological Society,* 84**,** 1205-1217.

Trenberth, K. E. & J. W. Hurrell (1994) Decadal atmosphere-ocean variations in the Pacific. *Climate Dynamics,* 9**,** 303-319.

Trenberth, K. E., J. W. Hurrell & D. P. Stepaniak. 2006. The Asian monsoon: global perspectives. In *The Asian Monsoon*, 67-87. Springer.

Troup, A. (1965) The 'southern oscillation'. *Quarterly Journal of the Royal Meteorological Society,* 91**,** 490-506.

Vose, R. S., S. Applequist, M. Squires, I. Durre, M. J. Menne, C. N. Williams Jr, C. Fenimore, K. Gleason & D. Arndt (2014) Improved historical temperature and precipitation time series for US climate divisions. *Journal of Applied Meteorology and Climatology,* 53**,** 1232-1251.

Wallace, J. M. & D. S. Gutzler (1981) Teleconnections in the geopotential height field during the Northern Hemisphere winter. *Monthly Weather Review,* 109**,** 784-812.

Wang, G., R. Kleeman, N. Smith & F. Tseitkin (2002) The BMRC coupled general circulation model ENSO forecast system. *Monthly weather review,* 130**,** 975-991.

Wanner, H., J. Beer, J. Bütikofer, T. J. Crowley, U. Cubasch, J. Flückiger, H. Goosse, M. Grosjean, F. Joos & J. O. Kaplan (2008) Mid-to Late Holocene climate change: an overview. *Quaternary Science Reviews,* 27**,** 1791-1828.

Ward, P. J., W. Beets, L. M. Bouwer, J. C. Aerts & H. Renssen (2010) Sensitivity of river discharge to ENSO. *Geophysical Research Letters,* 37**,** L12402.

Weng, H., S. K. Behera & T. Yamagata (2009) Anomalous winter climate conditions in the Pacific rim during recent El Niño Modoki and El Niño events. *Climate Dynamics,* 32**,** 663-674.

WGII, I. (2014) Climate Change 2014: Impacts, Adaptation, and Vulnerability-AR5 Summary for Policymakers. *WGII AR5 Phase I, Report Launch,* 1**,** 31.

Wu, H., M. D. Svoboda, M. J. Hayes, D. A. Wilhite & F. Wen (2007) Appropriate application of the standardized precipitation index in arid locations and dry seasons. *International Journal of Climatology,* 27**,** 65-79.

Yan, H., L. Sun, Y. Wang, W. Huang, S. Qiu & C. Yang (2011) A record of the Southern Oscillation Index for the past 2,000 years from precipitation proxies. *Nature Geoscience,* 4**,** 611-614.

Zhang, Q., C.-Y. Xu & Z. Zhang (2009) Observed changes of drought/wetness episodes in the Pearl River basin, China, using the standardized precipitation index and aridity index. *Theoretical and Applied Climatology,* 98**,** 89-99.

Zhao, G., H. Gao & L. Cuo (2016) Effects of Urbanization and Climate Change on Peak Flows over the San Antonio River Basin, Texas. *Journal of Hydrometeorology,* 17**,** 2371-2389.

Zhu, L., O. W. Frauenfeld & S. M. Quiring (2013) Seasonal tropical cyclone precipitation in Texas: A statistical modeling approach based on a 60 year climatology. *Journal of Geophysical Research: Atmospheres,* 118**,** 8842-8856.

APPENDIX A

CLASSIFIATION OF ANNUAL PRECIPITATION EXTREMES

Table A–1 lists 47 probability distributions, which were fitted to derive annual precipitation extremes ($P_{extreme}$) for the state of Texas using EasyFit distribution fitting software developed by MathWave Technologies (http://www.mathwave.com/easyfit–distribution–fitting.html), in order to extract the thresholds of $P_{extreme}$ corresponding to the recurrence interval of 2, 5, and 10 years.

Table A–1: List of probability distributions

Probability Distribution **[Domain]** **{Constraints/Conditions}**	**Probability Density Function (PDF)**	**Cumulative Density Function (CDF)**
Beta $\left[a \le x \le b\right]$	$f\left(x\right)=\left(\frac{1}{B\left(\lambda_1,\lambda_2\right)}\right)\left(\frac{\left(x-a\right)^{\lambda_1-1}\left(b-x\right)^{\lambda_2-1}}{\left(b-a\right)^{\lambda_1+\lambda_2-1}}\right)$ where B is the Beta Function, λ_1 and λ_2 are	$F\left(x\right)=I_X\left(\lambda_1,\lambda_2\right)$ where $X \equiv \frac{x-a}{x-b}$ and I_X is the

	continuous shape parameters $(\lambda_1 > 0; \lambda_2 > 0)$, and a and b are continuous boundary parameters ($a < b$)	Regularized Incomplete Beta Function.
Burr (4–Parameter) $[\gamma \le x < \infty]$	$$f(x) = \frac{\alpha z \left(\frac{x-\gamma}{\beta}\right)^{\alpha-1}}{\beta \left(1+\left(\frac{x-\gamma}{\beta}\right)^{\alpha}\right)^{z+1}}$$ where z and α are the continuous shape parameter $(z > 0; \alpha > 0)$, β is the continuous scale parameter (β > 0), and γ is the continuous location parameter ($\gamma \equiv 0$).	$$F(x) = 1 - \left(1+\left(\frac{x-\gamma}{\beta}\right)^{\alpha}\right)^{-z}$$
Burr (3–Parameter)	$$f(x) = \frac{\alpha z \left(\frac{x}{\beta}\right)^{\alpha-1}}{\beta \left(1+\left(\frac{x}{\beta}\right)^{\alpha}\right)^{z+1}}$$	$$F(x) = 1 - \left(1+\left(\frac{x}{\beta}\right)^{\alpha}\right)^{-z}$$

Cauchy $\left[-\infty < x < \infty\right]$	$$f(x)=\frac{1}{\left(\pi\sigma\left(1+\left(\frac{x-\mu}{\sigma}\right)^{2}\right)\right)}$$ where σ is the continuous scale parameter (σ > 0) and μ is the continuous location parameter.	$$F(x)=\frac{1}{\pi}\arctan\left(\frac{x-\mu}{\sigma}\right)+0.5$$
Chi–Squared (2–Parameter) $\left[\gamma \le x < \infty\right]$	$$f(x)=\frac{(x-\gamma)^{\nu/2-1}e^{\left(\frac{-(x-\nu)}{2}\right)}}{2^{\nu/2}\Gamma\left(\nu/2\right)}$$ where ν is the degree or freedom (ν > 0) and γ is the continuous location parameter ($\gamma \equiv 0$).	$$F(x)=\frac{\Gamma_{(x-\gamma)/2}\left(\nu/2\right)}{\Gamma\left(\nu/2\right)}$$
Chi–Squared (1–Parameter)	$$f(x)=\frac{x^{\nu/2-1}e^{\left(\frac{-x}{2}\right)}}{2^{\nu/2}\Gamma\left(\nu/2\right)}$$	$$F(x)=\frac{\Gamma_{x/2}\left(\nu/2\right)}{\Gamma\left(\nu/2\right)}$$

Dagum $\left[\gamma \le x < \infty\right]$	$$f(x)=\frac{\alpha z\left(\frac{x-\gamma}{\beta}\right)^{\alpha z-1}}{\beta\left(1+\left(\frac{x-\gamma}{\beta}\right)^{\alpha}\right)^{z+1}}$$ where z and α are the continuous shape parameter $\left(z>0;\alpha>0\right)$, β is the continuous scale parameter (β > 0), and γ is the continuous location parameter ($\gamma \equiv 0$).	$$F(x)=\left(1+\left(\frac{x-\gamma}{\beta}\right)^{-\alpha}\right)^{-z}$$
Erlang (3–Parameter) $\left[\gamma \le x < \infty\right]$	$$f(x)=\frac{\left(x-\gamma\right)^{\alpha-1}}{\beta^{\alpha}\Gamma(\alpha)}e^{\left(\frac{-(x-\gamma)}{\beta}\right)}$$ where α is the shape parameter (α > 0), β is the continuous scale parameter (β > 0), and γ is the continuous location parameter ($\gamma \equiv 0$).	$$F(x)=\frac{\Gamma_{(x-\gamma)/\beta}(\alpha)}{\Gamma(\alpha)}$$

Erlang (2–Parameter)	$f(x)=\dfrac{x^{\alpha-1}}{\beta^{\alpha}\Gamma(\alpha)}e^{\left(\frac{-x}{\beta}\right)}$	$F(x)=\dfrac{\Gamma_{x/\beta}(\alpha)}{\Gamma(\alpha)}$
Error $\left[-\infty<x<\infty\right]$	$f(x)=\dfrac{\alpha}{\sigma}e^{-\lvert\beta k\rvert}$ $\beta=\sqrt{\left(\dfrac{\Gamma\left(3/k\right)}{\Gamma\left(1/k\right)}\right)}$; $\alpha=\dfrac{k\beta}{2\Gamma\left(1/k\right)}$; $z\equiv\dfrac{x-\mu}{\sigma}$ where k is the continuous shape parameter, σ is the continuous scale parameter ($\sigma>0$), and μ is the continuous location parameter.	$F(x)=\begin{cases}0.5\left(1+\dfrac{\Gamma_{\lvert\beta z\rvert^{k}}\left(1/k\right)}{\Gamma\left(1/k\right)}\right)\forall\, x\geq\mu\\ 0.5\left(1-\dfrac{\Gamma_{\lvert\beta z\rvert^{k}}\left(1/k\right)}{\Gamma\left(1/k\right)}\right)\forall\, x<\mu\end{cases}$
Error Function $\left[-\infty<x<\infty\right]$	$f(x)=\dfrac{\gamma}{e^{(\gamma x)^{2}}\sqrt{\pi}}$ where γ is the continuous inverse scale parameter ($\gamma>0$) ,	$F(x)=\Phi\left(\sqrt{2}\gamma x\right)$ where Φ is the Laplace Integral.
Exponential (2–Parameter)	$f(x)=\dfrac{\lambda}{e^{\lambda(x-\gamma)}}$	$F(x)=1-\dfrac{1}{e^{\lambda(x-\gamma)}}$

$\left[\gamma \le x < \infty\right]$	where λ is the continuous inverse scale parameter ($\lambda >$ 0), and γ is the continuous location parameter ($\gamma \equiv 0$).	
Exponential (1–Parameter)	$f\left(x\right)=\frac{\lambda}{e^{\lambda x}}$	$F\left(x\right)=1-\frac{1}{e^{\lambda x}}$
F $\left[0 \le x < \infty\right]$	$f\left(x\right)=\frac{1}{x\beta\left(\nu_1,\nu_2\right)}\sqrt{\frac{\left(\nu_1 x\right)^{\nu_1}\nu_2^{\nu_2}}{\left(\nu_1 x+\nu_2\right)^{\nu_1+\nu_2}}}$ where ν_1 and ν_2 are the degrees of freedom $\left(\nu_1>0;\nu_2>0\right)$, and β is the Beta Function.	$F\left(x\right)=I_X\left(\nu_1,\nu_2\right)$ where $X \equiv \frac{\nu_1 x}{\nu_1 x+\nu_2}$, and I_X is the Regularized Incomplete Beta Function.
Fatigue Life (3–Parameter) $\left[\gamma < x < \infty\right]$	$f\left(x\right)=\frac{\sqrt{\left(x-\gamma\right)/\beta}+\sqrt{\beta/\left(x-\gamma\right)}}{2\alpha\left(x-\gamma\right)}\cdot\phi\left(\frac{1}{\alpha}\left(\sqrt{\frac{x-\gamma}{\beta}}-\sqrt{\frac{\beta}{x-\gamma}}\right)\right)$ where α is the shape parameter ($\alpha >$ 0), β is the continuous scale parameter (β > 0), γ is the continuous location parameter $\left(\gamma \equiv 0\right)$, ϕ is the	$F\left(x\right)=\Phi\left[\frac{1}{\alpha}\left(\sqrt{\frac{x-\gamma}{\beta}}-\sqrt{\frac{\beta}{x-\gamma}}\right)\right]$ where Φ is the Laplace Integral.

	PDF of standard Normal Distribution.	
Fatigue Life (2–Parameter)	$f(x)=\frac{\sqrt{x/\beta}+\sqrt{\beta/x}}{2\alpha x}.\phi\left(\frac{1}{\alpha}\left(\sqrt{\frac{x}{\beta}}-\sqrt{\frac{\beta}{x}}\right)\right)$	$F(x)=\Phi\left[\frac{1}{\alpha}\left(\sqrt{\frac{x}{\beta}}-\sqrt{\frac{\beta}{x}}\right)\right]$
Frechet (3–Parameter) $\left[\gamma<x<\infty\right]$	$f(x)=\frac{\alpha}{\beta}\left(\frac{\beta}{x-\gamma}\right)^{\alpha+1}e^{-\left(\beta/x-\gamma\right)^{\alpha}}$ where α is the shape parameter (α > 0), β is the continuous scale parameter (β > 0), and γ is the continuous location parameter $(\gamma\equiv 0)$.	$F(x)=e^{-\left(\beta/x-\gamma\right)^{\alpha}}$
Frechet (2–Parameter)	$f(x)=\frac{\alpha}{\beta}\left(\frac{\beta}{x}\right)^{\alpha+1}e^{-\left(\beta/x\right)^{\alpha}}$	$F(x)=e^{-\left(\beta/x\right)^{\alpha}}$
Gamma (3–Parameter) $\left[\gamma\le x<\infty\right]$	$f(x)=\frac{(x-\gamma)^{\alpha-1}}{\beta^{\alpha}\Gamma(\alpha)}e^{-\left((x-\gamma)/\beta\right)}$ where α is the shape parameter (α > 0), β is the continuous scale parameter (β > 0), and γ is the	$F(x)=\frac{\Gamma_{(x-\gamma)/\beta}(\alpha)}{\Gamma(\alpha)}$

	continuous location parameter $(\gamma \equiv 0)$.	
Gamma (2–Parameter)	$f(x)=\dfrac{x^{\alpha-1}}{\beta^{\alpha}\Gamma(\alpha)}e^{-x/\beta}$	$F(x)=\dfrac{\Gamma_{x/\beta}(\alpha)}{\Gamma(\alpha)}$
Generalized Extreme Value $\begin{bmatrix} 1+\alpha\left(\dfrac{x-\gamma}{\beta}\right)>0\,\forall\alpha\neq 0 \\ -\infty<x<\infty\,\forall\alpha=0 \end{bmatrix}$	$f(x)=\begin{cases}\dfrac{1}{\beta}e^{\left(-(1+\alpha z)^{-1/\alpha}\right)(1+\alpha z)^{-(1+1/\alpha)}} \forall\alpha\neq 0 \\ \dfrac{1}{\beta}e^{-\left(z+e^{-z}\right)}\forall\alpha=0\end{cases}$ where α is the shape parameter, β is the continuous scale parameter (β > 0), and γ is the continuous location parameter.	$F(x)=\begin{cases}e^{-(1+\alpha z)^{-1/\alpha}}\forall\alpha\neq 0 \\ e^{-e^{-z}}\forall\alpha=0\end{cases}$ where $z\equiv\dfrac{x-\gamma}{\beta}$.
Generalized Gamma (4–Parameter) $[\gamma\leq x<\infty]$	$f(x)=\dfrac{\lambda_1(x-\gamma)^{\lambda_1\lambda_2-1}}{\beta^{\lambda_1\lambda_2}\Gamma(\lambda_2)}e^{-\left(\frac{x-\gamma}{\beta}\right)^{\lambda_1}}$ where λ_1 and λ_2 are continuous shape parameters $(\lambda_1>0;\lambda_2>0)$, β is the continuous scale parameter (β > 0), and γ is the continuous	$F(x)=\dfrac{\Gamma_{\left(x-\gamma/\beta\right)^{\lambda_1}}(\lambda_2)}{\Gamma(\lambda_2)}$

	location parameter ($\gamma \equiv 0$).	
Generalized Gamma (3–Parameter)	$$f(x) = \frac{\lambda_1 x^{\lambda_1\lambda_2 - 1}}{\beta^{\lambda_1\lambda_2}\Gamma(\lambda_2)} e^{-\left(\frac{x}{\beta}\right)^{\lambda_1}}$$	$$F(x) = \frac{\Gamma_{\left(x/\beta\right)^{\lambda_1}}(\lambda_2)}{\Gamma(\lambda_2)}$$
Generalized Logistic $\left[\begin{array}{c} 1+\alpha\dfrac{(x-\mu)}{\sigma} > 0 \,\forall\, \alpha \neq 0 \\ -\infty < x < \infty \,\forall\, \alpha = 0 \end{array}\right]$	$$f(x) = \begin{cases} \dfrac{(1+\alpha z)^{-(1+1/\alpha)}}{\sigma\left(1+(1+\alpha z)^{-1/\alpha}\right)^2} \,\forall\, \alpha \neq 0 \\ \dfrac{e^{-z}}{\sigma\left(1+e^{-z}\right)^2} \,\forall\, \alpha = 0 \end{cases}$$ where α is the continuous shape parameter, σ is the continuous scale parameter ($\sigma > 0$), and μ is the continuous location parameter.	$$F(x) = \begin{cases} \dfrac{1}{1+(1+\alpha z)^{-1/\alpha}} \,\forall\, \alpha \neq 0 \\ \dfrac{1}{1+e^{-z}} \,\forall\, \alpha = 0 \end{cases}$$ where $z \equiv \dfrac{x-\mu}{\sigma}$.
Generalized Pareto $\left[\begin{array}{c} \mu \leq x < \infty \,\forall\, \alpha \geq 0 \\ \mu \leq x < \mu - \sigma/\alpha \,\forall\, \alpha < 0 \end{array}\right]$	$$f(x) = \begin{cases} \dfrac{1}{\sigma}\left(1+\alpha\dfrac{(x-\mu)}{\sigma}\right)^{-(1+1/\alpha)} \,\forall\, \alpha \neq 0 \\ \dfrac{1}{\sigma} e^{-\frac{(x-\mu)}{\sigma}} \,\forall\, \alpha = 0 \end{cases}$$ where α is the continuous shape parameter, σ is	$$F(x) = \begin{cases} 1-\left(1+\alpha\dfrac{(x-\mu)}{\sigma}\right)^{-1/\alpha} \,\forall\, \alpha \neq 0 \\ 1-e^{-\frac{(x-\mu)}{\sigma}} \,\forall\, \alpha = 0 \end{cases}$$

	the continuous scale parameter (σ > 0), and μ is the continuous location parameter.	
Gumbel Max $\left[-\infty < x < \infty\right]$	$f\left(x\right)=\frac{1}{\sigma}e^{-\left(z+e^{-z}\right)}$ where σ is the continuous scale parameter (σ > 0), and μ is the continuous location parameter.	$F\left(x\right)=e^{-e^{-z}}$ where $z\equiv\frac{x-\mu}{\sigma}$.
Gumbel Min $\left[-\infty < x < \infty\right]$	$f\left(x\right)=\frac{1}{\sigma}e^{\left(z-e^{z}\right)}$ where σ is the continuous scale parameter (σ > 0), and μ is the continuous location parameter.	$F\left(x\right)=1-e^{-e^{z}}$ where $z\equiv\frac{x-\mu}{\sigma}$.
Hyperbolic Secant $\left[-\infty < x < \infty\right]$	$f\left(x\right)=\frac{\operatorname{sech}\left(\frac{\pi\left(x-\mu\right)}{2\sigma}\right)}{2\sigma}$ where σ is the continuous scale parameter (σ > 0), and μ is the continuous location parameter.	$F\left(x\right)=\frac{2}{\pi}\arctan\left(e^{\pi\left(x-\mu\right)/2\sigma}\right)$

Inverse Gaussian (3–Parameter) $\left[\gamma < x < \infty\right]$	$f\left(x\right)=\sqrt{\frac{\lambda}{2\pi\left(x-\gamma\right)^{3}}}e^{-\lambda\left(x-\gamma-\mu\right)^{2}/2\mu^{2}\left(x-\gamma\right)}$ where λ and μ are continuous parameters $\left(\lambda>0;\mu>0\right)$, and γ is the continuous location parameter.	$F\left(x\right)=\Phi\left(\sqrt{\frac{\lambda}{x-\gamma}}\left(\frac{x-\gamma}{\mu}-1\right)\right)+$ $\Phi\left(-\sqrt{\frac{\lambda}{x-\lambda}}\left(\frac{x-\gamma}{\mu}+1\right)\right)e^{2\lambda/\mu}$ where Φ is the Laplace Integral.
Inverse Gaussian (2–Parameter) $\left[\gamma < x < \infty\right]$	$f\left(x\right)=\sqrt{\frac{\lambda}{2\pi x^{3}}}e^{-\lambda\left(x-\mu\right)^{2}/2\mu^{2}x}$	$F\left(x\right)=\Phi\left(\sqrt{\frac{\lambda}{x}}\left(\frac{x}{\mu}-1\right)\right)+$ $\Phi\left(-\sqrt{\frac{\lambda}{x}}\left(\frac{x}{\mu}+1\right)\right)e^{2\lambda/\mu}$
Johnson SB $\left[\beta \le x \le \beta+\lambda\right]$	$f\left(x\right)=\frac{\delta}{\lambda\sqrt{2\pi}z\left(1-z\right)}e^{-\frac{1}{2}\left(\gamma+\delta\ln\left(\frac{z}{1-z}\right)\right)^{2}}$ where γ and δ are the continuous shape parameter, λ is the continuous scale parameter ($\lambda>$ 0), and β is the continuous location parameter.	$F\left(x\right)=\Phi\left(\gamma+\delta\ln\left(\frac{z}{1-z}\right)\right)$ where $z\equiv\frac{x-\beta}{\lambda}$ and Φ is the Laplace Integral.

Johnson SU $\left[-\infty < x < \infty\right]$	$$f\left(x\right)=\frac{\delta}{\lambda\sqrt{2\pi}\sqrt{z^2+1}}e^{-\frac{1}{2}\left(\gamma+\delta\ln\left(z+\sqrt{z^2+1}\right)\right)^2}$$ where γ and δ are the continuous shape parameter, λ is the continuous scale parameter ($\lambda >$ 0), and β is the continuous location parameter.	$$F\left(x\right)=\Phi\left(\gamma+\delta\ln\left(z+\sqrt{z^2+1}\right)\right)$$ where $z\equiv\frac{x-\beta}{\lambda}$ and Φ is the Laplace Integral.
Kumaraswamy $\left[a\le x\le b\right]$	$$f\left(x\right)=\frac{\lambda_1\lambda_2 z^{\lambda_1-1}\left(1-z^{\lambda_1}\right)^{\lambda_2-1}}{b-a}$$ where λ_1 and λ_2 are continuous shape parameters $\left(\lambda_1>0;\lambda_2>0\right)$, and a and b are the continuous boundary parameters $\left(a<b\right)$	$$F\left(x\right)=1-\left(1-z^{\lambda_1}\right)^{\lambda_2}$$ where $z\equiv\frac{x-a}{b-a}$.
Laplace $\left[-\infty < x < \infty\right]$	$$f\left(x\right)=\frac{\lambda}{2}e^{-\lambda\lvert x-\mu\rvert}$$ where λ is the continuous inverse scale	$$F\left(x\right)=\begin{cases}\frac{1}{2}e^{-\lambda\left(\mu-x\right)} & \forall x\le\mu\\ 1-\frac{1}{2}e^{-\lambda\left(x-\mu\right)} & \forall x>\mu\end{cases}$$

	parameter ($\lambda >$ 0), and μ is the continuous location parameter.	
Levy (2–Parameter) $\left[\gamma < x < \infty\right]$	$$f\left(x\right)=\sqrt{\frac{\lambda}{2\pi}}\frac{e^{-0.5\lambda/x-\gamma}}{\left(x-\gamma\right)^{3/2}}$$ where λ is the continuous scale parameter ($\lambda >$ 0), and γ is the continuous location parameter.	$$F\left(x\right)=2-2\Phi\left(\sqrt{\frac{\lambda}{x-\gamma}}\right)$$ where Φ is the Laplace Integral.
Levy (1–Parameter) $\left[\gamma < x < \infty\right]$	$$f\left(x\right)=\sqrt{\frac{\lambda}{2\pi}}\frac{e^{-0.5\lambda/x}}{\left(x-\gamma\right)^{3/2}}$$	$$F\left(x\right)=2-2\Phi\left(\sqrt{\frac{\lambda}{x}}\right)$$
Log–Gamma $\left[0 < x < \infty\right]$	$$f\left(x\right)=\frac{\left(\ln\left(x\right)\right)^{\alpha-1}}{x\beta^{\alpha}\Gamma\left(\alpha\right)}e^{-\ln\left(x\right)/\beta}$$ where α and β are the continuous parameters $\left(\alpha > 0; \beta > 0\right)$.	$$F\left(x\right)=\frac{\Gamma_{\ln\left(x\right)/\beta}\left(\alpha\right)}{\Gamma\left(\alpha\right)}$$
Logistic $\left[-\infty < x < \infty\right]$	$$f\left(x\right)=\frac{e^{-z}}{\lambda\left(1+e^{-z}\right)^{2}}$$	$$F\left(x\right)=\frac{1}{1+e^{-z}}$$

	where λ is the continuous scale parameter ($\lambda >$ 0), and γ is the continuous location parameter.	where $z \equiv \frac{x-\gamma}{\sigma}$
Log–Logistic (3–Parameter) $\left[\gamma \le x < \infty\right]$	$$f(x)=\frac{\frac{\alpha}{\beta}\left(\frac{x-\gamma}{\beta}\right)^{\alpha-1}}{\left(1+\left(\frac{x-\gamma}{\beta}\right)^{\alpha}\right)^{2}}$$ where α is the continuous shape parameter $(\alpha > 0)$, β is the continuous scale parameter (β > 0), and γ is the continuous location parameter $(\gamma \equiv 0)$.	$$F(x)=\frac{1}{1+\left(\beta/_{x-\gamma}\right)^{\alpha}}$$
Log–Logistic (2–Parameter) $\left[\gamma \le x < \infty\right]$	$$f(x)=\frac{\frac{\alpha}{\beta}\left(\frac{x}{\beta}\right)^{\alpha-1}}{\left(1+\left(\frac{x}{\beta}\right)^{\alpha}\right)^{2}}$$	$$F(x)=\frac{1}{1+\left(\beta/_{x}\right)^{\alpha}}$$

Lognormal (3–Parameter) $[\gamma < x < \infty]$	$$f(x) = \frac{e^{-\frac{1}{2}\left(\frac{\ln(x-\gamma)-\lambda_2}{\lambda_1}\right)^2}}{(x-\gamma)\lambda_1\sqrt{2\pi}}$$ where λ_1 and λ_2 are the continuous parameters $(\lambda_1 > 0)$, and γ is the continuous location parameter ($\gamma \equiv 0$).	$$F(x) = \Phi\left(\frac{\ln(x-\gamma)-\lambda_2}{\lambda_1}\right)$$ where Φ is the Laplace Integral.
Lognormal (2–Parameter) $[\gamma < x < \infty]$	$$f(x) = \frac{e^{-\frac{1}{2}\left(\frac{\ln x-\lambda_2}{\lambda_1}\right)^2}}{x\lambda_1\sqrt{2\pi}}$$	$$F(x) = \Phi\left(\frac{\ln x-\lambda_2}{\lambda_1}\right)$$
Log–Pearson 3 $\begin{bmatrix} 0 < x \le e^{\gamma}\ \forall\ \beta < 0 \\ e^{\gamma} \le x < \infty\ \forall\ \beta < 0 \end{bmatrix}$	$$f(x) = \frac{1}{x\lvert\beta\rvert\Gamma(\alpha)}\left(\frac{\ln(x)-\gamma}{\beta}\right)^{\alpha-1} e^{-\ln(x)-\gamma/\beta}$$ where α, β and γ are the continuous parameters $(\alpha > 0; \beta \ne 0)$.	$$F(x) = \frac{\Gamma_{(\ln(x)-\gamma)/\beta}(\alpha)}{\Gamma(\alpha)}$$
Nakagami $[0 \le x < \infty]$	$$f(x) = \frac{2\alpha^{\alpha}}{\Gamma(\alpha)\beta^{\alpha}} x^{2\alpha-1} e^{-\alpha x^2/\beta}$$	$$F(x) = \frac{\Gamma_{\alpha x^2/\beta}(\alpha)}{\Gamma(\alpha)}$$

	where α and β are the continuous parameters $(\alpha \geq 0.5; \beta > 0)$.	
Normal $[-\infty < x < \infty]$	$f(x) = \dfrac{e^{-\frac{1}{2}\left(\frac{x-\mu}{\sigma}\right)^2}}{\sigma\sqrt{2\pi}}$ where σ is the continuous scale parameter $(\sigma > 0)$, and μ is the continuous location parameter.	$F(x) = \Phi\left(\dfrac{x-\mu}{\sigma}\right)$ where Φ is the Laplace Integral.
Pareto (First Kind) $[\lambda \leq x < \infty]$	$f(x) = \dfrac{\lambda\beta^{\lambda}}{x^{\lambda+1}}$ where λ is the continuous shape parameter $(\lambda > 0)$, β is the continuous scale parameter (β > 0).	$F(x) = 1 - \left(\dfrac{\beta}{x}\right)^{\lambda}$
Pareto (Second Kind) $[0 \leq x < \infty]$	$f(x) = \dfrac{\lambda\beta^{\lambda}}{(x+\beta)^{\lambda+1}}$	$F(x) = 1 - \left(\dfrac{\beta}{x+\beta}\right)^{\lambda}$

	where λ is the continuous shape parameter $(\lambda > 0)$, β is the continuous scale parameter (β > 0).	
Pearson Type 5 (3–Parameter) $[\gamma < x < \infty]$	$f(x) = \frac{e^{-\beta/(x-\gamma)}}{\beta\Gamma(\alpha)\left((x-\gamma)/\beta\right)^{\alpha+1}}$ where α is the continuous shape parameter $(\alpha > 0)$, β is the continuous scale parameter (β > 0), and γ is the continuous location parameter $(\gamma \equiv 0)$.	$F(x) = 1 - \frac{\Gamma_{\beta/(x-\gamma)}(\alpha)}{\Gamma(\alpha)}$
Pearson Type 5 (2–Parameter) $[\gamma < x < \infty]$	$f(x) = \frac{e^{-\beta/x}}{\beta\Gamma(\alpha)\left(x/\beta\right)^{\alpha+1}}$	$F(x) = 1 - \frac{\Gamma_{\beta/x}(\alpha)}{\Gamma(\alpha)}$

Pearson Type 6 (4–Parameter) $\left[\gamma \le x < \infty\right]$	$f\left(x\right)=\dfrac{\left(\left(x-\gamma\right)/\beta\right)^{\lambda_1-1}}{\beta\,\mathrm{B}\left(\lambda_1,\lambda_2\right)\left(1+\left(x-\gamma\right)/\beta\right)^{\lambda_1+\lambda_2}}$ where λ_1 and λ_2 are the continuous shape parameters $\left(\lambda_1>0;\lambda_2>0\right)$, β is the continuous scale parameter ($\beta>0$), γ is the continuous location parameter $\left(\gamma\equiv 0\right)$, and B is the Beta Function.	$F\left(x\right)=\mathrm{I}_{\left(x-\gamma\right)/\left(x-\gamma+\beta\right)}\left(\lambda_1,\lambda_2\right)$ where I_z is the Regularized Incomplete Beta Function.
Pearson Type 6 (3–Parameter) $\left[\gamma \le x < \infty\right]$	$f\left(x\right)=\dfrac{\left(x/\beta\right)^{\lambda_1-1}}{\beta\,\mathrm{B}\left(\lambda_1,\lambda_2\right)\left(1+x/\beta\right)^{\lambda_1+\lambda_2}}$	$F\left(x\right)=\mathrm{I}_{x/\left(x+\beta\right)}\left(\lambda_1,\lambda_2\right)$
Pert $\left[a \le x \le b\right]$	$f\left(x\right)=\dfrac{1}{\mathrm{B}\left(\alpha,\beta\right)}\dfrac{\left(x-a\right)^{\alpha-1}\left(b-x\right)^{\beta-1}}{\left(b-a\right)^{\alpha+\beta-1}}$	$F\left(x\right)=\mathrm{I}_z\left(\alpha,\beta\right)$ where $z\equiv\dfrac{x-a}{b-a}$ and I_z is the Regularized

	where $\alpha = \frac{4m+b-5a}{b-a}$, $\beta = \frac{5b-a-4m}{b-a}$, m is the continuous mode parameter $(a \le m \le b)$, a and b are the continuous boundary parameters, and B is the Beta Function.	Incomplete Beta Function.
Phased Bi–Exponential $[\gamma_1 \le x < \infty]$	$f(x) = \begin{cases} \beta_1 e^{-\beta_1(x-\gamma_1)} \ \forall \gamma_1 \le x \le \gamma_2 \\ \beta_2 e^{-(\beta_2(c-\gamma_2)+\beta_1(\gamma_2-\gamma_1))} \ \forall \gamma_2 \le x < \infty \end{cases}$ where β_1 and β_2 are the continuous inverse scale parameters $(\beta_1 > 0; \beta_2 > 0)$, and γ_1 and γ_2 are the continuous location parameters $(\gamma_2 > \gamma_1)$.	$F(x) = \begin{cases} 1-e^{-\beta_1(x-\gamma_1)} \ \forall \gamma_1 \le x \le \gamma_2 \\ 1-e^{-(\beta_2(c-\gamma_2)+\beta_1(\gamma_2-\gamma_1))} \ \forall \gamma_2 \le x < \infty \end{cases}$
Phased Bi–Weibull $[\gamma_1 \le x < \infty]$ $\left\{ \left(\frac{\gamma_2-\gamma_1}{\beta_1}\right)^{\alpha_1} = \left(\frac{\gamma_2-\gamma_1}{\beta_2}\right)^{\alpha_2} \right\}$	$f(x) = \begin{cases} \frac{\alpha_1}{\beta_1}\left(\frac{x-\gamma_1}{\beta_1}\right)^{\alpha_1-1} e^{-\left(\frac{x-\gamma_1}{\beta_1}\right)^{\alpha_1}} \ \forall \gamma_1 \le x \le \gamma_2 \\ \frac{\alpha_2}{\beta_2}\left(\frac{x-\gamma_1}{\beta_2}\right)^{\alpha_2-1} e^{-\left(\frac{x-\gamma_1}{\beta_2}\right)^{\alpha_2}} \ \forall \gamma_2 \le x < \infty \end{cases}$ where α_1 and α_2 are the continuous shape	$F(x) = \begin{cases} 1-e^{-\left(\frac{x-\gamma_1}{\beta_1}\right)^{\alpha_1}} \ \forall \gamma_1 \le x \le \gamma_2 \\ 1-e^{-\left(\frac{x-\gamma_1}{\beta_2}\right)^{\alpha_2}} \ \forall \gamma_2 \le x < \infty \end{cases}$

	parameters $(\alpha_1 > 0; \alpha_2 > 0)$, β_1 and β_2 are the continuous scale parameters $(\beta_1 > 0; \beta_2 > 0)$, and γ_1 and γ_2 are the continuous location parameters $(\gamma_2 > \gamma_1)$.	
Power Function $[a \le x \le b]$	$f(x) = \frac{\lambda (x-a)^{\lambda-1}}{(b-a)^{\lambda}}$ where λ is the continuous shape parameter $(\lambda > 0)$, and a and b are the continuous boundary parameters ($a < b$).	$F(x) = \left(\frac{x-a}{b-a}\right)^{\lambda}$
Rayleigh (2–Parameter) $[\gamma \le x < \infty]$	$f(x) = \frac{x-\gamma}{\beta^2} e^{-\frac{1}{2}\left(x-\gamma/\beta\right)^2}$ where β is the continuous scale parameter ($\beta >$ 0), and γ is the continuous location parameter.	$F(x) = 1 - e^{-\frac{1}{2}\left(x-\gamma/\beta\right)^2}$

Rayleigh (1–Parameter) $\left[\gamma \le x < \infty\right]$	$f(x) = \dfrac{x}{\beta^2} e^{-\frac{1}{2}\left(x/\beta\right)^2}$	$F(x) = 1 - e^{-\frac{1}{2}\left(x/\beta\right)^2}$
Reciprocal $\left[a \le x \le b\right]$	$f(x) = \dfrac{1}{x\left(\ln(b) - \ln(a)\right)}$ where a and b are the continuous boundary parameters (0 < a < b).	$F(x) = \dfrac{\ln(x) - \ln(a)}{\ln(b) - \ln(a)}$
Rice $\left[0 \le x < \infty\right]$	$f(x) = \dfrac{x}{\sigma^2} e^{-\left(\left(x^2+\nu^2\right)/2\sigma^2\right)} \mathrm{I}_0\left(\dfrac{x\nu}{\sigma^2}\right)$ where ν and σ are the continuous parameters $\left(\nu \ge 0; \sigma > 0\right)$, I_0 is the modified function of the first kind of order zero.	$F(x) = 1 - Q_1\left(\dfrac{\nu}{\sigma}, \dfrac{x}{\sigma}\right)$ where Q_1 is the Marcum Q–function.
Student's T $\left[-\infty < x < \infty\right]$	$f(x) = \dfrac{1}{\sqrt{\pi\nu}} \dfrac{\Gamma\left(\left(\nu+1\right)/2\right)}{\Gamma\left(\nu/2\right)} \left(\dfrac{\nu}{\nu + x^2}\right)^{(\nu+1)/2}$ where ν is the degrees of freedom (positive	$F(x) = \begin{cases} \dfrac{1}{2} - \dfrac{1}{2}\mathrm{I}_z\left(\dfrac{1}{2}, \dfrac{\nu}{2}\right) \forall\, x < 0 \\ \dfrac{1}{2} + \dfrac{1}{2}\mathrm{I}_z\left(\dfrac{1}{2}, \dfrac{\nu}{2}\right) \forall\, x \ge 0 \end{cases}$

	integer).	where $z \equiv \frac{x^2}{\nu + x^2}$ and I_z is the Regularized Incomplete Beta Function.
Triangular $[a \le x \le b]$	$f(x) = \begin{cases} \frac{2(x-a)}{(m-a)(b-a)} \forall a \le x \le m \\ \frac{2(b-x)}{(b-m)(b-a)} \forall m < x \le b \end{cases}$ where m is the continuous mode parameter $(a \le m \le b)$, a and b are the continuous boundary parameters ($a < b$).	$F(x) = \begin{cases} \frac{(x-a)^2}{(m-a)(b-a)} \forall a \le x \le m \\ 1 - \frac{(b-x)^2}{(b-m)(b-a)} \forall m < x \le b \end{cases}$
Uniform $[a \le x \le b]$	$f(x) = \frac{1}{b-a}$ where a and b are the continuous boundary parameters ($a < b$).	$F(x) = \frac{x-a}{b-a}$
Wakeby	$f(x) = \frac{(1-F(x))^{\delta+1}}{\alpha t + \gamma}$	The distribution is defined by the Quantile function (Inverse CDF),

$\begin{bmatrix} \xi \le x < \infty \,\forall\, \delta \ge 0 \\ \gamma > 0 \\ \xi \le x \le \xi + \alpha/\beta - \gamma/\delta \,\forall\, \delta < 0 \\ or\, \gamma = 0 \end{bmatrix}$ $\begin{Bmatrix} \alpha \ne 0\, or\, \gamma \ne 0 \\ \beta + \delta > 0\, or\, \beta = \gamma = \delta = 0 \\ if\ \alpha = 0, then\, \beta = 0 \\ if\ \gamma = 0, then\, \delta = 0 \\ \gamma \ge 0\, \&\, \alpha + \gamma \ge 0 \end{Bmatrix}$	where $t = \left(1 - F(x)\right)^{\beta+\gamma}$ and F is the CDF.	$x(F) = \xi + \frac{\alpha}{\beta}\left(1 - (1-F)^{\beta}\right) - \frac{\gamma}{\delta}\left(1 - \frac{1}{(1-F)^{\delta}}\right)$
Weibull (3–Parameter) $\left[\gamma \le x < \infty\right]$	$f(x) = \frac{\lambda}{\beta}\left(\frac{x-\gamma}{\beta}\right)^{\lambda-1} e^{-\left(x-\gamma/\beta\right)^{\lambda}}$ where λ is the shape parameter ($\lambda > 0$), β is the continuous scale parameter ($\beta > 0$), and γ is the continuous location parameter $(\gamma \equiv 0)$.	$F(x) = 1 - e^{-\left(x-\gamma/\beta\right)^{\lambda}}$
Weibull (2–Parameter) $\left[\gamma \le x < \infty\right]$	$f(x) = \frac{\lambda}{\beta}\left(\frac{x}{\beta}\right)^{\lambda-1} e^{-\left(x/\beta\right)^{\lambda}}$	$F(x) = 1 - e^{-\left(x/\beta\right)^{\lambda}}$

APPENDIX B

VARIATION OF HYDROMETEOROLOGICAL VARIABLES

Table B–1 to B–3, B–4 to B–6, and B–7 to B–9 lists the average precipitation per season in the decade in moderately wet, considerably wet, and extremely wet periods, for Cold Desert/Semi–Arid Climate, Humid Sub–Tropical Climate, and Warm Desert/Semi–Arid Climate regions of Texas, respectively. Here '–' denotes nil precipitation events of the order of respective SPI thresholds.

Tables B–10 to B–12, B–13 to B–15, and B–16 to B–18 list the decadal variation of average seasonal temperature (T_{avg}–S), mean of maximum daily temperature in a season (EMXT–S), and total number of days with projected maximum temperature of 90°F (DX90–S) for Cold Desert/Semi–Arid Climate, Humid Sub–Tropical Climate, and Warm Desert/Semi–Arid Climate regions of Texas, respectively.

Here, the conventional seasonal classification approach is adopted: (i) *December–February (DJF)*: Winter Season, (ii) *March–May (MAM)*: Spring Season, (iii) *June–August (JJA)*: Summer Season, and (iv) *September–November (SON)*: Autumn Season.

Table B–1: Average precipitation (*in.*) in moderately wet period $\{0.00 \leq SPI \leq 0.99\}$ for Cold Desert/Semi–Arid Climate Region

Seasons / Decades	DJF	MAM	JJA	SON
1971–1980	1.7	2.5	6.3	7.2
1981–1990	2.3	2.8	8.0	7.2
1991–2000	3.0	2.7	7.7	6.8
2001–2010	3.2	3.6	7.0	6.8

Table B–2: Average precipitation (*in.*) in considerably wet period $\{1.00 \leq SPI \leq 1.99\}$ for Cold Desert/Semi–Arid Climate Region

Seasons / Decades	DJF	MAM	JJA	SON
1971–1980	2.3	4.3	10.4	11.8
1981–1990	3.8	2.5	9.7	10.5
1991–2000	3.9	4.4	10.3	9.9
2001–2010	3.1	6.1	8.0	11.4

Table B–3: Average precipitation (*in.*) in extremely wet period $\{SPI \geq 2.00\}$ for Cold Desert/Semi–Arid Climate Region

Seasons / Decades	DJF	MAM	JJA	SON
1971–1980	–	1.0	–	14.3

1981–1990	5.0	9.0	7.0	18.0
1991–2000	5.1	4.2	16.5	–
2001–2010	3.7	4.8	10.0	9.3

Table B–4: Average precipitation (*in.*) in moderately wet period $\{0.00 \le SPI \le 0.99\}$ for Humid Sub–Tropical Climate Region

Seasons / Decades	**DJF**	**MAM**	**JJA**	**SON**
1971–1980	8.1	8.1	11.2	11.5
1981–1990	7.3	6.9	12.7	10.1
1991–2000	8.1	8.7	11.4	11.3
2001–2010	9.3	8.4	10.1	11.4

Table B–5: Average precipitation (*in.*) in considerably wet period $\{1.00 \le SPI \le 1.99\}$ for Humid Sub–Tropical Climate Region

Seasons / Decades	**DJF**	**MAM**	**JJA**	**SON**
1971–1980	10.8	11.0	14.3	17.5
1981–1990	10.4	9.6	19.3	14.9
1991–2000	12.5	10.6	11.1	16.3
2001–2010	8.9	12.0	15.7	16.3

Table B–6: Average precipitation (*in.*) in extremely wet period $\{SPI \geq 2.00\}$ for Humid Sub–Tropical Climate Region

Seasons / Decades	DJF	MAM	JJA	SON
1971–1980	–	–	12.0	26.0
1981–1990	19.5	9.0	26.0	–
1991–2000	14.9	4.0	19.0	–
2001–2010	28.0	9.0	21.0	19.5

Table B–7: Average precipitation (*in.*) in moderately wet period $\{0.00 \leq SPI \leq 0.99\}$ for Warm Desert/Semi–Arid Climate Region

Seasons / Decades	DJF	MAM	JJA	SON
1971–1980	3.5	2.1	7.3	7.2
1981–1990	3.6	2.6	8.0	6.1
1991–2000	3.5	3.1	5.9	6.7
2001–2010	5.5	2.2	6.1	5.2

Table B–8: Average precipitation (*in.*) in considerably wet period $\{1.00 \leq SPI \leq 1.99\}$ for Warm Desert/Semi–Arid Climate Region

Seasons / Decades	DJF	MAM	JJA	SON
1971–1980	2.0	0.7	9.0	12.9

1981–1990	3.5	3.3	7.4	8.8
1991–2000	2.4	2.3	6.8	11.0
2001–2010	3.0	6.3	8.1	8.0

Table B–9: Average precipitation (*in.*) in extremely wet period $\{SPI \geq 2.00\}$ for Warm Desert/Semi–Arid Climate Region

Seasons / Decades	**DJF**	**MAM**	**JJA**	**SON**
1971–1980	–	1.0	12.0	10.0
1981–1990	8.0	–	7.0	–
1991–2000	8.3	2.5	–	–
2001–2010	4.0	5.0	10.5	11.0

Table B–10: Average seasonal temperature (°F) for Cold Desert/Semi–Arid Climate Region

Seasons / Decades	**DJF**	**MAM**	**JJA**	**SON**
1971–1980	42.8	61.7	79.1	61.4
1981–1990	42.4	61.7	79.1	62.4
1991–2000	44.7	62.2	79.8	62.2
2001–2010	44.2	62.9	78.2	62.6

Table B–11: Mean of maximum daily temperature in a season (°F) for Cold Desert/Semi–Arid Climate Region

Seasons / Decades	DJF	MAM	JJA	SON
1971–1980	85.3	100.7	107.9	99.7
1981–1990	84.3	101.1	107.8	100.4
1991–2000	83.8	102.3	108.7	99.9
2001–2010	86.8	104.0	107.0	98.3

Table B–12: Total number of days with projected maximum temperature of 90°F for Cold Desert/Semi–Arid Climate Region

Seasons / Decades	DJF	MAM	JJA	SON
1971–1980	1	901	4952	981
1981–1990	1	993	5050	991
1991–2000	4	1124	5269	1158
2001–2010	7	1178	5279	881

Table B–13: Average seasonal temperature (°F) for Humid Sub–Tropical Climate Region

Seasons / Decades	DJF	MAM	JJA	SON
1971–1980	49.4	67.1	82.4	67.7
1981–1990	49.6	67.2	82.9	68.9
1991–2000	52.0	67.4	83.5	68.4
2001–2010	50.8	68.0	83.6	70.7

Table B–14: Mean of maximum daily temperature in a season (°F) for Humid Sub–Tropical Climate Region

Seasons / Decades	DJF	MAM	JJA	SON
1971–1980	90.0	101.6	106.8	101.2
1981–1990	88.6	102.4	108.1	102.9
1991–2000	89.1	102.8	109.5	103.0
2001–2010	89.7	104.7	108.0	100.9

Table B–15: Total number of days with projected maximum temperature of 90°F for Humid Sub–Tropical Climate Region

Seasons / Decades	DJF	MAM	JJA	SON
1971–1980	20	1211	10026	2488
1981–1990	27	1448	10325	2879
1991–2000	37	1515	10599	3012
2001–2010	24	1787	10570	2670

Table B–16: Average seasonal temperature (°F) for Warm Desert/Semi–Arid Climate Region

Seasons / Decades	DJF	MAM	JJA	SON
1971–1980	49.0	66.8	80.9	65.5
1981–1990	48.8	67.0	81.3	66.8
1991–2000	51.3	68.1	82.9	67.0
2001–2010	50.6	68.8	83.0	67.9

Table B–17: Mean of maximum daily temperature in a season (°F) for Warm Desert/Semi–Arid Climate Region

Seasons / Decades	DJF	MAM	JJA	SON
1971–1980	86.3	100.5	107.0	99.1
1981–1990	85.2	101.9	107.5	101.2
1991–2000	86.6	102.2	108.1	101.0
2001–2010	86.4	104.6	107.4	99.5

Table B–18: Total number of days with projected maximum temperature of 90°F for Warm Desert/Semi–Arid Climate Region

Seasons / Decades	DJF	MAM	JJA	SON
1971–1980	2	565	2148	547
1981–1990	5	619	2207	552
1991–2000	5	744	2316	654
2001–2010	5	690	2276	515

APPENDIX C

GANTT CHART OF RESEARCH

Stages of Research	**2015**			**2016**												**2017**			
	O	**N**	**D**	**J**	**F**	**M**	**A**	**M**	**J**	**J**	**A**	**S**	**O**	**N**	**D**	**J**	**F**	**M**	**A**
Idea Development																			
Literature Review																			
Analysis: Research Objective I																			
Analysis: Research Objective II																			
Analysis: Research Objective III																			
Thesis Development																			

APPENDIX D

RESEARCH PUBLICATIONS

D.1 Thesis Publications

D.1.1 Peer–Reviewed Journals

Bhatia, Nikhil, and Vijay P. Singh. "Long–term variations in Texas Meteorology: An assessment of Standardized Precipitation Index and Extreme Precipitation Events", *Theoretical and Applied Climatology*, (2017) {Under–Review}

Bhatia, Nikhil, Vijay P. Singh, and Roshan K. Srivastav. "Variability of Extreme Precipitation over Texas and its relationship with Climatic Cycles", *Theoretical and Applied Climatology*, (2017) {Under–Review}

Bhatia, Nikhil, and Vijay P. Singh. "Sensitivity of Extreme Precipitation in Texas to Climatic Cycles", *Journal of Applied Meteorology and Climatology*, (2017) {Under–Review}

D.1.2 Professional Conferences

Bhatia, Nikhil, Vijay P. Singh, and Roshan K. Srivastav. “Influence of Climate Oscillations on Extreme Precipitation in Texas”, *AGU Fall Meeting*, San Francisco, California (December 12–16, 2016)

D.2 Additional Publications

D.2.1 Professional Conferences

Bhatia, Nikhil, and Vijay P. Singh. “Evaluation of hydrologic models for Texas Flash Flood Alley”, *ASABE Annual International Meeting*, Spokane, Washington (July 16–17, 2017)

Bhatia, Nikhil, Vijay P. Singh, and Roshan K. Srivastav, “Quantifying the impact of Teleconnections on Hydrologic Regimes in Texas”, *AGU Fall Meeting*, San Francisco, California (December 12–16, 2016)

D.2.2 Scopus–Registered Conference Proceedings

Bhatia, Nikhil, and Vijay P. Singh. "Evaluation of hydrologic models for Texas Flash Flood Alley", *ASABE Proceedings*, (2017)

D.2.3 University–Level Symposia

Bhatia, Nikhil, and Vijay P. Singh. “Variation of the impact of Pacific Decadal Oscillation on extreme streamflow regimes in Texas”, *Water Daze Conference*, Texas A&M University, College Station, Texas (April 05, 2017)

Bhatia, Nikhil, and Vijay P. Singh, “Variation of the impact of Pacific Decadal Oscillation on extreme streamflow regimes in Texas”, *Student Research Week*, Graduate and Professional Student Council, Texas A&M University, College Station, Texas (March 27–31, 2017)

Bhatia, Nikhil, Vijay P. Singh, and Roshan K. Srivastav, “Climate variability and its impacts on recent major flood events in the United States”, *Symposium for*

Agricultural and Applied Economics Research, Texas A&M University, College Station, Texas (April 15, 2016)

Bhatia, Nikhil, Vijay P. Singh, and Roshan K. Srivastav, "Quantifying the impact of Climatic Cycles on Hydrologic Extremes in Texas", *Water Daze Conference*, Texas A&M University, College Station, Texas (March 30, 2016)

Bhatia, Nikhil, and Vijay P. Singh, "Quantifying the impact of Climatic Cycles on Hydrologic Extremes in Texas", *Student Research Week*, Graduate and Professional Student Council, Texas A&M University, College Station, Texas (March 29–31, 2016)